PRECISION RADIAL VELOCITY SPECTROMETER

Document Title	**Science Case**
Document Number	PRVS-SPEC-00004-0001
Issue	3.0
Date	21st September 2006

Document Prepared By:	Hugh Jones	**Signature and Date**	Hugh Jones 21st September 2006
Document Approved By:	John Rayner	**Signature and Date**	John Rayner 21st September 2006
Document Released By:	Dave Lunney	**Signature and Date**	Dave Lunney 21st September 2006

CHANGE RECORD

Issue	Date	Section affected	Change Description
0.1	30 August 2006	5	Pathfinder detailed pasted in OCDD numbers pasted in
0.2	12th September 2006	All	Finalise surveys Finalise skewness calculations More Gemini N/S Other cases – Fox, Vacca, Barnes References
1.0	18th September 2006		Reviewed by PR & DWL
1.1	20 September 2006	All	Editing, format - WRFD
2.0	20 September 2006	All	Check through
3.0	21 Sept 2006	All	Corrected version

PRECISION RADIAL VELOCITY SPECTROMETER

Document Number:	PRVS-SPEC-00004-0001
Issue:	3.0
Category:	Systems
Status:	Issued
Author:	Hugh Jones et al
Date:	21st September

Table of Contents

1. PURPOSE

This document describes the science case for the Gemini Precision Radial Velocity Spectrometer (PRVS). It presents a description of the main scientific reasons to build PRVS and provides details of the programmes, strategies and calibration system. It has been shaped by the contributions from two science team workshops in Washington (January 2006), and Edinburgh (March 2006). The participants in these workshops as well as other interested parties who have helped shape the science case are given below. The "Science Team" is not fixed: our expectation is that experts will join as either Full or Associate members, depending on their contribution, and that Gemini will play a significant role in these definitions.

Scientist	Institute, Location	Specialities
Jeremy Bailey	McQuaire University, Australia	Planets, Exoplanets, IR astronomy
John Barnes	University of Hertfordshire, UK	Cool stars
Tim Brown	Las Cumbres Observatory	Precision astronomy
Andrew Collier Cameron	University of St Andrews, UK	Doppler/Zeeman mapping
Mike Cushing	Arizona, USA	Brown dwarfs
Bill Dent	ATC, Edinburgh, UK	Young disks, star & planet formation
Jean-Francios Donati	Toulouse, France	Polarimetry
Derek Fox	Penn State, USA	Gamma Ray Bursts
Todd Henry	Georgia State, USA	Nearby stars
Chris Johns-Krull	Rice University, USA	Stellar activity
Hugh Jones	University of Hertfordshire, UK	Exoplanets, brown dwarfs
Jim Kasting	Penn State, USA	Brown dwarfs
Marek Konacki	Nicolaus Copernicus, Poland	Exoplanets
Andrew Levan	University of Hertfordshire, UK	High Redshift Cosmology
Doug Lin	University of California, USA	Star and planet formation
Mike Liu	IfA, Hawaii, USA	Brown dwarfs, extra-solar planets
Andy Longmore	ATC, Edinburgh, UK	Infrared astronomy
Kevin Luhman	Penn State, USA	Brown dwarfs
Steve Miller	University College London, UK	Solar system
Mike Murphy	University of Cambridge, UK	Fine structure constant
Andrej Niedzielski	Torun Observatory, Poland	Precision astronomy
Francesco Pepe	Genva Observatory, Switzerland	Precision radial velocities
Lisa Prato	Lowell Observatory, USA	IR binaries
Larry Ramsey	Penn State, USA	Star formation, binaries, YSOs
John Rayner	IfA, Hawaii, USA	Star formation
Ignas Snellen	Leiden University, Netherlands	Characterisation of extra-solar planets
Ed Thommes	CTIA, Canada	Star and planet formation
Chris Tinney	AAO, Australia	Exoplanets, brown dwarfs
Bill Vacca	Sophia Observatory, USA	Exoplanets
Adrian Webster	IfA, Edinburgh, UK	Interstellar chemistry
Alex Wolszczan	Penn State, USA	Exoplanets

2. APPLICABLE AND REFERENCE DOCUMENTS

Reference	Document Title	Document Number	Issue / Date
AD01	Science Requirements Document	PRVS-SPEC-00005-0001	1.0 / 18th Sep 2006
AD01	Instrument Design And Analysis	PRVS-PLA-00006-0001	1.0 / 14th Sep 2006
AD01	Calibration Assembly	PRVS-TRE-00004-0001	1.0 / 16th Sep 2006

3. ACRONYMS AND ABBREVIATIONS

PRVS	Precision Radial Velocity Spectrometer
PRV	Precision Radial Velocity
RMS	Root Mean Squared
S/N	Signal-to-Noise
NIR	Near InfraRed
Q	Quality factor
FRD	Functional Requirements Document
FOV	Field Of View
QI	Quartz Iodine
LN	Liquid Nitrogen
XD	Cross Disperser
SDSU	San Diego State University
PC	Personal Computer
DC	Direct Current
CCF	Cross Correlation Function
km/s	kilometres per second
m/s	metres per second
BD	Brown dwarf
Exoplanet	Extra-Solar Planet
SRF	Spectral Response Function

4. DEFINITIONS

TBD To Be Defined : a requirement to be developed during the preliminary design stage of the instrument.

TBC To Be Confirmed : a requirement that is correct with the current design information but requires confirmation during the preliminary design stage of the instrument.

TBR To Be Reviewed : a requirement specified to meet the PRVS top-level requirements, but which might over-constrain the design.

5. FINDING TERRESTRIAL-MASS PLANETS AROUND LOW-MASS STARS

The discovery of the Jupiter-mass planet 51 Peg B (Mayor & Queloz 1995) and the rapid detection of giant planets around several other stars (e.g. Marcy & Butler 1996) rapidly turned the search for extra-solar planets from a quirky backwater into a flourishing mainstream activity. In the last 5 years the field has matured into a complex and vibrant discipline that now lies at the heart of astronomical research. While we are still not yet sensitive to the presence of our Solar System around any Solar type star, the number of exoplanets discovered now stands at over 200 including at least 20 multiple planet systems. They have now been discovered in most environments where a concerted effort has been made. In particular, they have been discovered with a wide range of orbital parameters around most spectral types and even around pulsars. It thus seems they form easily and are rather robust to stellar evolution. There are many potential avenues for exoplanet research that are being explored in order to ultimately better understand our Solar System, the Earth and our human race in the context of planetary systems more generally.

The "Doppler Wobble" technique has played the dominant role in foundation of this new field. Surveys using this method have discovered almost all the planets known within 200 pc, and the vast majority of gas-giant planets found within 3 AU of their host stars. Other techniques, such as searches for planetary transits and gravitational micro-lensing events have so far had limited success, although many of these programs have begun only recently. Doppler searches, however, provide the most accurate estimates of key exoplanet properties: minimum planet mass; orbital period; orbital semi-major axis; and eccentricity. They also differ from photometric transit and micro-lensing surveys because they specifically target nearby well characterised stars. They provide robust minimum masses and orbital parameters and allow for critical and independent verification by other groups and techniques. One of the key results coming out of the Doppler surveys so far is that low-mass planets are much more common than high-mass ones with $dN/dM \propto M^{-1.18}$, and exoplanets form with masses at least as low as Neptune. Improvements in the efficiency and sampling of searches at optical wavelengths promise long-term precisions of ~0.5 m/s and ~5 $M_\oplus$ detections around solar-type stars. While this is likely to be the lower mass limit for CCD-based of solar type surveys until larger telescopes become available, it is feasible to survey lower mass primaries to achieve a corresponding smaller mass limit. Thus the lowest mass planets have been found around M dwarfs (e.g., GJ876d: 7 $M_\oplus$ Rivera et al. 2005), with detections down to a few $M_\oplus$ feasible around mid-M spectral types.

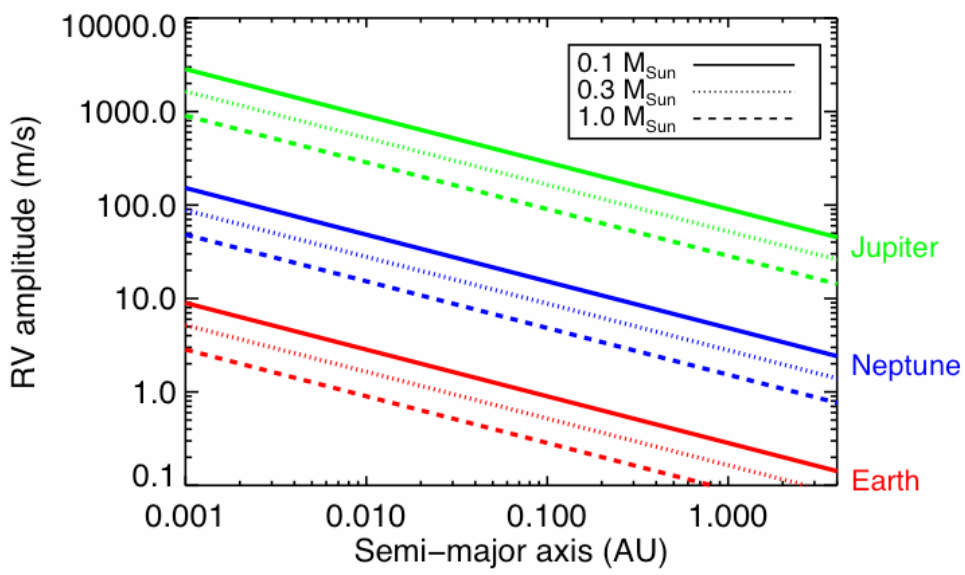

Figure 5-1 RV amplitude as a function of separation for planets around host stars of various masses. Different colours correspond to different planet masses, while different line styles correspond to different host-star masses.

This approach to extend RV surveys to even lower-mass planets, well into the realm of terrestrial planets, is to search around lower-mass primary stars since the RV reflex signal will be larger for lighter primary stars (see Figure 5-1). Circumstellar disks appear to be common around young (few Myr) low-mass stars and brown dwarfs (e.g. Liu, Najita & Tokunaga 2003), naturally raising the question of whether these objects can form planets and, if so, how their planetary systems compare to the well-studied systems around solar-type stars. Since 8 out of 9 stars in a volume-limited sample are M dwarfs, it is imperative to assess the planet-bearing frequency of what may be the most common sites of extra-solar planetary systems. In fact GJ876d and the microlensing detection of the distant 5 Earth-mass exoplanet OGLE-2005-BLG-390Lb (Beaulieu et al. 2006) shows that exoplanets near terrestrial-mass do exist. Thus a major new frontier in exoplanet research is to find and characterise the local examples. Apart from their proximity M dwarfs are particularly interesting because they offer the possibility to detect terrestrial mass planets in their habitable zone. Optical RV surveys are restricted to stars more massive than about M4 dwarfs (~0.3 $M_{\odot}$). Very nearby, lower mass M dwarfs are optically too faint. One way to search for planets around later type M dwarfs and even brown dwarfs is to make radial velocity measurements where the stars are bright, that is, in the infrared.

In this science case proposal we examine the scientific appeal of doing precision RV surveys in the NIR and based on the radial velocity information in M dwarf spectra formulate a potential survey that might be carried out. Apart from precision radial velocities we envisage an instrument that has sufficient throughput and wavelength coverage to be of interest to the wider Gemini community and thus give details of other cutting-edge science that might be conducted. Given that the feasibility of doing precision RV surveys in the NIR has yet to be established we describe and present latest results from our practical pathfinder experiment. In order to build the best radial velocity instrument feasible we also consider the instrumental stability and calibration requirements.

5.1 BASELINE EXPECTATIONS

A lack of massive planets around M dwarfs has been a suspicion for a number of years (e.g., for Jupiter-mass planets see Endl et al. 2006). Samples from individual teams are relatively small and usually not given high priority amongst the queue of Solar analogues giving high signal-to-noise observations. When all optical surveys are taken together it may be possible that there is indeed a lack of Jupiter-mass planets around M dwarfs in comparison with Solar analogues. The most complete analysis of the problem has been done by Endl et al. (2006); however, this analysis did not account for metallicity and rejected GJ876 because it was already known to host planets. Nonetheless, since Solar Systems are broadly expected to scale with the mass of the hosts this is perhaps not surprising. Kornet, Wolf & Rozyczka (2006) indicate that the set of protoplanetary disks capable of giant planet formation may actually be *larger* for less massive stars. Provided that the distribution of initial disk parameters does not depend too strongly on the mass of the central star, they predict that the percentage of giant planets should increase with decreasing mass.

Nonetheless some simulations of the core-accretion model indicate that Jovian-mass planets are rare around early-M dwarfs because rocky cores do not grow fast enough but that planets up to ~10 $M_{\oplus}$ should be common (Laughlin et al. 2004, Ida & Lin 2004b, 2005). Therefore, achieving very high RV stability seem very desirable: according to the models, a detection threshold of ~25 m/s (RMS ~5 m/s) is unlikely to detect anything, while a ~10 m/s threshold (RMS ~ 2 m/s) should detect many terrestrial planets around low-mass stars. This assumes that the detection threshold is 4-5 sigma i.e. that a precision of 2m/s gives a threshold of 10 m/s. This is true for periods which are long compared to the measurement baseline. For earth-mass planets around M dwarfs the periods are days to months so we might get to thresholds closer to the precision (Narayan et al, 2005).

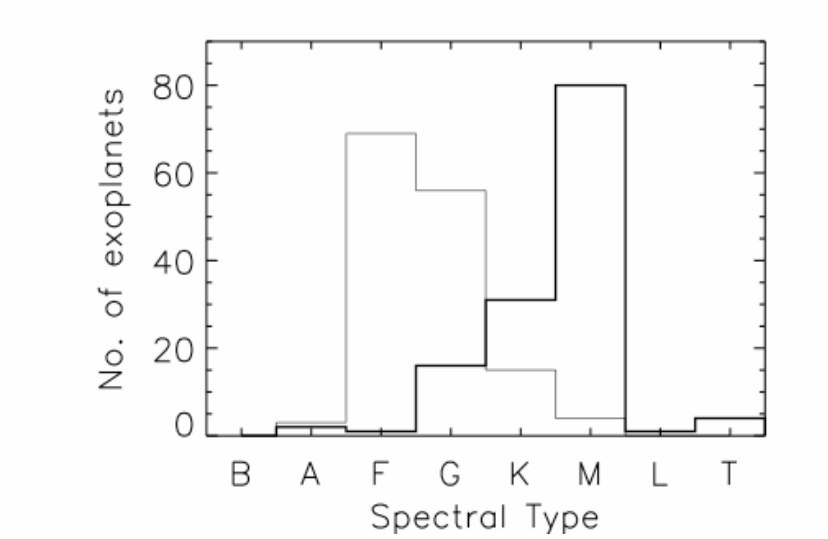

Figure 5-2 Number of exoplanets known per spectral type based on exoplanets.org is shown with thin solid line. The thick solid line shows the breakdown of stars within 10pc from RECONS (http://www.chara.gsu.edu/RECONS/TOP100.htm). While M dwarfs dominate the Solar neighbourhood few exoplanets have been discovered in orbit around them.

An infrared RV survey will survey stars which span a mass range of at least a factor of 5, from ~0.08–0.4 $M_{\odot}$. This is comparable to the mass range currently being surveyed by current optical RV programs (~0.4–1.5 $M_{\odot}$) and illustrates the significant parameter space to be explored by PRVS. We discuss three major scientific areas to be addressed by a PRVS survey.

1. **Testing theories of giant and terrestrial planet formation:** Extending the planet census to mid/late-M and L dwarfs will be a powerful and novel avenue for testing planet-formation theories. By probing host stars and planets of much lower masses, PRVS will address some of the key theoretical questions, in particular towards identifying the dominant physical processes that shape planet formation.

   Core-accretion models predict a rapid rise in the number of planets below ~10 $M_{\oplus}$, as more massive planets would have rapidly accreted gas and grown to much larger masses. PRVS will *directly test* the current paradigm by having the sensitivity to find these sub-critical rocky cores and to determine the critical core mass, as well as its dependence on host star mass. Similarly, current models predict few 10–100 $M_{\oplus}$ planets at separations inside 3 AU (the "planet desert"; Ida & Lin 2004a). This mass range reflects the planet mass needed to start and end runaway gas accretion, while the outer ~3 AU radius is tied to the timescale for gas accretion and the protostellar disk lifetime. Therefore, determining the locus of the planet desert for low-mass stars and brown dwarfs in comparison to solar-mass stars will be a key test of the theory.

   The orbital radius at which ice condenses ("the snow line") scales as $\sqrt{L_{Star}}$, and hence for a given RV survey, the time baseline needed to reach the snow line scales as $L^{3/4}$. In other words, infrared RV surveys of ultracool dwarfs reach the snow line ~100× quicker than optical surveys of Solar-type stars. The surface density of grains is much enhanced outside the snow line, which is expected to lead to enhanced planet formation and a sharp rise in planet frequency outside this radius (Lissauer 1987; Pollack et al. 1996). For a similar reason, stars with higher metallicities are expected to more readily form terrestrial planets. PRVS can test these ideas by assembling a populous sample of terrestrial planets around stars with a wide range of masses and metallicities.

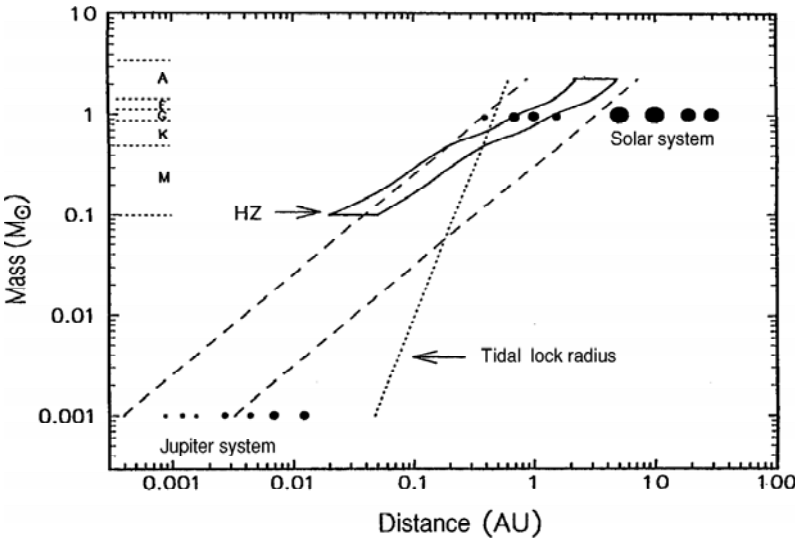

Figure 5-3 Habitable zone as a function of stellar mass (Kasting et al 1993). The "HZ" box shows the habitable zone. The dotted line represents the distance within which a planet's rotation is predicted to become tidally locked in 4.5 Gyr. The long dashed lines are a simple estimate of the probable terrestrial planet accretion zone. In the case of M dwarfs, the habitable zone resides at ~0.01-0.3 AU, and a dedicated infrared RV survey can find terrestrial planets at such separations.

2. **Searching for terrestrial planets in the habitable zone:** M dwarfs are the most common type of stars and in principle could represent the most common hosts of planetary systems. The habitability of these systems is the subject of increasing interest (e.g. Turnbull & Tarter 2003 and references therein). Given the exceptionally long main-sequence lifetimes of such low mass stars, any terrestrial planets would have abundant opportunities to develop life, and perhaps technologically advanced civilization.

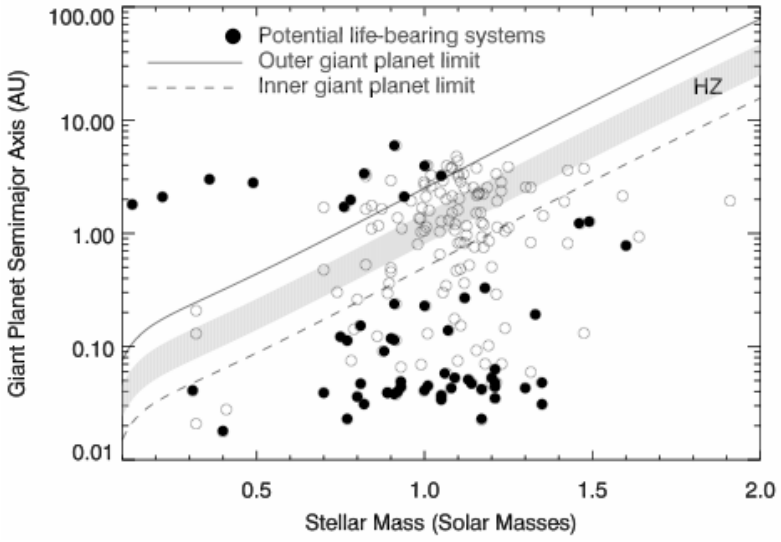

Figure 5-4 The 'modern' plot showing planet orbital parameter space that allows terrestrial planets to form in the Habitable Zone. The solid line indicates the limit for outer giant planets from Raymond et al. (2006). The dashed line is an approximate limit (0.5 AU with eccentricity less than 0.1 - the maximum eccentricity achieved in most simulations - for a solar-mass star) inside which low-eccentricity giant planets allow for the formation of habitable planets, derived from our results. The Habitable Zone (shown shaded), was calculated by assuming the temperature to scale with the stellar flux (i.e., the square root of the stellar luminosity), using a stellar mass-luminosity relation fit to data of Hillenbrand & White (2004). Open circles represent known giant planets that are unlikely to allow habitable terrestrial planets in the Habitable Zone. Filled circles represent known planets with low enough orbital eccentricities to satisfy our criteria for habitable planet formation, deemed to be potentially life-bearing.

Due to their low luminosities, the habitable zone (HZ) around ultracool dwarfs is much closer to the central star than for solar-type stars (Figure 5-4). Close-in planets around M dwarf will likely be synchronously rotating due to tidal forces (Dole 1964), and hence stellar insolation will occur on only one hemisphere. Kasting et al. (1993) suggested this would be hostile to life, since the dark-side of the planet could initiate permanent freeze-out of water and other volatiles. However, more recent work has suggested that only a small amount of gaseous CO2 is needed to prevent this atmospheric collapse, and a fairly dense atmosphere could lead to efficient heat transport over the entire planet, allowing the presence of liquid water (Joshi, Haberle & Reynolds 1997).

For the M dwarfs, the estimated habitable zones are at separations of ~0.01 to ~0.3 AU, well suited for the PRVS survey. Sensitivity to terrestrial planets in the HZ is essential, since gas giant planets in the HZ are unlikely to support life (though their rocky moons might). Figure 5-5 shows the planet mass detection threshold for a given RV sensitvity as a function of orbital radius and host star mass. Note that for 0.5 $M_{\odot}$ star (which correspond

to spectral type M0), even the most massive habitable terrestrial planets (10 $M_\oplus$) induce an RV signature of only ~2 m/s. However, for the case of a 0.1 $M_\odot$ star (M9), an RV sensitivity of 8 m/s is sufficent to detect planets of >4 $M_\oplus$ within the HZ. Therefore, for a given RV sensitivity limit, detection of terrestrial planets in the HZ of other stars is most feasible around the lowest mass primaries.

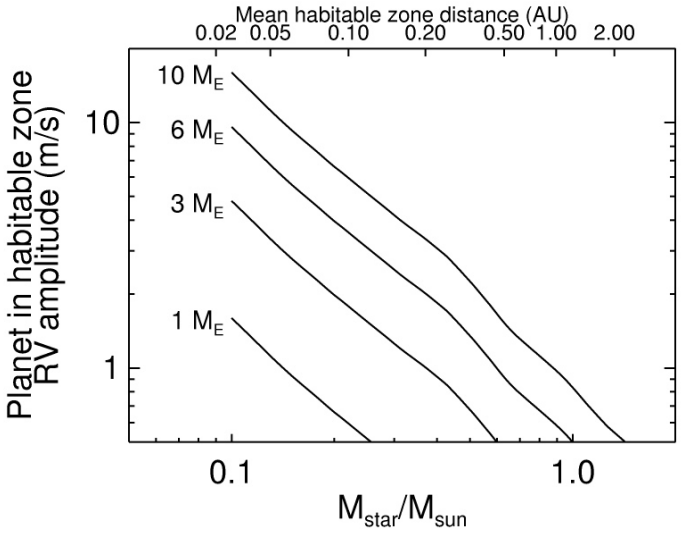

Figure 5-5 RV amplitude for terrestrial planets in the habitable zone, as a function of stellar mass. The mean distance of the HZ as a function of stellar mass is taken from the work of Kasting et al. (1993) and is indicated on the top axis. For solar-type stars, even the most massive terrestrial planets have an essentially undetected RV signature. For low-mass stars, the lighter primary stars and lower luminosities mean that habitable terrestrial planets can be detected.

3. **Detecting massive large-separation planets around low-mass stars:** Jupiter-mass planets at large separations around low-mass dwarfs will be detectable due to their large RV reflex amplitude (`Figure 5-4`) though their long periods will impede precise determination of M sin i. Such planets are relevant for the issue of habitability, since massive planets can shield inner terrestrial planets from life-threatening intensive bombardment by comets. Furthermore, such long-period planets identified by PRVS will be among the most promising targets for direct imaging of extra-solar planets. By virtue of the low luminosities of the primary stars, it will be much easier to directly image the thermal emission from the planets, through both imaging and spectroscopy. The near-IR contrast ratios are as favourable as 10–15 mag (Baraffe et al. 2004).

   These wide, massive planets would be appealing targets for high-contrast AO imaging using laser-guide stars (since in most cases the primary stars will be too faint to serve as their own wavefront references). From space, the *James Webb Space Telescope* would be a ready capability for direct imaging. Jovian-mass planets are expected to be rare around VLM stars and brown dwarfs in the standard core-accretion models of planet formation; however, such massive planets might form by other mechanisms, e.g. the case of the ~5 $M_{Jupiter}$ companion to the young brown dwarf 2MASSW,J1207334-393254 (Chauvin et al. 2005). Even though such objects might not be considered as `true' planets, since they likely did not form in a disk, such objects would be valuable templates for studying the physical properties (L_{bol}, T_{eff},

SEDs and spectra) of very-low-mass objects in the planetary-mass regime. In addition, combining the imaging and RV datasets provide a stronger constraint on the companion mass than either dataset alone (e.g. Liu et al. 2002).

5.1.1 Infrared radial velocity survey of brown dwarfs

What would we expect, if we go to even lower masses, planets of brown dwarfs? If planets can only form by core accretion, one would expect to find only planets of very low mass (~0.01 M_{Jup} or a few $M_{\oplus}$ in this case). Likewise, one may argue that brown dwarfs resemble Jupiter and we might expect to see only Io or Ganymede-type objects. Again this implies that brown dwarfs should have planets of only a few $M_{\oplus}$ (Desidera 1999). However, even such planets could be detected with an accuracy of RV-measurements of 5 to 10 m/s (`Figure 5-6`). On the other hand, one may argue that brown dwarfs (BD) should have massive planets, simply because there are many BD-BD binaries and the mass-ratio between a brown dwarf and a massive planet is only ~1:10. Since for field objects there is no break in the initial mass function at 13 M_{Jup}, such "BD-planet binaries" could be possible. The best evidence for the existence of such objects is 2MASSW,J1207334-393254 (Chauvin et al. 2005). If brown dwarfs have massive planets, we would thus expect there is no correlation with metallicity, as these planets would not have been formed by core-accretion.

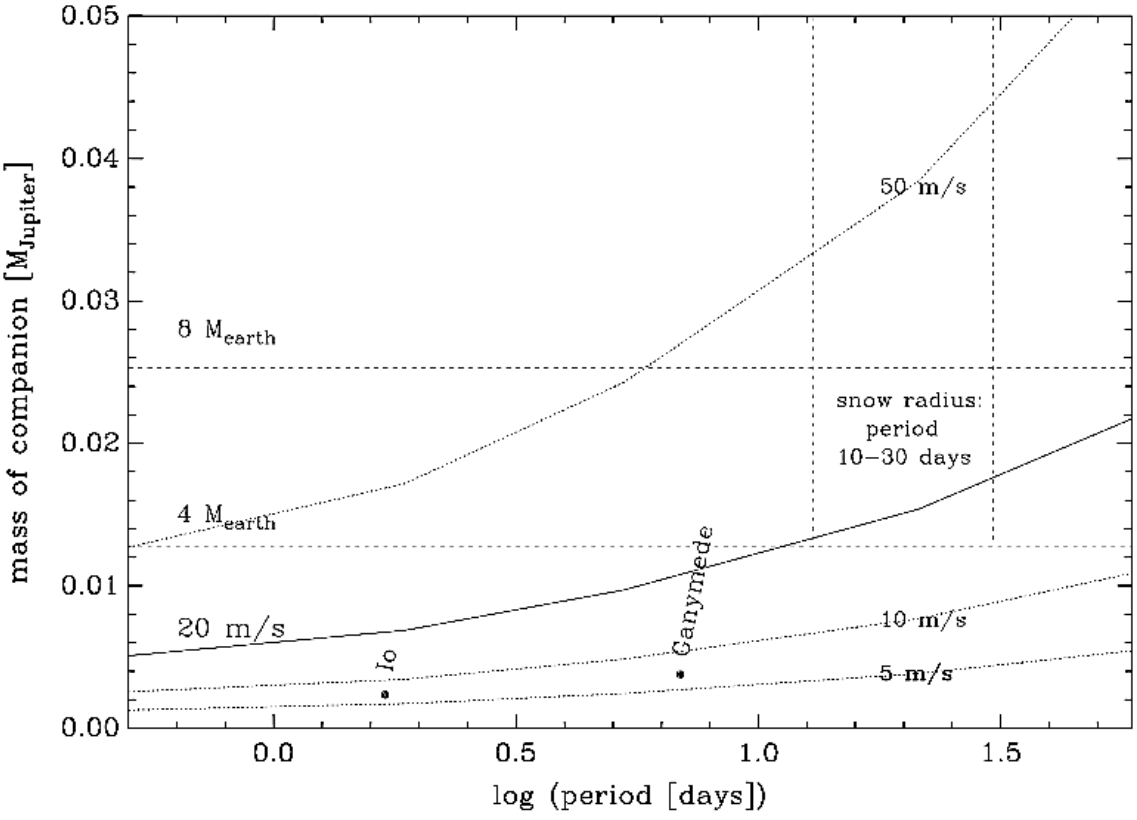

Figure 5-6 Guenther et al. (2006) shows the semi-amplitude of the RV-variations caused planets orbiting BDs. A BD of 40 M_{Jup} is assumed. Planets of only a few earth-masses could be detected if an accuracy of 20 m/s is achieved. An accuracy of 5 m/s is required in order to detect objects analogue to Io and Ganymede. In the case of the disk of a BD the ice-line would correspond to an orbital period of only 10 to 30 days.

5.1.2 Synergy of optical and infrared RV surveys

In many ways, optical and infrared surveys will provide complementary information about planetary systems, each covering different regions of the stellar mass, planetary mass, and semi-major axis parameter space. Optical RV surveys will have had a ~15-yr head start by the time PRVS is commissioned. However, the rate of planet detection for PRVS might be accelerated compared to those surveys:

- The planetary mass function around solar-type stars steeply rises to lower masses, with $dN/dM \propto M^{-1}$ to M^{-2} (Tabachnik & Tremaine 2002; Lineweaver & Grether 2003). Since the RV reflex amplitude scales as $M_{planet}/\sqrt{M_{star}}$ achieving comparable velocity precision in the IR for ultra-cool dwarfs compared to the optical studies of Solar-mass stars means that lower mass, and hence many more, planets can be detected.
- Optical RV surveys are just beginning to explore the region past the snow line around Solar-type stars (3 AU). The radius of the snow line scales as $\sqrt{L_{Star}}$, and hence for a given RV survey, the time baseline needed to reach the snow line scales as $L^{3/4}/\sqrt{M_{Star}}$. In other words, infrared RV surveys of ultra-cool dwarfs reach the snow line ~100× quicker than optical surveys of Solar-type stars. Therefore, PRVS will immediately begin to probe the orbital separations most favourable for planet formation.

Our infrared RV survey will survey host objects which span a mass range of a factor 4–5, from ~0.08–0.4 $M_{\odot}$. Hence, our infrared RV survey will span a range of host star masses comparable to the current optical RV surveys, illustrating the significant parameter space to be explored by the PRVS. The combination of optical and infrared RV surveys will measure the planetary-mass function, orbital distribution, and frequency over a broad range of central star mass, and thereby provide the necessary data for direct confrontation between models and observations.

5.1.3 Connections to high contrast, direct imaging searches

A five-year PRVS survey will probe to about 1 AU separations around 0.1-$M_{\odot}$ stars. However, as noted above, PRVS will also be sensitive to planets at even larger distances, but since the time baseline will be shorter than the orbital periods, mass (M sin *i*) determinations will not be possible. These planets will reveal themselves as long-term velocity trends in their host stars.

Such long-period planets uncovered by PRVS will be among the most promising targets for direct imaging of exoplanets. For direct imaging, the required contrast ratio depends on the star's brightness, which is very non-linear with the mass. For instance, in bolometric luminosity, a 0.1-$M_{\odot}$ star is 1000× fainter than a 1-$M_{\odot}$ star. Thus, by virtue of the low luminosities of the primary stars, it will be much easier to detect the thermal emission from the planets, through both imaging and spectroscopy.

The near-IR (1–5 μm) emission of gaseous planets is enhanced by many orders of magnitude over the expected blackbody emission, due to the water and methane molecules that dominate the opacities. For Jovian-class planets, the contrast ratios are as favourable as 10–15 mag at these wavelengths (Baraffe et al. 2004). Several high-contrast adaptive optics systems on ground-based 8–10-metre-class telescopes will be available for imaging. The primary stars will be too faint to serve as wave-front references, but sodium laser guide stars would be readily available by then. From space, the *JWST* would be a ready capability for direct imaging. The coronagraphic version

of *TPF* (*TPF-C*) would also be a possibility; however, the contrast gains for imaging planets in scattered light will not be nearly as much as for imaging in thermal emission.

Jovian-mass planets are expected to be rare around VLM stars and brown dwarfs in the standard core-accretion models of planet formation, since the disk masses and planetesimal growth times in low-mass disks are too slow to build the large rocky cores needed for runaway gas accretion (Laughlin et al. 2004; Ida & Lin 2004b). However, such massive planets might form by other mechanisms, e.g. disk instability.

Strong circumstantial evidence for massive planets around brown dwarfs comes from the recent discovery of a candidate planetary companion to the young brown dwarf 2MASSW,J1207334-393254 by AO imaging (Chauvin et al. 2004). If confirmed, the companion would have a mass of only 5 $M_{Jupiter}$ and a separation of 60 AU. Such an object almost certainly did not form in a circum-stellar disk, but nonetheless it demonstrates that massive planets might form around brown dwarfs, perhaps from direct fragmentation during the proto-stellar collapse phase. Even though such objects might not be considered as "true" planets, since they did not form in a disk, finding such objects would be extremely valuable for studying the physical properties (L_{bol}, T_{eff}, SEDs and spectra) of very-low-mass objects in the planetary-mass regime. While the orbital separation of 2MASSW,J1207334-393254 B is too far out to induce significant RV signal, such objects at a few-AU separations would induce long-term RV trends that could easily be identified by PRVS. These objects would be then prime candidates for direct detection at IR wavelengths by ground-based and space-based high-contrast imaging systems. The combined imaging and RV datasets provide a stronger constraint on the companion mass than either dataset alone (e.g. Liu et al. 2002).

5.1.4 Connections to transit surveys

A terrestrial planet transiting a VLM star/brown dwarf would produce a photometric transit signature of 1–2%, easily detectable (and a factor of ~20–100× larger than such a planet transiting a solar-type star). On the timescale of PRVS, COROT and Kepler missions as well as ground-based surveys such as the UKIDSS and VISTA M dwarf transit search are expected to produce a large number of events to follow-up (e.g. Pinfield, Jones & Steele 2005). Given the expected dominance of M dwarf host stars in all of these samples, PRVS will be the most efficient (and in many cases the only) instrument capable of follow-up. Such transit and radial velocity data will provide the most exacting test for models of exoplanets (e.g., Sato et al. 2005) and importantly along with the transit data now been acquired for Solar type stars (e.g., Deming et al. 2005) will provide substantial coverage of the available parameter space for exoplanet characteristics.

5.1.5 Expectations for PRVS scaling from optical surveys of solar-type stars

Despite the stunning success of the optical radial velocity technique in finding exoplanets we have only scratched the surface of the plausible exoplanet parameter space. While dramatic progress has been made in understanding of planet formation, the predictive capability of the new theories is far from established. While series of papers such as the 'Deterministic model of planet formation' (Ida & Lin 2005) are rapidly assembling a big picture many important theoretical and empirical input variables are not known so there is scepticism as to their utility. The *most conservative* indicator for what we might expect from a PRVS survey of low-mass stars would thus seem to come from a simple scaling of findings from optical surveys.

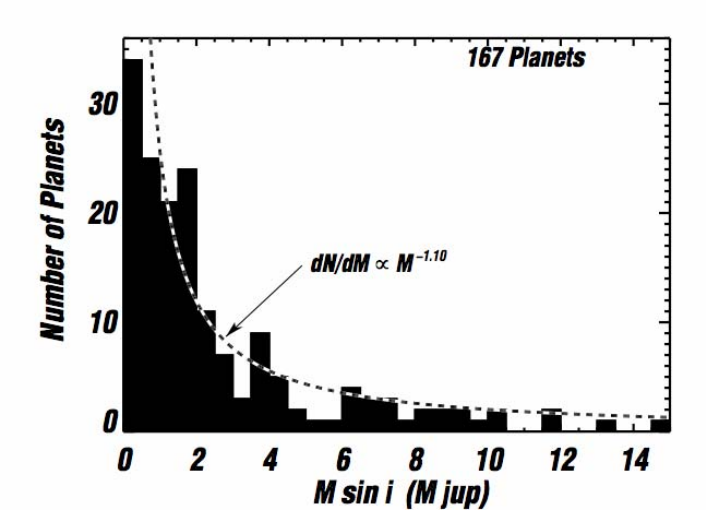

Figure 5-7 Minimum mass distribution of 167 known nearby exoplanets with M sin i < 15 M_{Jup} from Butler et al. (2006). The mass distribution shows an increase in the number of planets at lower masses that is roughly characterized by a power law, dN/dM ~ $M^{-1.2}$. Lower mass planets have smaller Doppler amplitudes, so relevant selection effects mean that this result is a lower limit on the number of lower-mass planets. This distribution represents results from many surveys, and so is drawn from an inhomogeneous sample.

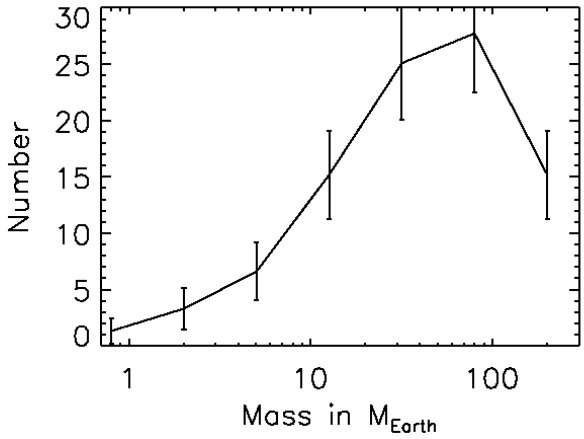

Figure 5-8 Predicted counts from 5 year PRVS M dwarf survey based on a rescaling of the previous figure but with a logarithmic x axis. It is derived from the exoplanet catalogue of Butler et al. (2006) with orbital periods of >5yr removed. The plot has been scaled in mass to move from detection around Solar type stars (median value 1.1 $M_\odot$) to detection around 0.15 $M_\odot$ (~M4 which corresponds to approximately the mean mass of a baseline PRVS M dwarf survey) and from precision of 3m/s to 1m/s. The expected number has been reduced by a factor of 0.66 on the basis that PRVS will only have access to a single hemisphere. The fall in expected planets towards lower mass is due to observational bias and is analogous to that seen in the current exoplanet catalogues. The plot is based on results from many surveys and is thus drawn from an inhomogeneous sample. The error bars are based on (number)$^{1/2}$ statistics and are only indicative. Of the PRVS exoplanets discovered with <10 $M_\oplus$ we expect that approximately 50% would be found within their habitable zones (based on the 12/25 known exoplanets with < 0.314 $M_{Jupiter}$ being found with 0.1AU of their host stars). This is likely to be a conservative assumption as simulations suggest that size will scale with mass (see text for details).

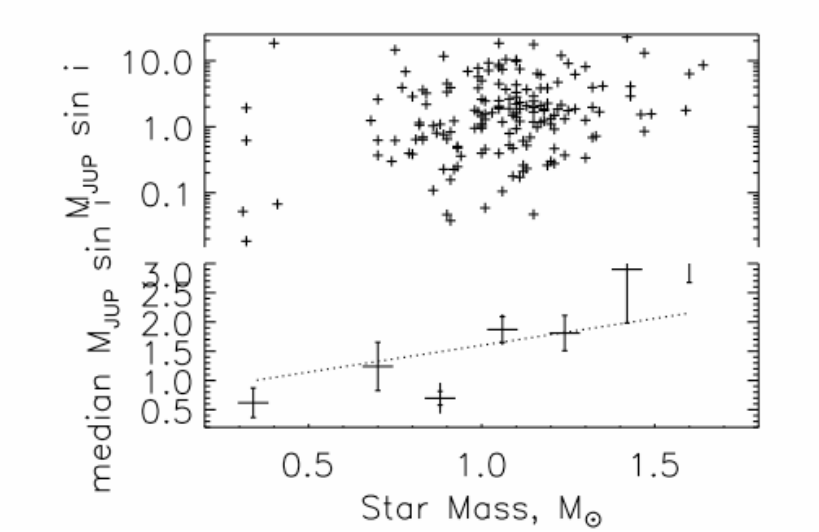

Figure 5-9 The upper plot shows the masses of exoplanet host stars plotted with respect to the mass of their exoplanets. The lower plot shows a binned version of the data. It can be seen that there is a probable trend of lower mass planets being detected around lower mass primaries. The dotted line shows the expectation if planet mass scales with host star mass. The plot is based on the data in Butler et al. (2006). It shows results from many surveys and is thus drawn from an inhomogeneous sample. The error bars are based on (*number*)$^{1/2}$ statistics and are at best indicative.

Several groups are now starting to predict a significant population of Neptune to Earth-mass rocky bodies around low mass stars (eg Laughlin, Bodenheimer & Adams, 2004). Ida & Lin (2005) find that planets around M dwarfs will migrate prior to fully accreting gas and so there should be a relative abundance of *close-in* low-mass (<Neptune) planets around these stars. This is consistent with simulations based on Grether & Lineweaver (2006) and Ailbert et al. (2005). Though the theoretical expectations are that Earth mass exoplanets should be proportionally more common around M dwarfs than around Solar type stars, theoretical predictions in this field are still in their infancy and so scaling from existing optical surveys is probably the most conservative prediction. However, we won't know for sure unless we try!

5.2 RADIAL VELOCITY INFORMATION IN M STAR SPECTRA

To date, most searches for planets around nearby stars have been carried out using radial velocity measurement techniques in the optical regime on solar-type (FGK) stars. These searches have found planets with masses of 0.02-180 $M_{Jupiter}$ (Butler et al. 2006). However there is great interest in searching for even lower mass planets (terrestrial planets, with M ~ $M_\oplus$, or 0.003 $M_{Jupiter}$). Since the amplitude of the reflex motion (the quantity measured in radial velocity observations) K scales as $m_{planet}/(M_* + m_{planet})^{0.5}$, the largest radial velocity signal produced by terrestrial planets will be observed for the lowest mass primaries. This naturally leads to searches for

planets around M- and L-type stars. Because the spectra of such stars peak in the near-infrared (NIR), with very little photon flux in the optical (Figure 5-10), it would seem natural to extend the radial velocity technique to near-infrared wavelengths. However, the question arises: **how much Doppler information is intrinsically present in the NIR spectra of these stars, relative to the optical?**

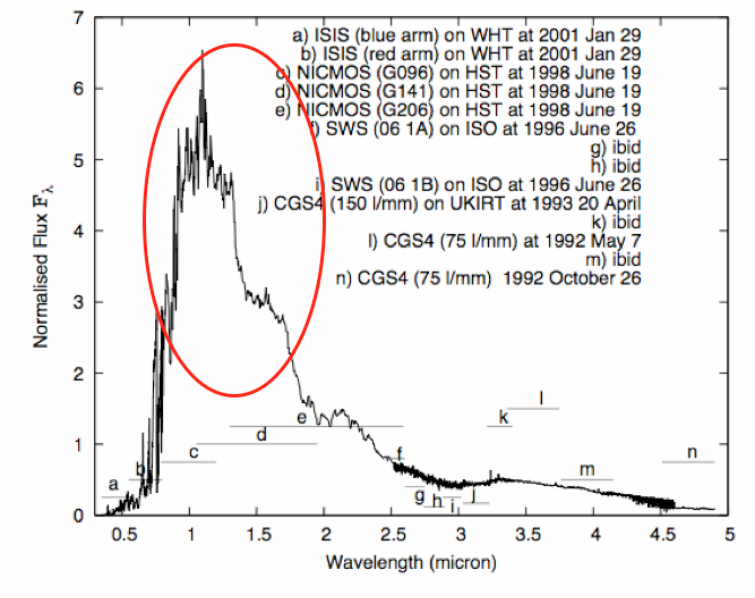

Figure 5-10 The observed spectral energy distribution for GJ406 (M6V) from Pavlenko et al. (2005). The spectral region available to PRVS is highlighted by the red oval.

It has long been realised that M dwarf spectra are rich in spectral information. Below around 3500K (~M2V) molecules form at depths corresponding to the stellar photosphere and a rich forest of lines can be seen at high resolutions. While the spacing of atomic lines increases toward the infrared for all spectral types in the infrared region M dwarfs and cooler objects exhibit plenty of molecular features which dramatically carve up the spectrum. The following Figures (Figure 5-11 to Figure 5-13) show example spectral regions of different M spectral types compared with synthetic spectra. Each of the spectral regions shows a few deep atomic lines, though the majority of the features in all cases are molecules. In general terms the quality of atomic and molecular data in the infrared is rather poor in comparison with optical line lists. Nonetheless Figure 5-13 indicates that some spectral regions (particularly those dominated by water) are fit rather well. Although there are others such as Figure 5-12 where representative molecular opacities, in particular for the metal hydrides are missing and fits are rather poor.

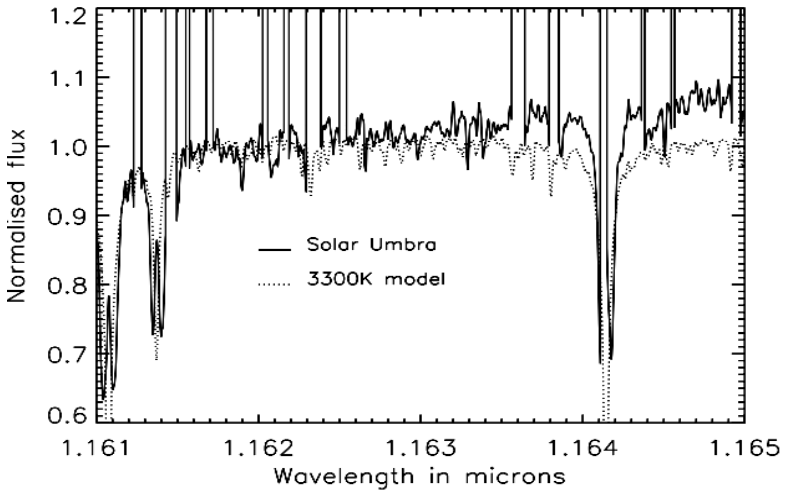

Figure 5-11 Solar Umbra spectrum (solid line) from the McMath Solar Telescope (Wallace et al. (1993) compared to 3300K model (dotted line). At these temperatures features are reasonably well modelled by the Phoenix model atmospheres (Bott & Hauschildt 2005). The regions of Solar Umbra given by straight lines going up to the top of the plot are ones for which telluric contamination means these sections have been ignored.

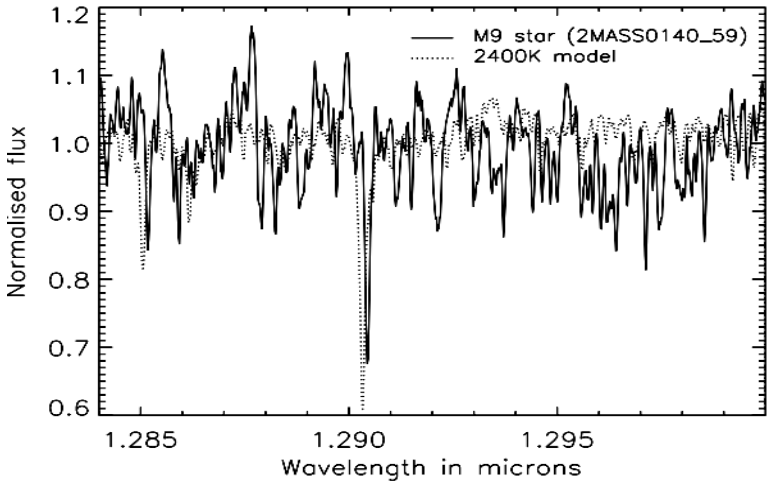

Figure 5-12 The M9V star (solid line, 2MASS0140_59 from Mclean et al., in preparation) *v* sin *i* = 6.5 km/s compared to a 2400K PHOENIX synthetic spectrum (dotted line, from Bott & Hauschildt 2005). For spectral types later than M5 the J band spectral region is rather poorly modelled. This arises due to the relatively poor quality of the FeH line list. It should be noted that Lyubchik et al. (2006, A&A, submitted) find a very similar result though using a different synthetic spectral code and different water vapour line list (that of Barber et al. 2006 rather than that of Partridge & Schwenke 1997).

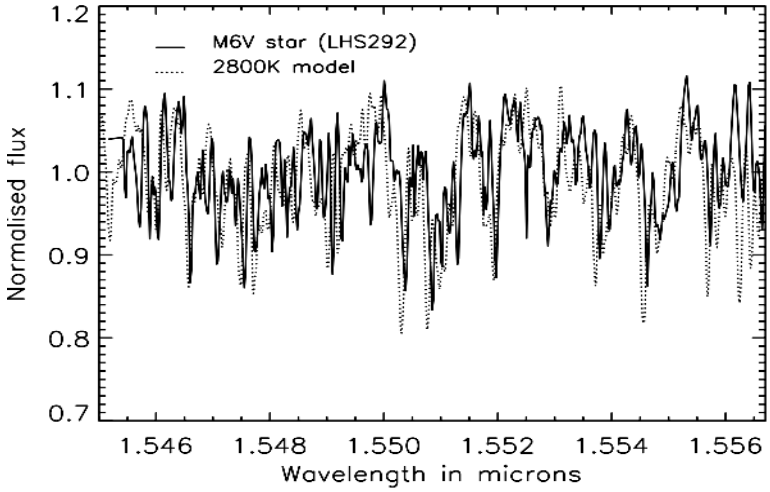

Figure 5-13 M6V star (solid line, LHS292) from Keck NIRES (Prato et al., in preparation) compared to a 2600K PHOENIX synthetic spectrum (dotted line, Bott & Hauschildt 2005). The H band spectral region appears to dominated by stellar water vapour which is relatively well modelled.

To answer the key question about comparison of the optical and infrared, we have followed the Fourier analysis presented by Erskine (2003). The Doppler information content in a spectrum $F(\lambda)$ depends on the number, width, and depth of the stellar features present and is related to the derivative $\partial F/\partial\lambda$. If the Fourier transform of F is given by f(k) for spatial frequencies k, then the Fourier transform of the partial derivative is given by $2\pi ikf(k)$. In Figure 5-14, we show the magnitude of the complex function ikf(k) for an M6V model spectrum (see below) for 5 spectral regions: V, Y, J, H, and K. In all cases, the Doppler information content in the spectra rises to a broad maximum and then falls off. As can be seen, the height of J-band curve is about the same as, while the Y -band curve is actually higher than, that of the V -band curve, which suggests that these band contain as much (or more) Doppler information as the V band. Overplotted on this figure are also lines corresponding to the Fourier transform of an instrumental SRF, idealized as a Gaussian, with resolving powers of R=20,000, 50,000, 70,000, and 100,000 (left to right). These curves indicate that a resolving power of $\geq$ 70, 000 is needed to capture the Doppler information contained in the broad peak. However, increasing the resolving power to 100,000 provides little additional gain, as this resolving power serves only to capture more information in the weak tail of the distribution.

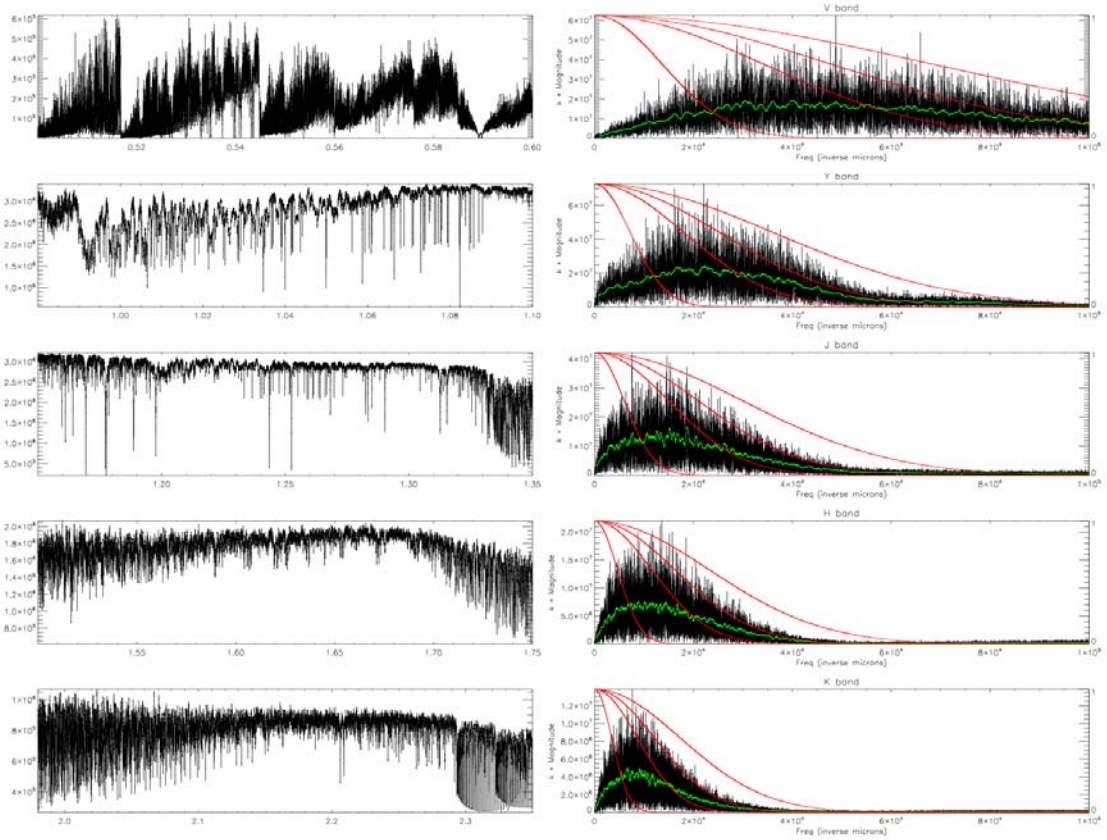

Figure 5-14 Doppler information in 5 spectral regions of an M6V star. On the left are the theoretical spectra for the regions and on the right are the Fourier transforms of the derivatives ∂F/∂λ as a function of spatial frequencies k. The overplotted curves are the transforms of Gaussian SRFs with R=20K, 50K, 70K, and 100K (left to right).

5.2.1 Computations

In order to assess the utility of radial velocity measurements of M dwarfs in the infrared we follow use the formulae provided by Bouchy et al. (2001; see also Connes 1985) to compute the theoretical Quality Factor (Q) and RMS velocity error (eta_v) for radial velocity measurements derived from various regions of the optical and NIR spectrum.

We have used the PHOENIX models of Hauschildt to generate estimates of both Q and εv for four standard near-infrared spectral regions [0.98-1.10 μm ('Y band'), 1.15-1.35 μm ('J band'), 1.50-1.75 μm ('H band'), and 1.98-2.35 μm ('K band')] for a range of M spectral types and a variety of resolving powers, pixel sampling, and rotational velocities. As a fiducial reference, we have also computed values for the wavelength region currently used by HARPS [approximately 0.5-0.7 μm ('V +R band')]. The computations are described below.

The important input parameters are the stellar model spectra, the instrument parameters, telluric absorption and stellar rotation; each of these is described in the following sections.

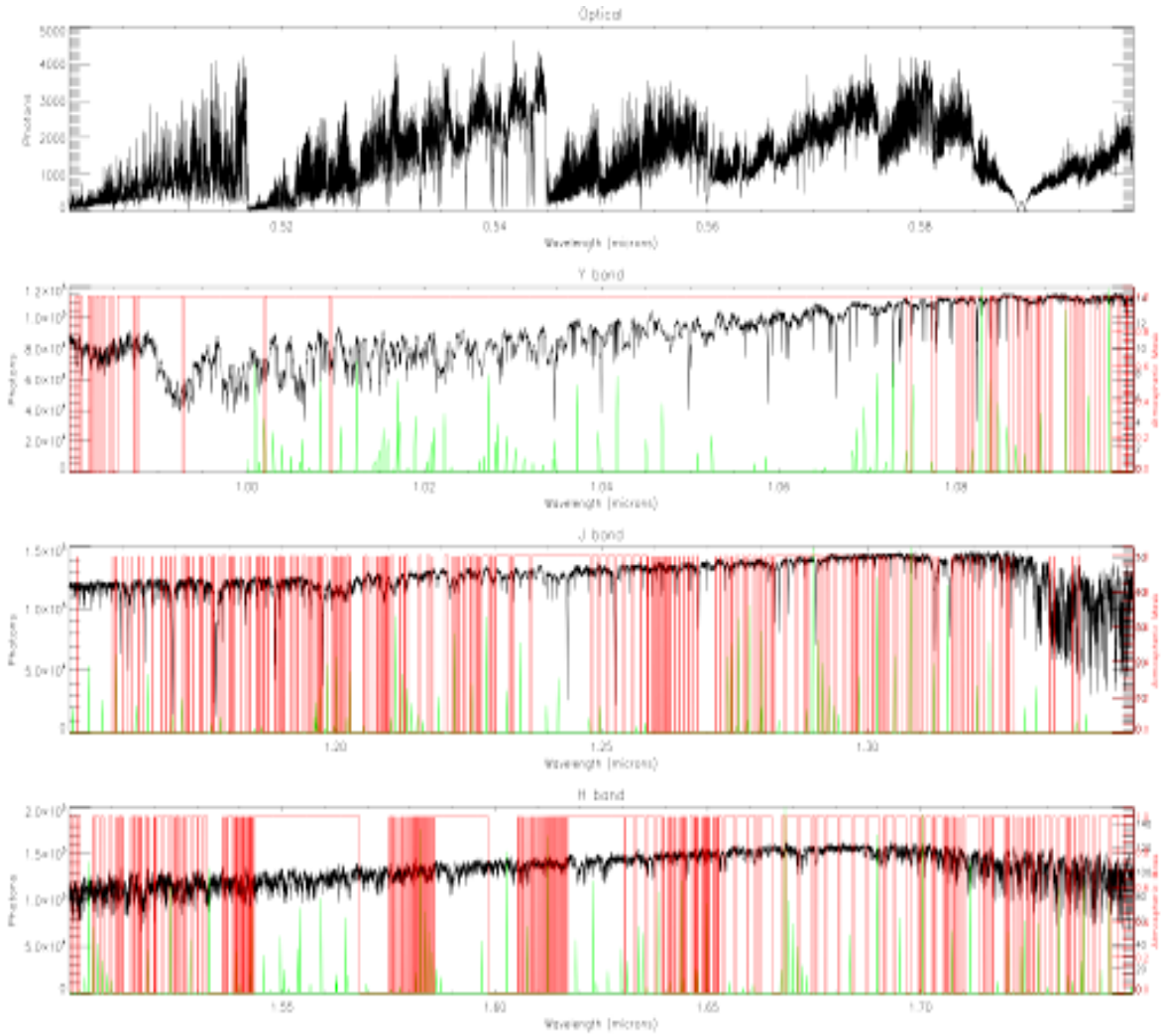

Figure 5-15 Synthetic spectrum of an M6V star, with J = 9 mag and v sin i = 5 km/s, 'observed' for 900 s on an 8-m telescope with a total throughput of 0.075, R=70000, and a pixel sampling of 2.5 pixels/FWHM. The telluric mask is overplotted. Only those points where the mask has a value of 1 were used for the calculations. The atmospheric transmission and OH emission lines are overplotted in red and green respectively. Note the variation in the y scale between the various spectral regions. The optical is shown at the top, and the lower panels are Y, J and H band.

5.2.2 Stellar Models

The theoretical spectra were computed by P. Hauschildt as part of the Gaia grid (Brott & Hauschildt 2005). They are PHOENIX, LTE, dusty models for Teff between 1400 and 3500 K, log g of 5.0, and solar metallicity. The models have a mean spectral sampling of 0.015 Å. We have converted the tabulated values of wavelength and flux to units of microns and W m-2 μm-1 and adopted the spectral type - Teff calibration from Jones et al. (2005) given in Table 1. For all the calculations presented here, the models were scaled to J = 9 mag. The spectral regions considered here are shown in Figure 5-15 for an example spectral type of M6V.

Table 1 Adopted Spectral Type - Teff Calibration

Sp Type	T_{eff} (K)
M0V	3800
M3V	3300
M6V	2800
M9V	2400

5.2.3 Instrument Parameters

Because the calculations require the number of detected photons from a given source, it is necessary to adopt some realistic instrument and observing parameters. We assumed that the observations consisted of a single 900 s exposure on an 8-m telescope. This yields a S/N of ~ 300 in each of the NIR bands. The total throughput was assumed to be 0.1 independent of wavelength. We have assumed that the resolving power of the instrument R and the sampling p (pixels per resolution element) are fixed, and therefore that the FWHM and (spectral) pixel scale $s = \lambda/(R \cdot p)$ vary linearly with wavelength.

Table 2 Percentage of Useable Spectrum

Band	Percentage			
(microns)	Gemini North		Gemini South	
	$\lvert v \rvert < 5$ km/s	$\lvert v \rvert < 30$ km/s	$\lvert v \rvert < 5$ km/s	$\lvert v \rvert < 30$ km/s
0.50-0.60 (V)	97	91	97	91
0.98-1.10 (Y)	96	87	93	79
1.15-1.35 (J)	67	34	57	27
1.50-1.75 (H)	86	58	81	51
1.98-2.35 (K)	52	24	44	18

Note. — For a zenith angle of 20 degrees, R = 70000, p = 2.5, and a limit of 98 % transmission. Gemini North was assumed to be at an elevation of 14000 feet and to have 2 mm of precipitable water vapour. Gemini South was assumed to be at an elevation of 8500 feet and to have 4 mm of precipitable water vapour.

5.2.4 Telluric Absorption

The effects of telluric absorption are accounted for in the calculations for the spectral regions by generating a telluric mask containing only 1's and 0's. For the NIR regions, atmospheric transmission spectra were generated with ATRAN (Lord 1992) with parameters appropriate for the Gemini North and South telescopes. The precipitable water vapour content was set to 2 mm for the former and 4 mm for the latter. For the optical spectra, we used the atmospheric transmission spectrum generated from solar observations at KPNO at various airmasses (Hinkle et al., 2003). The mask values were set to zero at all pixels where the mean transmission is less than 0.98. All pixels within $|v| < 30$ km/s of those set to 0 are likewise set to 0. This value corresponds to the highest velocity shift introduced by the earth's motion around the sun over a year. At all other points, the mask was set to 1. This mask is computed for each resolving power and pixel sampling. In Table 2, we list the percentage of each band that remains after masking out using this procedure for the two sites and for R=70K and p=2.5. We also give the percentage of the bands available for stars near the ecliptic pole ($|v| < 5$ km/s).

For the NIR results shown in this proposal, we used the NIR transmission spectrum valid for Gemini North. We have ignored the OH emission features in the calculations. Although they will certainly contaminate the observed spectra and reduce the number of pixels available for the radial velocity measurements, we have assumed that these features will be unresolved at all resolving powers. Therefore, they will remove only a few pixels in each spectral region and their effect on the calculations should be minimal. Furthermore, as long as these features are not saturated, their effects can be greatly mitigated by sky subtraction techniques.

5.2.5 Procedure

For each calculation, the model was 'spun up' by adding a specified rotational velocity. It was then smoothed to the requested resolving power by convolving with a Voigt profile (after resampling onto a wavelength grid that is evenly spaced in ln λ). The smoothed model was then 'sampled' by integrating over each pixel in the output wavelength array and converted to detected photons per pixel. We included a pixel response function that rose from 0.5 at the edges to 1 in the center and resulted in an effective pixel area of 0.85. An example of the resulting spectra for the M6V model is shown in Figure 5-15. At each pixel, the numerical derivative with respect to the wavelength is then computed (via a low-order Savitzky-Golay smoothing process [Press et al. 1992]). The quality factor Q and velocity measurement precision εv were then computed from the equations above, including the telluric mask values at each point in the summation.

5.2.6 Stellar Rotation

In order to take advantage of the resolution of a spectrometer it is desirable to measure the radial velocity of stars with the lowest possible values of $v \sin i$. This situation has been modelled and verified by experiment (e.g., Bouchy, Pepe & Queloz 2001) and predicts quite dramatic differences in precision. For example a 4500 K star with a $v \sin i$ =1 km/s is expected to produce a radial velocity precision 5 times higher than one with $v \sin i$ =16 km/s. While these relationships used for these simulations have not been verified for late type M dwarfs they are expected to be robust having been used for a wide-range of spectral types. For example, Galland et al. 2006) measured a doppler uncertainty of 65 m/s for β Pictoris ($v \sin i$ > 120 km/s, Abt 2000) in contrast to the expected uncertainty of 60 m/s (based solely on $v \sin i$ modulation of the Q factor). While $v \sin i$ information has not usually been available for most objects on planet search surveys, optical surveys have generally avoided the measurement of radial velocities for fast rotating objects by avoiding active stars. Nonetheless Figure 5-16 (upper panel) shows that exoplanets have been successfully discovered across a wide range of $v \sin i$ values. This result continues to be tested by the ongoing work of Galland et al. (2006).

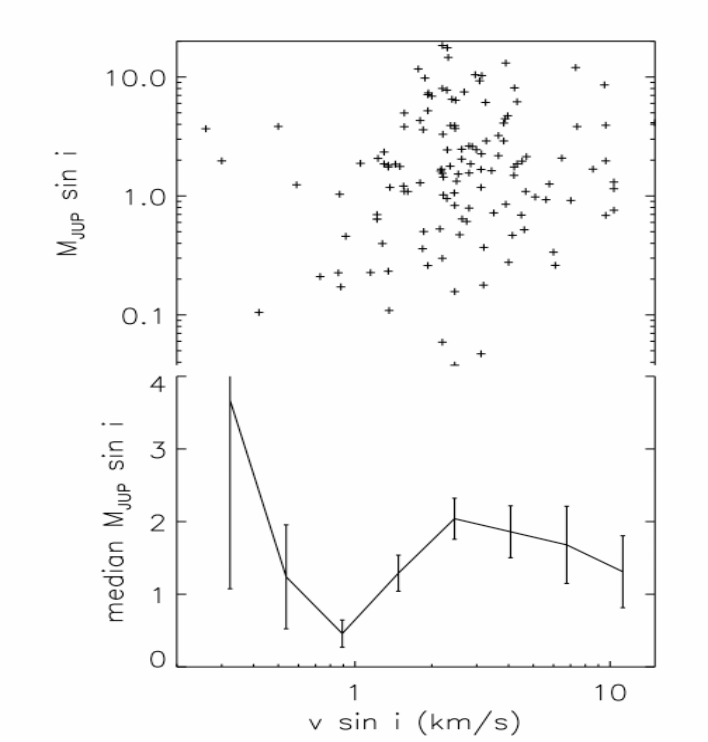

Figure 5-16 The upper plot shows the *v* sin *i* values for exoplanet host stars plotted with respect to the mass of their exoplanets (available for 135 exoplanets). The lower plot shows a binned version of the data. There does not appear to be a correlation between *v* sin *i* values of exoplanet hosts and the mases of their exoplanets. If *v* sin *i* was a limiting factor for the current radial velocity searches and thus setting a mass detection threshold we would expect to see exoplanet hosts with higher values of *v* sin *i* to host more massive exoplanets. The plot is based on the data in Butler et al. (2006). It shows results from many surveys and is thus drawn from an inhomogeneous sample. The error bars are based on (*number*)$^{1/2}$ statistics and are only indicative.

Given the nearly two orders of magnitude in *v* sin *i* values spanned by the known exoplanet host stars from optical planet search survey, it is instructive to consider the impact of *v* sin *i*. The lower panel in Figure 5-16 indicates that for the observed exoplanet host stars the expectation of on average finding higher mass planets around faster rotating stars is not yet seen. While it is possible that some enhancement of exposure times may have been in place for some surveys, in general *v* sin *i* values for potential planet host stars have been regularly determined.

5.2.7 Stellar rotation and spectral type

It is instructive to consider the fraction of low mass stars that might have *v* sin *i* values within the range of those for which exoplanets have been measured for Solar type stars.

It is well known that stellar evolution processes slow toward lower masses (e.g. Adams, Bodenheimer & Laughlin, 2005). This is also true for M dwarfs rotation. Relative to Solar type stars they have a relatively longer spin-down time and have relatively high values of rotation. Figure 5-17 shows how *v* sin *i* depends on spectral type, taken from published measurements. There is a sharp transition in *v* sin *i* at around a spectral type of M4 and a steady rise in *v* sin *i*

thereafter. Another way of looking at this is to plot the percentage of measured stars with low v sin i ; Figure 5-18 shows the percentage with v sin i <7km/s decreases below 50% for spectral type M5 and later, and is consistent with a random orientation of fast rotators by type M6. If one had to choose only a low v sin i sample of M dwarfs based on existing values of v sin i , it would only be possible to include a relatively small number of late-type dwarfs (later than M5). Consequently the probability of finding planets down to Terrestrial masses would be significantly reduced.

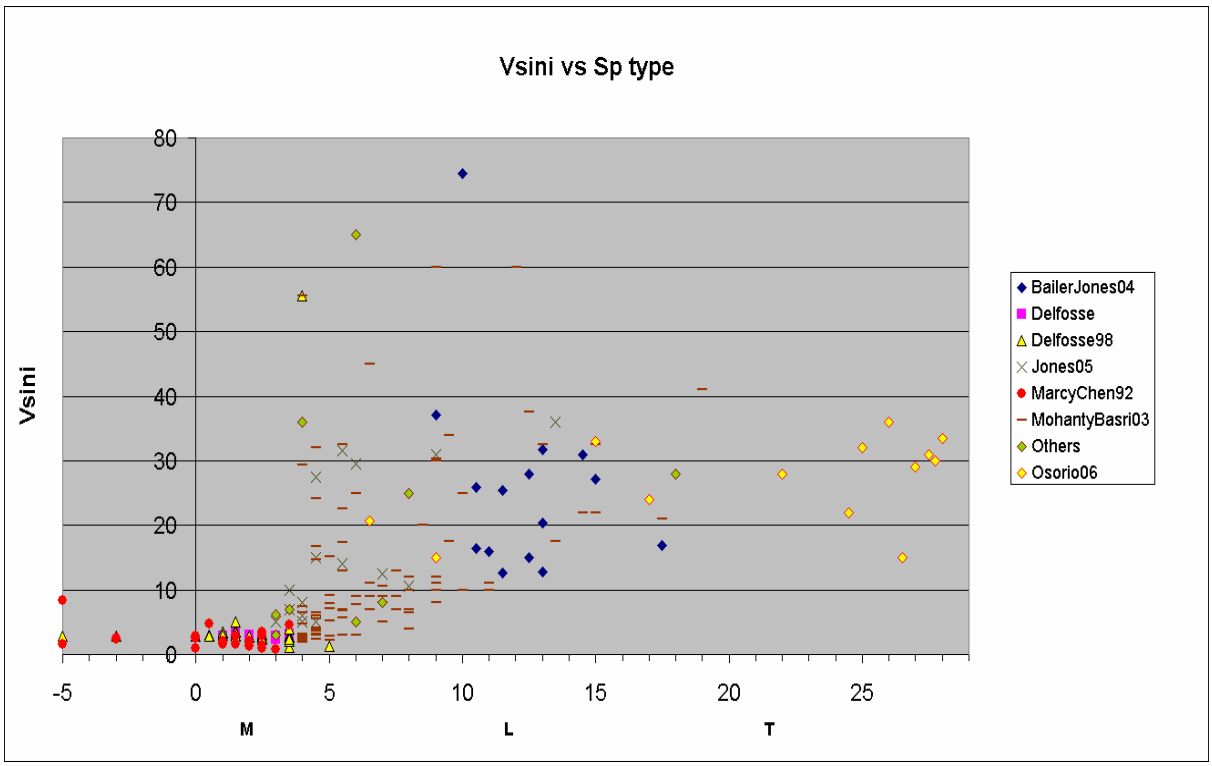

Figure 5-17 shows measured *v* sin *i* verses spectral type for M, L and T dwarfs in the available literature.

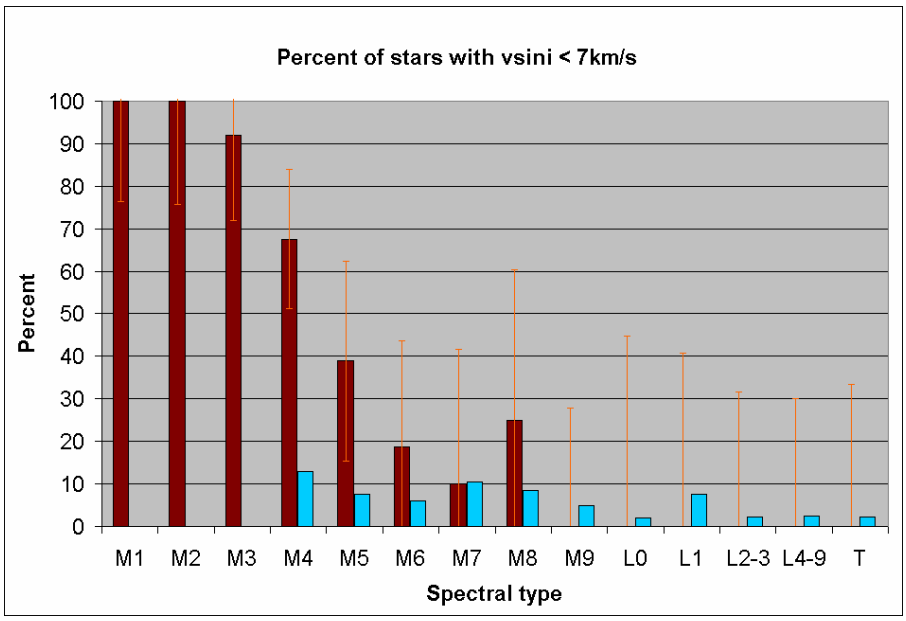

Figure 5-18 The percentage of stars with low *v sin i* (<7 km/s) is shown for a range of spectral types (brown histogram). The light blue histogram show the expected percentage assuming a random distribution of orientation angles. There appears to be sharp transition in *v* sin *i* at a spectral type of M4. The data is drawn from various different papers and thus is an inhomogeneous sample. The error bars are based on (*number*)$^{1/2}$ statistics and are only indicative.

5.2.8 Results

The figures shown below (Figure 5-19, Figure 5-20, Figure 5-21) present the results of the εv calculations as a function of rotational velocity for five values of the resolving power (R=20000, 50000, 70000, 100000, 150000) and three stellar models (M3V, M6V, M9V). We assume p=2.5. We considered v sin i between 0 and 30 km/s. As can be seen from the figures, the attainable velocity precision from each of the near-infrared bands can be nearly as high as that from the optical. In all cases, the Y band provides velocity precisions that are comparable to those from the optical band. **The NIR bands provide a significant improvement in velocity precision over the optical for late spectral types (≥ M6V) and whenever the star has substantial rotational velocity (v sin i > 5 - 10 km/s).** By combining the Y, J, and H bands, the theoretically attainable velocity precision is as good as or significantly better than that achieved with the optical band.

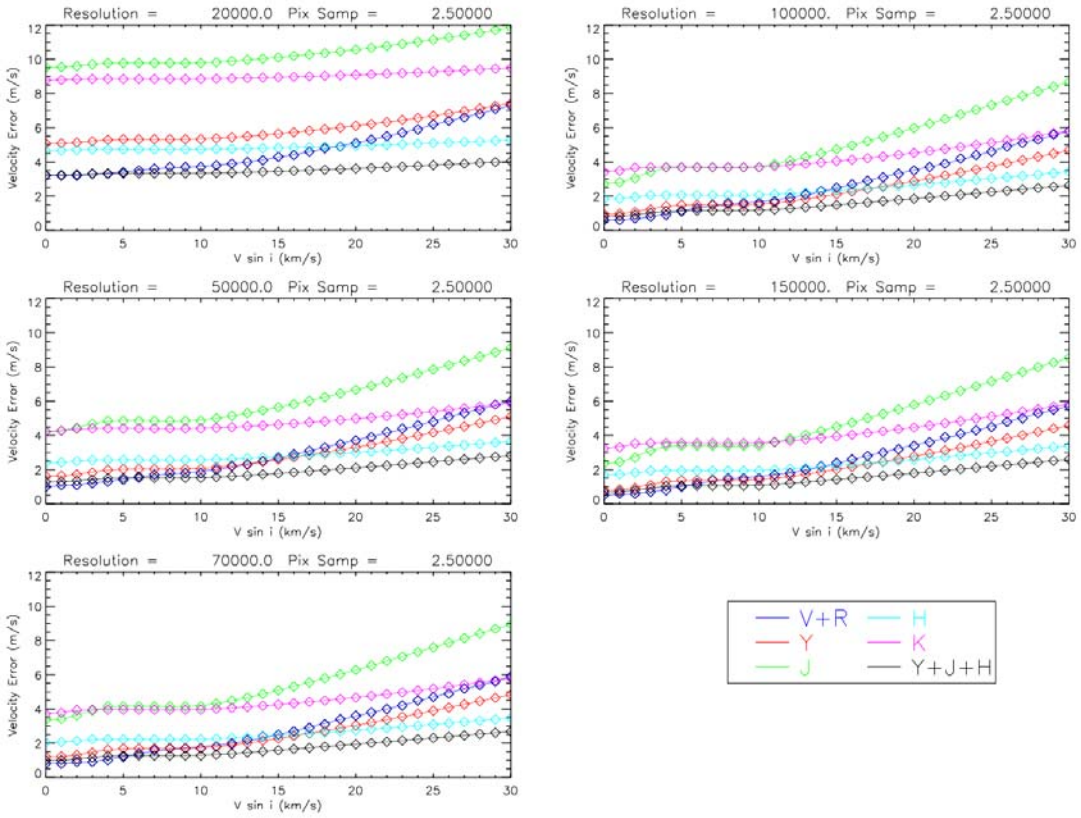

Figure 5-19 Velocity error, εv versus rotational velocity for the M3V model for different values of the resolving power. In each plot the dark blue dots represent the values for the V+R optical regime (HARPS-like), the red for the Y band, the green for the J band, the light blue for the H band, and the black for the combined NIR (Y+J+H) bands. A pixel sampling of 2.5 was assumed. The solid lines are low-order polynomial fits to the points.

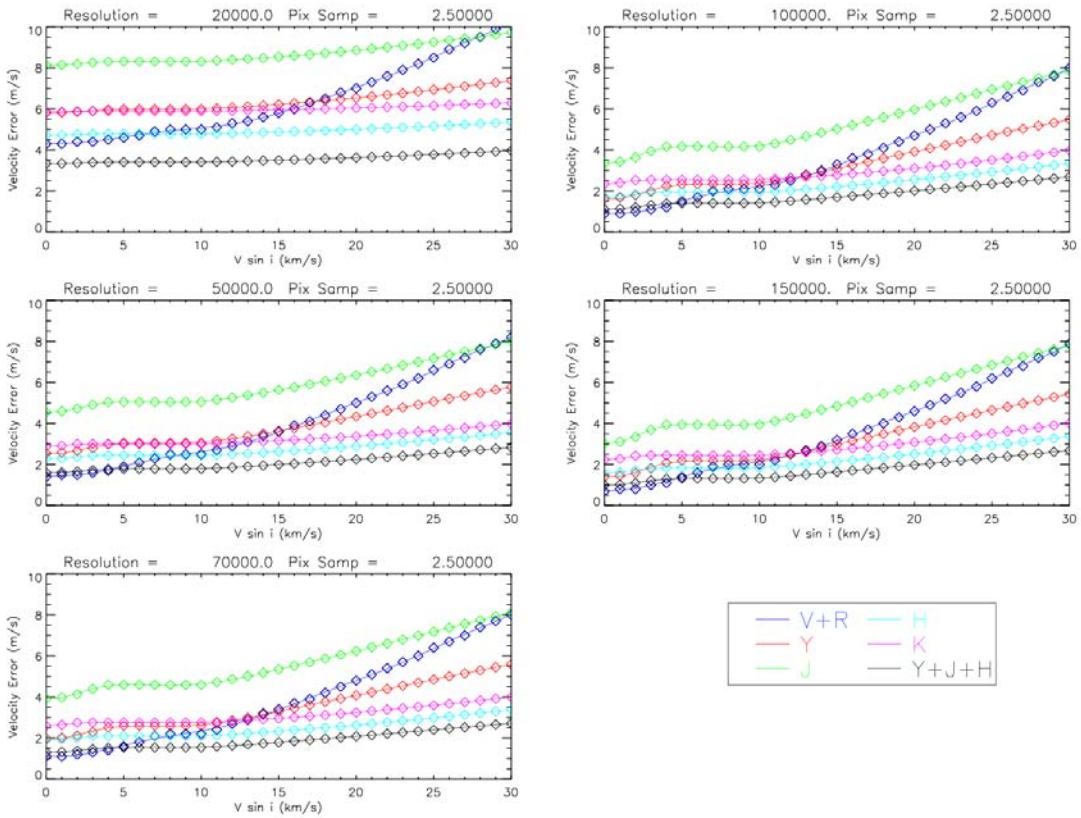

Figure 5-20 Velocity error, εv versus rotational velocity for the M6V model for different values of the resolving power. In each plot the dark blue dots represent the values for the V+R optical regime (HARPS-like), the red for the Y band, the green for the J band, the light blue for the H band, and the black for the combined NIR (Y+J+H) bands. A pixel sampling of 2.5 was assumed. The solid lines are low-order polynomial fits to the points.

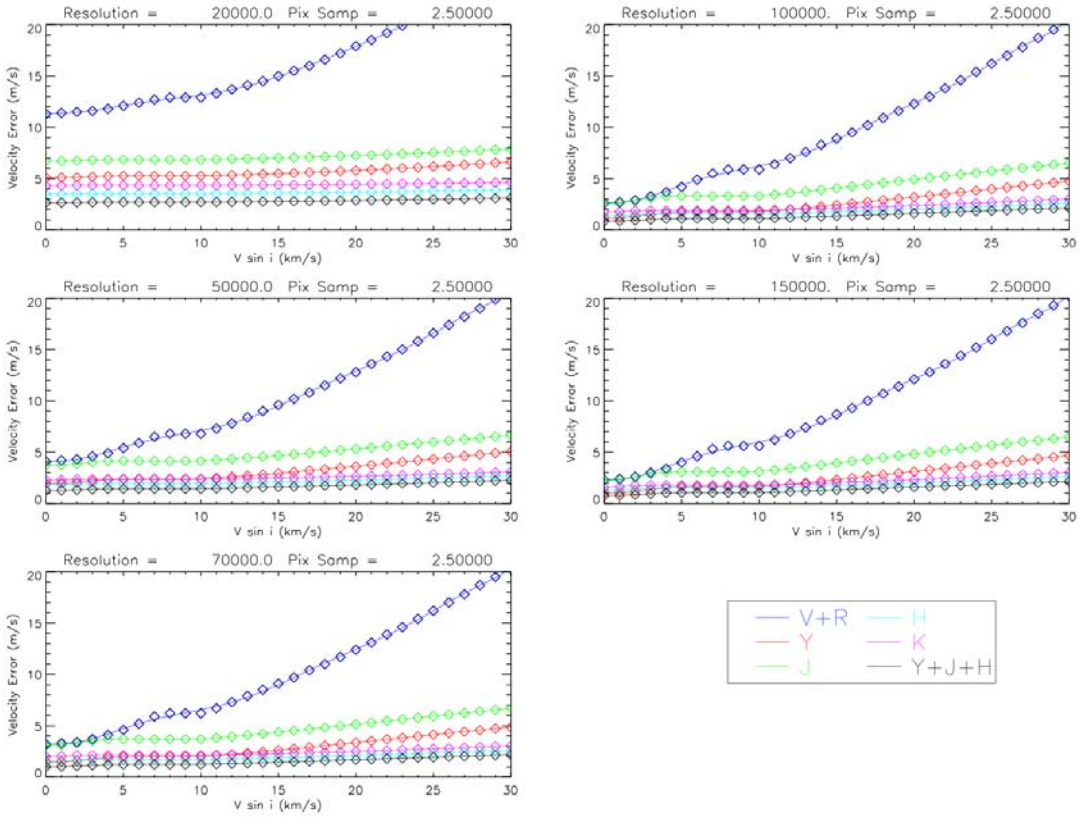

Figure 5-21 Velocity error, εv versus rotational velocity for the M9V model for different values of the resolving power. In each plot the blue dots represent the values for the V+R optical regime (HARPS-like), the red for the Y band, the green for the J band, the light blue for the H band, and the black for the combined NIR (Y+J+H) bands. A pixel sampling of 2.5 was assumed. The solid lines are low-order polynomial fits to the points.

5.2.9 Resolving Power

As has been found by Bouchy et al. (2001), observations at R values higher than 100K provide little improvement in the attainable velocity precision. Based on our results, the optimal R value would appear to be between 70K and 100K.

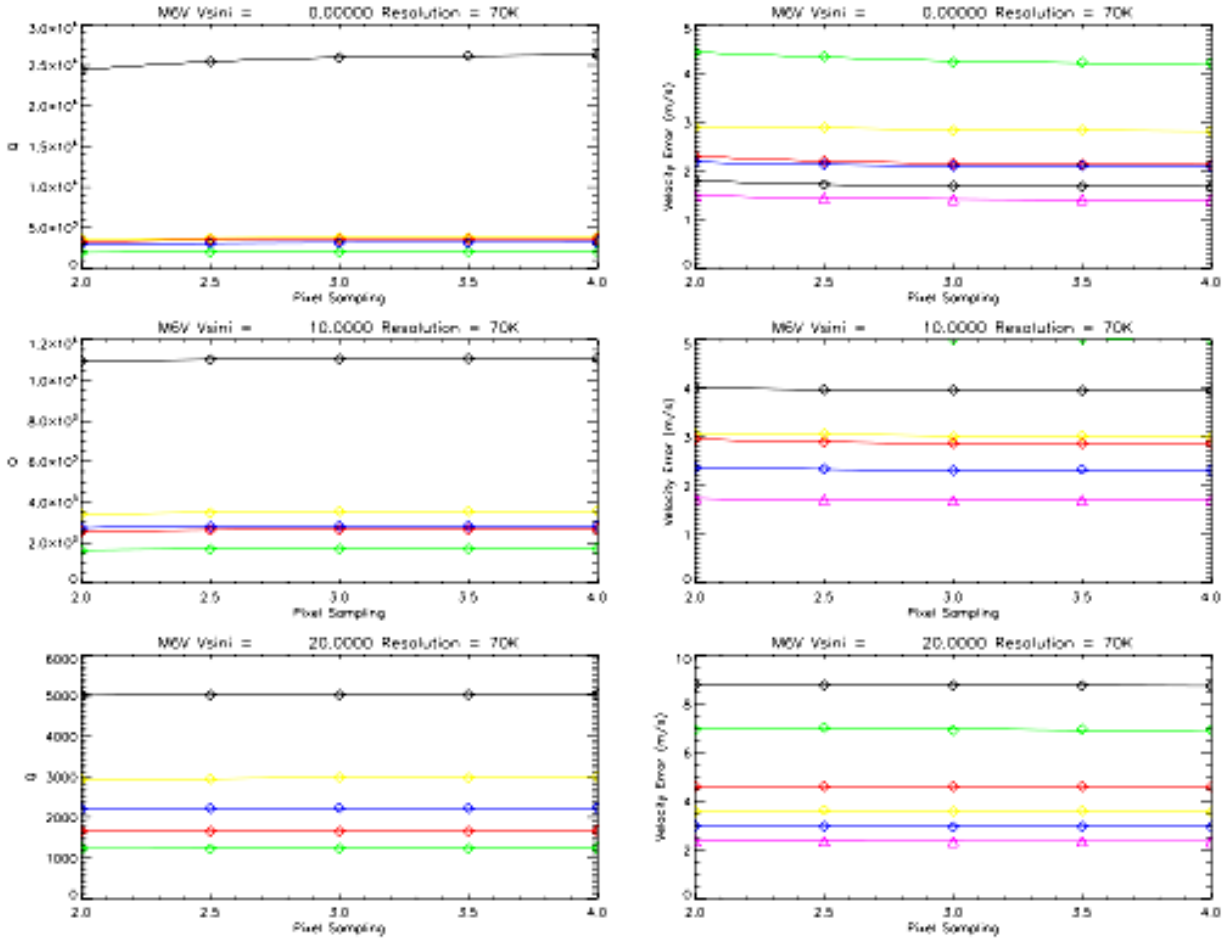

Figure 5-22 Q (left) and ε_v (right) versus pixel sampling for the M6V model and three values of the rotational velocity. A resolving power of R=70000 was assumed. The solid lines are low-order polynomial fits to the points.

5.3 SAMPLING

Figure 5-22 presents the Q and εv values as a function of pixel sampling for the M6V model with a resolving power of 70000 and three values of rotational velocity (0, 10, and 20 km/s). There appears to be little variation in either quantity with p, although a slight minimum can be found near p ~ 3 pixels.

5.4 DISCUSSION AND CONCLUSIONS

Although the NIR bands are contaminated by atmospheric absorption, they remain extremely useful for radial velocity measurements of late-type stars. As can be seen from the figures presented here, the Quality Factor Q, although a good measure of the inherent Doppler information contained in a spectrum, is not a good measure of the theoretically attainable velocity precision from an observation. This is simply because it does not take into account the number of available photons. For M stars, factors of 5-100 more photons are emitted in the NIR bands compared to the optical. This more than makes up for the reduced Doppler content. The

NIR bands, particularly Y and H, are especially useful if the star has substantial rotational velocity. The NIR bands allow velocity measurements with an accuracy of a few meters per second to be attained for all M subtypes. Precisions on the order of 1 - 2 m/s can be achieved by combining the Y and H-band measurements. We consider this to be a conservative conclusion since we expect that overall the synthetic spectra in the infrared probably underestimate the number and strength of M dwarf features, e.g. Figure 5-12. In addition, the synthetic spectra will serve to overemphasize the quality factor of the optical regime because they do not adequately include the observed blanketing effects of photospheric dust at optical wavelengths.

5.4.1 Radial velocity analysis of simulated M dwarfs

Two spectra were generated for a M3V and a M6V dwarf, respectively, sampled over a 0.98-1.1 micron range at 70k resolution. The spectra have a S/N=300 and are contaminated by telluric lines. The telluric lines have a random jitter over a 0-100 m/s range. Also, the stellar lines are rotationally broadened to 5 km/s in both spectra. Both data sets consist of 11 spectra and a telluric line - free template.

The spectra have been normalised by the corresponding, approximately determined continuum trends and then had the simulated Doppler shifts measured using the CCF method. To do this, the cleanest 16k-segments of the spectra were chosen and cross-correlated with templates in the frequency domain, using the FFTW3 package Fourier Transform routines. CCF shifts were measured by fitting an orthogonalized, 5-point parabola around the CCF peak. Orthogonalization of model polynomials minimises a correlation between coefficients, whereas limiting the fit to the very top of the CCF makes the procedure reasonably independent of any lower level asymmetries in it. Typically, the S/N ratio for these fits (peak/RMS) was much larger than a 1000, resulting in errors of shift determination on the order of (1/1000)*pixel width.

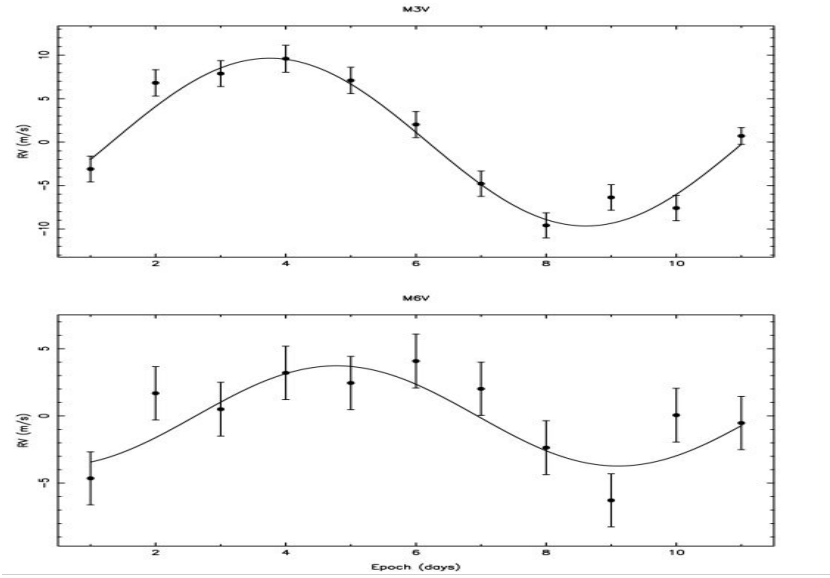

Figure 5-23 Simulated radial velocity curves for spectral types M3 and M6.

To determine the simulated orbits, the spectra have been sampled at a fixed 1-day interval and fitted circular orbits to the measured RVs using Wolszczan's radial velocity code. The results are

shown in the enclosed figure and in the table, which lists the best-fit parameters for the two data sets. Errors in orbital parameters have been determined by means of the standard bootstrap method.

M3V	M6V
a1sini = 0.0013 +/- 0.0001 10^6 km	a1sini = 0.0004 +/- 0.0001 10^6 km
Pb = 9.718 +/- 0.251 days	Pb = 8.652 +/- 2.123 days
T0 = 3.7519 +/- 0.1000 MJD	T0 = 4.7795 +/- 0.8142 MJD
e = 0.00000 +/- 0.0000	e = 0.00000 +/- 0.0000
omega = 0.000 +/- 0.000 deg	omega = 0.000 +/- 0.000 deg
K1 = 9.651 +/- 0.764 m/s	K1 = 3.726 +/- 1.413 m/s
rms = 1.808 m/s	rms = 3.374 m/s
chisq = 2.408	chisq = 2.240
m1 = 0.33 Msun	m1 = 0.15 Msun
a2 = 0.062 A.U.	a2 = 0.044 A.U.
m2sini = 0.000046 Msun	m2 sini = 0.000010 Msun

It is apparent from the figure and the table that the CCF analysis of the simulated spectra has recovered the simulated orbits represented by a 10 m/s and 5 m/s RV variation for the M3V and the M6V dwarf, respectively. Also, note that only one orbital cycle is present in both data sets and that no attempt has been made to compensate for the presence of telluric lines in the spectra. In particular, a marginal detection of the M6V star orbit would most certainly become quite secure, if more orbits were included in the analysis. This simulation is designed to illustrate a worst case situation: no telluric correction, maximum jet stream winds, only a small fraction of the available spectral range was used (only Y band), and a small number of data points.

5.4.2 Stellar Activity

For most main sequence stars it is well established (e.g. Hatzes et al. 2002) that rotation is closely correlated to stellar activity. Thus in addition to high v sin i values blurring radial velocity information they are also synonymous with the support magnetic spots which have different temperatures and velocities to bulk rotational velocities (e.g. differential rotation of ε Eri measured by MOST by Croll et al. 2006). Such spots explain the high radial velocity jitter values recorded for active stars. Nonetheless activity proxies have only recently been determined for many local bright stars. Thus included within the stars currently under scrutiny are many that are significantly active. Indeed exoplanets have already been found around a number of active stars. Some radial velocity signals interpreted as exoplanets have been shown to arise from the rotational modulation of stellar surface activity e.g., HD192263 (Henry, Donahue & Balinuas 2002). Taken alongside their relatively high rotation rates, the long evolutionary timescales associated with M dwarfs suggest that their phase of relatively high activity is prolonged relative to Solar type stars. Activity for Solar type stars is usually discerned using so-called S values as pioneered and continued by the Mount Wilson Observatory (e.g. Duncan et al. 2005). These are a measure of the Ca HK line emission and are characterised by both persistent and flare emission for which the heating mechanism is not understood. Ca HK measurements are now routinely

compared to observed 'jitter' for radial velocity searches (Wright et al. 2005). This has produced a useful predictor to understand what part of any radial velocity signal may be ascribed to the star's activity as opposed to intrinsic noise or an exoplanet radial velocity signature. While low values of jitter are clearly required for detection of low-mass planets the existing exoplanet detections (Figure 5-24) indicate that exoplanet are detected in the presence of significant jitter.

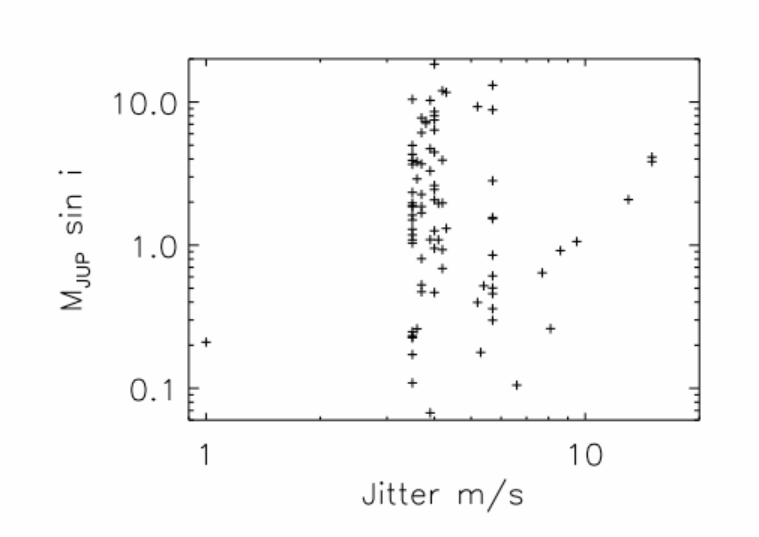

Figure 5-24 Jitter values for exoplanet host stars compared to exoplanet masses based on Butler et al. (2006) catalogue.

The largest compilation of stellar jitter has been made by Wright (2005) based on the long running Keck and Lick radial velocity surveys. Although the M dwarf sample considered is not as well characterised as the hotter stars, Figure 5-25 indicates that M dwarf jitter values are rather similar to those of K, G and F type stars (in spite of the fact that the selection procedure to include inactive star was less rigorous for these M stars). It should be mentioned again that the lowest mass radial velocity planets discovered to date have been made around the M dwarfs GJ436 and GJ876 which are part of this sample.

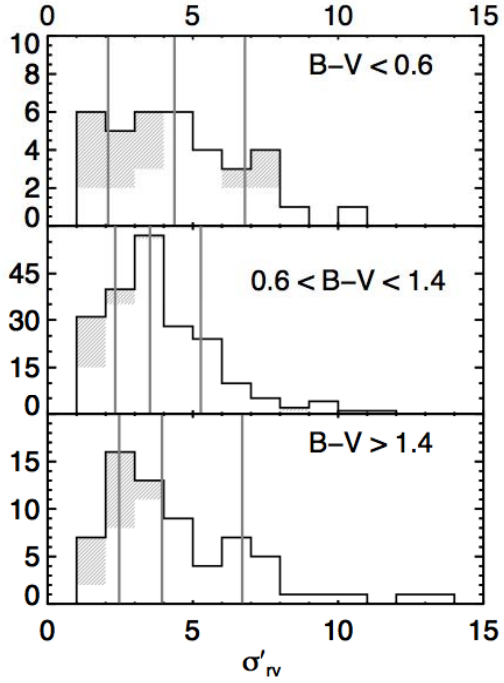

Figure 5-25 shows the distribution of jitter values for stars in three B-V ranges (corresponding roughly to inactive and unevolved spectral types F, G and K, and M) from Wright (2005). The vertical bars show the values of the 20th percentile, median, and 80th percentile. Shaded regions indicate stars for which only upper limits on the jitter can be set. It should be noted that the template error and photon-limited precision is 2 m/s, 2-4 m/s for objects in the middle and upper plots and 3 m/s, 3-8m/s for the lower plot.

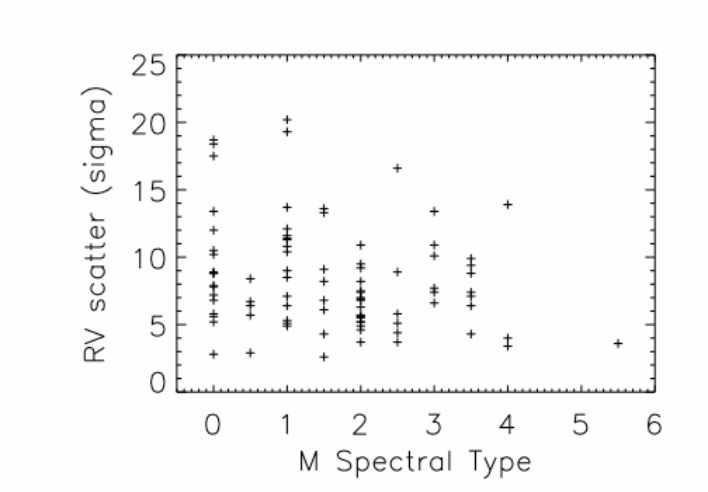

Figure 5-26 shows the scatter of M dwarf radial velocities as a function of spectral type based on the results of Endl et al. (2006).

The largest radial velocity programme for M dwarfs that has been published to date is Endl et al. (2006). The sample of 90 M dwarfs is compiled from four different radial velocity surveys and is based on an object selection criteria which uses strong coronal X-ray emission based on the

ROSAT All-Sky-Survey to remove the most active M dwarfs. While the work of Endl et al. does not extend to late enough spectral types to be especially useful for PRVS (mostly it is earlier than M3V) it at least serves to indicate that there is no evidence for an increase in RV scatter with spectral type even though the later type M dwarfs tended to be the faintest objects in the survey. This presumably arises because the relative faintness of later M spectral types is compensated by the increasing richness of spectral information due to the widespread formation of molecules and thus a denser packing of strong spectral features from which to derive radial velocities.

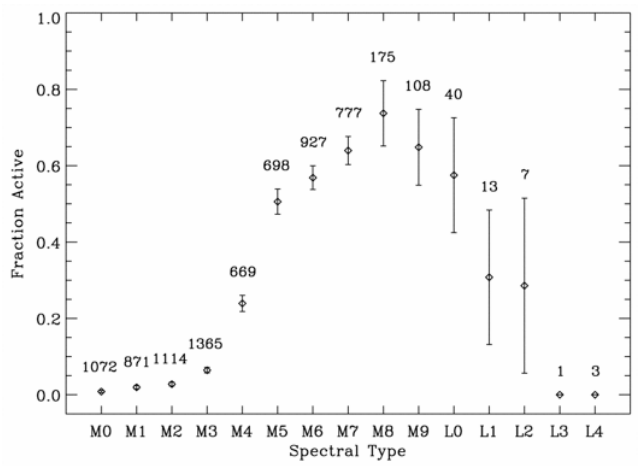

Figure 5-27 Fraction of stars with variable Hα (activity proxy) shown as a function of spectral type based on SDSS results (from West et al. 2004 and confirmed by West et al. 2006). The numbers above each bin represent the total number of stars used to compute the fraction. The presence of inactive M7 and M8 stars had not seen in earlier observations. Spectral type bins with no observed activity (L3, L4) are included for completeness.

Evolutionary models of M dwarfs (e.g. Adams, Bodenheimer & Laughlin 2005) bear out the undergraduate stellar moto of 'live fast die young' and show that evolutionary changes in late type M dwarfs (with masses close to the star-brown dwarf mass break) are very slow and that they live for trillions of year. It was anticipated that such long nuclear timescales might carry over into long activity timescales for M dwarfs. The extrapolation of the simple log-linear fit of the age at which activity ceases versus spectral type (colour, mass) derived from a few open clusters in Hawley et al. (2000) would predict that no M7 dwarfs in the galaxy would be old enough to have ceased their active phase. However, based on observations of ~2600 M7 dwarfs in SDSS, West et al. (2006) suggest a factor of 3 difference in activity between young M7 dwarfs and those with ages of 6-7 Gyr. Based on their high SN observations of inactive M7 stars at a variety of ages they expect that Hα measured activity shuts off rather rapidly rather than undergoing a gradual decline.

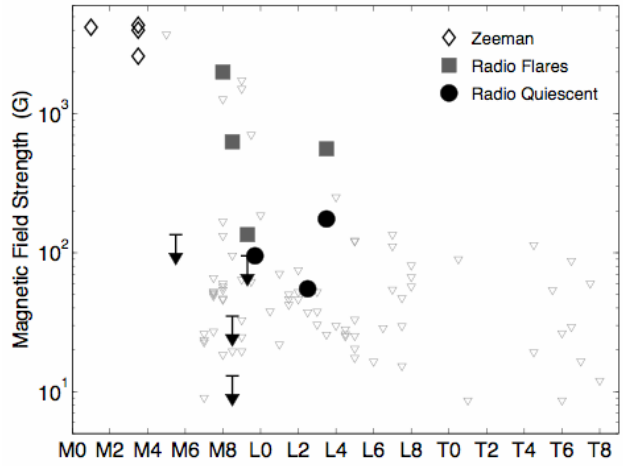

Figure 5-28 (from Berger, 2006) Magnetic field strengths and upper limits as inferred from other radio observations (quiescent: circles; flares: squares). Also shown are the values for early M dwarfs measured from Zeeman line broadening (Saar & Linsky 1985; Johns-Krull & Valenti 1996). We note that the surface field strength in the radio active dwarfs may be up to an order of magnitude larger depending on the structure of the field and the height of the radio emitting region.

For solar type stars CaHK is the most well established activity proxy. However, for M dwarfs this is a weak feature (e.g., even for young Hyads, Paulson et al. 2002) and is located at rather too short wavelengths to be useful for later M dwarfs. In general terms, coronal emission is more prominent (easier to measure) than chromospheric emission. So for M dwarfs activity proxies such as Hα emission, X-ray flux, radio flux and photometric variability must be considered. This situation arises because stars on the main sequence become fully convective below a mass of about 0.35 M , magnetic fields cannot be maintained stars of lower mass or later type via an αΩ dynamo. An alternative dynamo may come into operation (e.g., Chabrier & Kuker 2005). Such a change in dynamo mechanism with spectral types seems to directly affects the activity of M dwarfs as measured by Hα emission. Early M dwarfs, in most cases do not show any detectable Hα emission whereas it increases at mid and late M type. Furthermore, a saturation-type relation between rotation and activity has been confirmed by Mohanty & Basri (2003) and Delfosse et al. (1998). The detection of flares and apparent rotationally modulated radio emission (Berger et al. 2005) indicates the existence of magnetic fields. However, Welsh et al. (2005) finds that on average UV flares recorded by GALEX are five times less energetic for M5-9 stars than for M1-5 stars. Based on Hα measurements, West et al. (2004) find that magnetic activity strongly decreases beyond around M7. These results as well as modelling of late M dwarf spectra may be explained via an increasingly neutral photosphere and the onset of dust formation. For later spectral types it is not clear the extent to which photometric activity is caused by magnetic activity (through star spots) and dust clouds. So while there is a clear trend for later-type objects to rotate much faster this is appears to be offset by the lack of magnetic activity and prevalence of dust clouds.

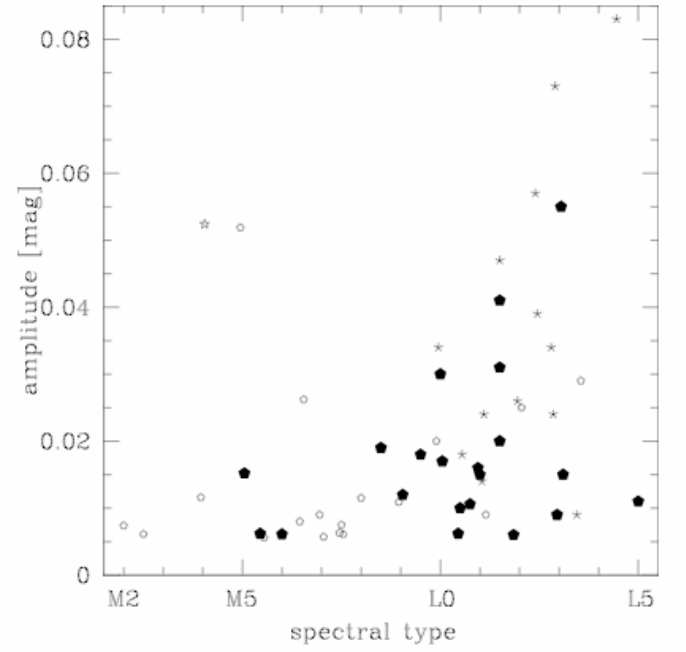

Figure 5-29 Rockenfeller, Bailer-Jones & Mundt (2006) shows variability amplitudes (variable objects, open markers) and upper detection limits (non-variable objects, open markers) compiled from relevant works in the I band. Starred symbols stand for RMS-amplitudes where the χ^2 test gives a detection but variability is finally rejected. Amplitudes and upper limits are RMS values.

Beyond M dwarf spectral types of around M6 dust forms in their atmospheres (e.g., Jones & Tsuji 1997). The impact of dust is now reasonably well modelled and is an essential ingredient for modelling late M dwarfs and the L spectral types. Once the photospheric temperatures of M dwarfs drops to around 1500 K methane forms in their atmosphere (defining T spectral class). Around this temperature the atmosphere fundamentally changes and there is a rain-out of the dust and the photospheres of such objects (which must incidentally be brown dwarfs) become dust-free.

Hatzes et al. (2002) gives the random variations from spots covering a fraction F (%) of the surface as: A(m/s) = (8.6 v sin i - 1.6) . $F^{0.9}$. For a spot coverage (F) of 1% and v sin i =7km/s, this gives A=60m/s i.e., not very promising. In fact F would be higher for the active M stars (perhaps >5%). However, such dramatic radial velocity changes ('jitter') are not seen for M dwarfs: to quote Saar et al. (2004) 'even relatively active stars in this spectral range are good targets for planet searches'. This situation probably arises due to the increasing gravity to later dwarf spectral types. PRVS should have the added advantage of reduced star/spot contrast in the infrared; typically this gives a factor 3-4 lower contrast compared with the optical, which is reflected in the lower apparent variability when observing in the NIR (eg Rockenfeller at al., 2006a).

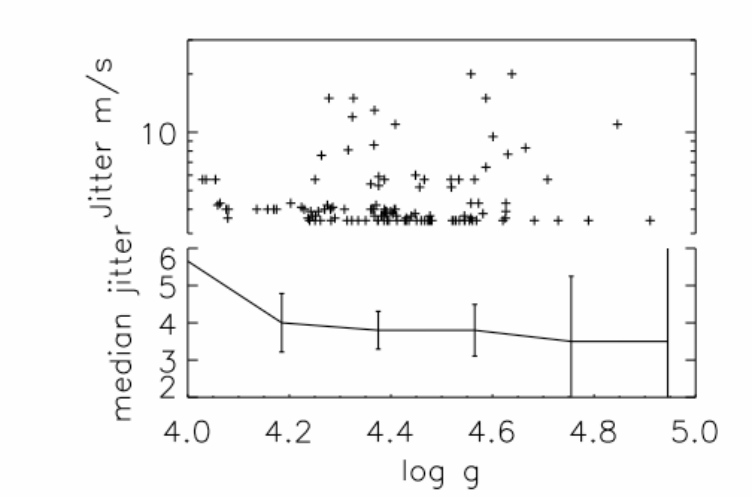

Figure 5-30 Velocity jitter in m/s inferred for exoplanets.org stars with published planets. Log g values below 4 are not shown though based on measured K giant planets (e.g. Setiawan et al. 2004) are larger than 50 m/s. There are relatively few planets with recorded gravities above log g of 4.6 so the data for the two right hand bins has been combined.

Empirical investigations to investigate 'weather' in late-type stars and brown dwarfs have been pioneered by Tinney & Tolley (1999) though it has been a field plagued by marginal detections. Work by Rockenfeller et al. (2006a,b) reasonably claims to have associated photometric variability and v sin i. Rockenfeller et al. investigated the incidence of variability in M dwarfs and L dwarfs. They confirm that the measured amplitude of variable M dwarfs increases strongly from the red (I-band) to U/UV (e.g. Stepanov et al. 1995). Based on I band variability they find fractions of 0.25±0.25 (M0-M4, 4 objects), 0.29±0.13 (M5-M9, 17 objects) and 0.48±0.12 (L type, 31 objects). Overall they find a 2σ difference between M dwarfs and L dwarfs and attribute this to an increased occurrence of variability among L dwarfs. Despite in-depth modelling, Rockenfeller et al. do not manage to determine whether the increase in variability for L dwarfs as due to clear hole in a dusty sky or the other way round, dusty cloud on a clear sky. The incompleteness of further information on the targets such as, Hα, v sin i, X-ray flux mean that it has not been properly tested whether these quantities are significantly different between variable and non-variable objects. Despite considerable ground based work over the last six years no signature have been traced in the infrared, even in Spitzer observations of L dwarfs (Morales-Calderon et al. 2006).

The lack of a predictive model for the velocity fields for the Sun means that there are many pieces missing in the jigsaw to understand the likely activity of late-type M dwarfs as well as L and T dwarfs. While there is plenty of evidence for substantial spots, flares and even dust clouds, the existing photometric variability and radial velocity evidence points to the likelihood for relatively low radial velocity jitter values being recorded for M and L dwarfs. While rotation rates increases toward lower temperatures and masses, any increases in activity may well offset by a lack of photospheric magnetic field and increasing stellar gravity. In solar type stars large velocity shifts arise in part due to the 1700 K difference between solar photosphere and solar spot photosphere. Modelling by Rockenfeller et al. (2006) suggests that the difference in temperature between spots and photosphere to be ~200 K for late-type M dwarfs. Furthermore, PRVS measurements will be made in the infrared where the contrast between photosphere and spot will be much smaller.

5.5 MOCK SURVEY

There are a number of theoretical simulations which touch on simulations of terrestrial planets in a variety of ways including analytical extrapolation (eg., Grether & Lineweaver 2006), scaling laws of (e.g., Ida & Lin 2005), ab inito Monte Carlo methodology (e.g., Alibert et al. 2005ab) as well as considerable exoplanets around M dwarfs as a means to distinguish formation mechanisms e.g. Laughlin et al. (2004) and Kornet, Wolf & Rozyczka (2006). Theoretical works are all optimistic about the formation of large numbers of terrestrial planets. While these are exciting and suggestive, the predictions include a wide variety of orbital outcomes and there remain many poorly constrained inputs to the models. At present, it is not clear that models yet have substantial predictive power. Given that the field of exoplanets has been driven to date by observations we consider a more empirical approach.

If we scale from the exoplanets discovered by the optical radial velocity surveys (Figure 5-8) for a five year survey we see that PRVS may discover around 20 exoplanets with $< 10\ M_{\oplus}$ including a few around an Earth mass. This is consistent with simulations based on Grether & Lineweaver (2006), Ailbert et al. (2005). Though the theoretical expectations are that Earth mass exoplanets should be proportionally more common than around Solar type stars theoretical, predictions in this field are in their infancy and so scaling from existing optical surveys is more conservative. Based on the planets discovered with orbits less than five years the Keck, Lick and AAT planet searches have surveyed 1040 stars and found 124 exoplanets with orbits of less than five years. Scaling by a factor of 0.66 to account for the sky coverage accessible to Gemini means that PRVS will need to survey 686 stars.

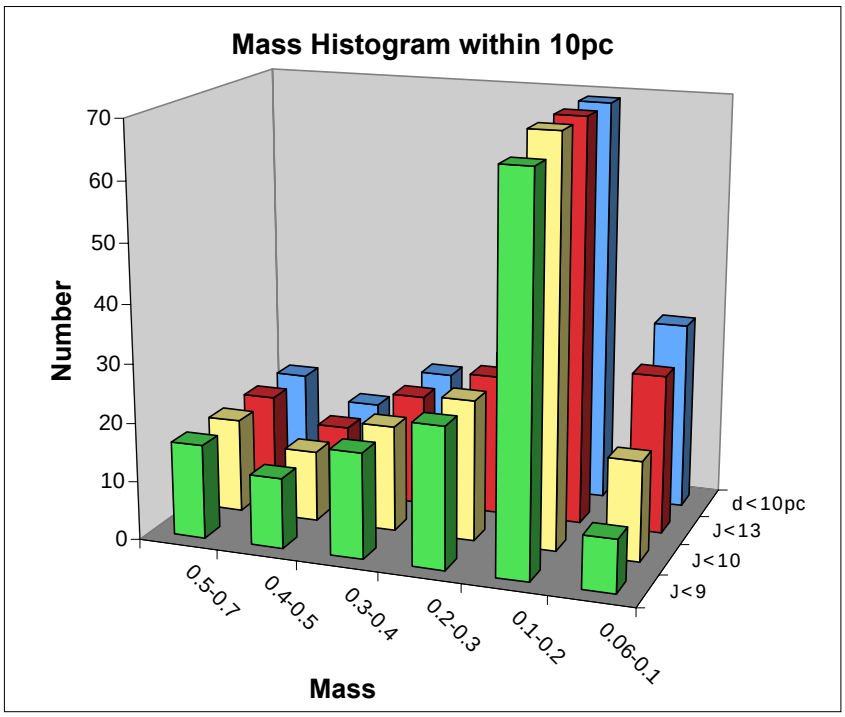

Figure 5-31 Examination of the 10pc sample (based on sample supplied by Todd Henry for this design study) indicates that the bulk of the available objects have masses less than 0.2 $M_{\odot}$ and are thus prime targets (ie. Spectral types cooler than M4 and nearly all beyond the reach of optical surveys). The histograms are shown for different J band magnitudes to indicate that high precisions (e.g., S/N=300 in 1hr for J=11.25) will be achievable for all but the very coolest known brown dwarfs. Even this 10pc sample is expected to be incomplete by perhaps 50%.

Thus it is expected that the 0.06-0.1 $M_\odot$ bin will prove to contain more objects than the 0.1-0.2 $M_\odot$ bin. This will be revealed following the analysis of more reliable multi-band deeper IR surveys including proper motions (UKIDSS and Pann-Starrs).

5.5.1 PRVS Notional RV Survey

We constructed mock surveys in order to gauge the various factors involved in conducting a high-precision RV survey with PRVS. The input population of ultra-cool dwarfs in the solar neighbourhood was based on the *Nstars* project (Reid et al. 2004, Cruz et al. 2004 and for the L and T dwarfs Allen et al. 2006) and the observed IR colours and magnitudes of M and L dwarfs. The J-band Luminosity Function resulting from this work and used in our mock RV surveys is given in Table 3 J-band Luminosity Function based on Reid et al. (2004) and Cruz et al. (2004)..

Table 3 J-band Luminosity Function based on Reid et al. (2004) and Cruz et al. (2004).

M(J)	ϕ	f_{good}	M_*	~ Sp T
5.25	3.4	1.0	0.64	M0
6.25	4.9	1.0	0.55	
6.75	4.7	1.0	0.46	M1
7.25	6.1	1.0	0.37	
7.75	6.3	1.0	0.30	M3
8.25	5.3	1.0	0.24	
8.75	5.4	0.75	0.19	M4
9.25	5.3	0.75	0.15	
9.75	4.3	0.5	0.12	M5
10.25	2.7	0.5	0.10	
10.75	1.79	0.5	0.090	M7
11.25	1.12	0.5	0.081	M8
11.75	0.97	0.1	0.076	L0
12.25	0.60	0.1	0.074	L1
12.75	0.34	0.1	0.073	L3
13.25	0.30	0.1	0.073	L4

M(J) is the J-band magnitude, ϕ is the space density in units 10^{-3} stars/pc^3, $\mathbf{f_{good}}$ is an ad hoc parameter which represents the fraction of stars useable for an RV survey ($v \sin i < 10$ km/s). $\mathbf{M_*}$ is the mass in units of the sun based on a 5 Gyr Baraffe model (which is a good fit to the published dynamical data of Delfosse et al. (2004). **Sp T** is the approximate spectral type.

The survey is optimized to cover as many mid to late M dwarfs (M5 V to M9 V) as reasonable. These lower mass stars require a velocity precision of ≈ 2 m/s to detect terrestrial mass planets in the habitable zone. Surveys of early M stars can cover more stars but require a velocity precision of ≤ ~ 1 m/s .

For viable surveys we consider that we need to survey ~ 500 stars over 30 epochs over about five years to be comparable with optical surveys. The important parameters include instrument sensitivity, the S/N per target observation to reach a desired RV precision, the number of observing nights per year, the fraction of stars of suitable stars, and observing efficiency and

observation overhead for acquisition. Our analysis based on the Bouchy et al. (2001) formulation indicates that a S/N of 300 is required to each a velocity precision of ~ 1 m/s. As an independent check Alex Wolszczan used his RV code to extract radial velocities from simulated PRVS spectra and this method also finds that a S/N of 300 is required for a RV precision ~ 1 m/s. Based on measurements of activity in M stars 30% of the stars in each luminosity bin are rejected. Although our modelling shows that v sin i > 10 km/s is not in itself a significant hindrance to measuring precise radial velocities (see the modelling presented in the Science Case) the mock survey is shown for all remaining stars and for stars with v sin i < 10 km/s to assess the effect on the surveys where velocity jitter in fast rotators is a factor. This effect is quantified in the $\mathbf{f_{good}}$ parameter in the J-band Luminosity Function (in the above table) and comes from v sin i measurements of M and L stars. Mock surveys are computed for 50 and 100 nights per year for five years.

Table 4: Mock M Dwarf RV Surveys

S/N:	**300**			
Nights/year :	**100**		**50**	
***V* sin *i* / km/s:**	**All**	**<10**	**all**	**< 10**
~ Sp. Type	**Number of Stars**			
M2.5 V	77	90	35	41
M3.0 V	77	90	35	41
M4.0 V	77	90	35	41
M5.0 V	77	90	35	41
M6.0 V	77	58	35	41
M6.5 V	35	17	35	17
M8.0 V	10	5	10	5
M9.0 V	3	1	3	1
L1.0	1	0	1	0
L2.0	0	0	0	0
Total	434	441	198	253

The table above shows the results of several simulations of the M Dwarf RV Survey. These simulations indicate that 50 nights per year is marginal (only about 200 stars) for a good survey and that 100 nights per year is better (over 400 stars). These results are preliminary and much more work needs to be done to design an optimised survey.

As an example, the output of the simulation for 100 nights/year, S/N=300, v sin i < 10 km/s (red in the above table), is given below:

---

(1) Magnitude-limited sample:
fraction of sky observable = 0.66
fraction of non-active stars = 0.7
accounting for fraction of good stars in each LF bin: YES

minimum S/N = 300
max integration per object = 4800.0 sec
limiting mags {Y,J,H} = 12.30, 11.75, 11.20

N*(max) = # of stars observable to specified sensitivity limit
d(max) = maximum distance (pc) the spectral type can be observed

---

~SpT	fgood	M(Y)	d(max)	N*(max)	M(J)	d(max)	N*(max)	M(H)	d(max)	N*(max)
2.5	1.00	8.2	68.9	3986	7.8	68.0	3832	7.2	67.7	3776
3.0	1.00	8.8	53.7	1590	8.2	54.0	1616	7.7	53.3	1552
4.0	0.75	9.3	41.1	545	8.8	42.9	619	8.2	42.0	580
5.0	0.75	9.9	31.5	240	9.2	34.1	304	8.7	33.4	287
6.0	0.50	10.5	24.1	58	9.8	27.1	83	9.2	26.8	81
6.5	0.50	11.0	18.8	17	10.2	21.5	26	9.6	21.5	26
8.0	0.50	11.7	14.1	5	10.8	17.1	9	10.1	17.7	10
9.0	0.50	12.2	10.8	1	11.2	13.6	3	10.5	14.5	3
10.0	0.10	12.8	8.3	0	11.8	10.8	0	10.9	11.9	0
11.5	0.10	13.4	6.2	0	12.2	8.6	0	11.3	9.9	0

---

(2) Simulated survey
fraction of sky observable = 0.66
fraction of non-active stars = 0.7
accounting for fraction of good stars in each LF bin: YES

minimum S/N = 300
max integration per object = 4800.0 sec
limiting mags {Y,J,H} = 12.30, 11.75, 11.20

observing efficiency = 80.0%
fixed overhead per star = 180.0 sec
min integation per star = 60.0 sec
# of epochs needed per star = 30
max # of targets per LF bin = 90.0
max # of bright targets per LF bin = 90.0
hours of observing per night = 8.0
survey duration = 5.0 yrs

N* = # of stars observed in sample

<dist = max distance (pc) of targets for each LF bin
Tmax = max integration time of targets for each LF bin
Nts/yr = # of telescope nights per year needed

*** Y-band ***

~SpT	M(Y)	fgood	Mstar	d(max)	N*(max)	N*	<dist	Tmax	Nts/yr
2.5	8.2	1.00	0.30	68.9	3986	90	19.5	30.6	4.8
3.0	8.8	1.00	0.24	53.7	1590	90	20.6	104.3	4.8
4.0	9.3	0.75	0.19	41.1	545	90	22.6	434.9	9.5
5.0	9.9	0.75	0.15	31.5	240	90	22.7	1298.0	21.6
6.0	10.5	0.50	0.12	24.1	58	58	24.1	4800.0	45.7
6.5	11.0	0.50	0.10	18.8	17	17	18.8	4800.0	13.4
8.0	11.7	0.50	0.09	14.1	5	5	14.1	4800.0	3.9
9.0	12.2	0.50	0.08	10.8	1	1	10.8	4800.0	0.8
10.0	12.8	0.10	0.08	8.3	0	0	0.0	0.0	0.0
11.5	13.4	0.10	0.07	6.2	0	0	0.0	0.0	0.0

Total number of targets = 441.0
Telescope nights per year = 104.53

*** J-band ***

~SpT	M(J)	fgood	Mstar	d(max)	N*(max)	N*	<dist	Tmax	Nts/yr
2.5	7.8	1.00	0.30	68.0	3832	90	19.5	32.3	4.8
3.0	8.2	1.00	0.24	54.0	1616	90	20.6	102.1	4.8
4.0	8.8	0.75	0.19	42.9	619	90	22.6	367.0	8.5
5.0	9.2	0.75	0.15	34.1	304	90	22.7	947.1	16.7
6.0	9.8	0.50	0.12	27.1	83	83	27.1	4800.0	65.4
6.5	10.2	0.50	0.10	21.5	26	26	21.5	4800.0	20.5
8.0	10.8	0.50	0.09	17.1	9	9	17.1	4800.0	7.1
9.0	11.2	0.50	0.08	13.6	3	3	13.6	4800.0	2.4
10.0	11.8	0.10	0.08	10.8	0	0	0.0	0.0	0.0
11.5	12.2	0.10	0.07	8.6	0	0	0.0	0.0	0.0

Total number of targets = 481.0
Telescope nights per year = 130.109

*** H-band ***

~SpT	M(H)	fgood	Mstar	d(max)	N*(max)	N*	<dist	Tmax	Nts/yr
2.5	7.2	1.00	0.30	67.7	3776	90	19.5	32.9	4.8
3.0	7.7	1.00	0.24	53.3	1552	90	20.6	107.7	4.9
4.0	8.2	0.75	0.19	42.0	580	90	22.6	400.2	9.0
5.0	8.7	0.75	0.15	33.4	287	90	22.7	1022.6	17.8
6.0	9.2	0.50	0.12	26.8	81	81	26.8	4800.0	63.8
6.5	9.6	0.50	0.10	21.5	26	26	21.5	4800.0	20.5
8.0	10.1	0.50	0.09	17.7	10	10	17.7	4800.0	7.9
9.0	10.5	0.50	0.08	14.5	3	3	14.5	4800.0	2.4
10.0	10.9	0.10	0.08	11.9	0	0	0.0	0.0	0.0
11.5	11.3	0.10	0.07	9.9	0	0	0.0	0.0	0.0

Total number of targets = 480.0
Telescope nights per year = 130.931

5.5.1.1 L and T dwarf RV Survey

As described above there is great scientific potential for an L and T dwarf survey. This is an area where new objects and a better understanding of properties is developing rapidly. Prior to investing a lot of telescope time into such a project, we will embark on pilot project to attempt radial velocity measurements of a few bright examples at different spectral types. It is likely that by the commissioning of PRVS a further spectra type of Y will be available for study.

S/N=100, vsini: all stars

*** J-band ***

~SpT	M(J)	fgood	Mstar	d(max)	N*(max)	N*	<dist	Tmax	Nts/yr
10.0	11.8	1.00	0.08	33.3	70	70	33.3	5600.0	63.9
11.5	12.2	1.00	0.07	26.5	22	22	26.5	5600.0	20.1
12.5	12.8	1.00	0.07	21.0	7	7	21.0	5600.0	6.4
14.0	13.2	1.00	0.07	16.7	3	3	16.7	5600.0	2.7
15.5	13.8	1.00	0.07	13.3	5	5	13.3	5600.0	4.6
17.0	14.2	1.00	0.07	10.5	4	4	10.5	5600.0	3.7
23.0	14.8	1.00	0.06	8.4	3	3	8.4	5600.0	2.7
26.0	15.2	1.00	0.04	6.7	1	1	6.7	5600.0	0.9

Total number of targets = 115.0
Telescope nights per year = 104.938

S/N=100, vsini < 10km/s

*** J-band ***

~SpT	M(J)	fgood	Mstar	d(max)	N*(max)	N*	<dist	Tmax	Nts/yr
10.0	11.8	0.10	0.08	37.8	10	10	37.8	7200.0	11.6

11.5 12.2 0.10 0.07 30.0 3 3 30.0 7200.0 3.5
12.5 12.8 0.10 0.07 23.9 1 1 23.9 7200.0 1.2
14.0 13.2 0.10 0.07 19.0 0 0 0.0 0.0 0.0
15.5 13.8 0.10 0.07 15.1 1 1 15.1 7200.0 1.2
17.0 14.2 0.10 0.07 12.0 1 1 12.0 7200.0 1.2
23.0 14.8 0.10 0.06 9.5 0 0 0.0 0.0 0.0
26.0 15.2 0.10 0.04 7.5 0 0 0.0 0.0 0.0
Total number of targets = 16.0
Telescope nights per year = 18.6

S/N=50, vsini: all stars

*** J-band ***

~SpT M(J) fgood Mstar d(max) N*(max) N* <dist Tmax Nts/yr
10.0 11.8 1.00 0.08 53.5 287 100 37.6 882.7 17.5
11.5 12.2 1.00 0.07 42.5 89 89 42.5 3600.0 53.4
12.5 12.8 1.00 0.07 33.7 28 28 33.7 3600.0 16.8
14.0 13.2 1.00 0.07 26.8 11 11 26.8 3600.0 6.6
15.5 13.8 1.00 0.07 21.3 19 19 21.3 3600.0 11.4
17.0 14.2 1.00 0.07 16.9 16 16 16.9 3600.0 9.6
23.0 14.8 1.00 0.06 13.4 11 11 13.4 3600.0 6.6
26.0 15.2 1.00 0.04 10.7 4 4 10.7 3600.0 2.4
Total number of targets = 278.0
Telescope nights per year = 124.342

S/N=50, vsin < 10km/s

*** J-band ***

~SpT M(J) fgood Mstar d(max) N*(max) N* <dist Tmax Nts/yr
10.0 11.8 0.10 0.08 69.6 63 63 69.6 6100.0 62.4
11.5 12.2 0.10 0.07 55.3 20 20 55.3 6100.0 19.8
12.5 12.8 0.10 0.07 43.9 6 6 43.9 6100.0 5.9
14.0 13.2 0.10 0.07 34.9 2 2 34.9 6100.0 2.0
15.5 13.8 0.10 0.07 27.7 4 4 27.7 6100.0 4.0
17.0 14.2 0.10 0.07 22.0 4 4 22.0 6100.0 4.0
23.0 14.8 0.10 0.06 17.5 2 2 17.5 6100.0 2.0
26.0 15.2 0.10 0.04 13.9 1 1 13.9 6100.0 1.0
Total number of targets = 102.0
Telescope nights per year = 101.044

5.5.2 Summary

The mock survey described here is meant to be representative, not definitive. Our quantitative evaluation reveals several key results:

- As expected for a survey spanning a factor of ~100 in absolute infrared magnitude, it is easy to observe many of early-/mid-M types at little cost in telescope time. The required amount of observing time for these bright targets is driven by the fixed overhead, not by the integration time, and hence there is a strong premium on minimising the observing overheads (e.g. target acquisition).
- Observing the coolest objects is very costly in observing time, not only because these objects are getting fainter but also because the LF is turning down, i.e. there is a lower space density of these ultra-cool objects.
- Observing at Y, J and H-band is sufficient. [Observing at K does not add much; although the coolest dwarfs are quite red, they also are relatively rare and faint, so only a handful of additional objects can be observed at K.]
- Substantial surveys of L and T dwarfs are feasible if a lower radial velocity precision is tolerated.

The survey is optimized to cover as many mid to late M dwarfs (M5 V to M9 V) as reasonable. These lower mass stars require a velocity precision of ≈ 2 m/s to detect terrestrial mass planets in the habitable zone. Surveys of early M stars can cover more stars but require a velocity precision of ≤ ~ 1 m/s .

PRVS can carry out a ground-breaking RV survey and move the field of exoplanets forward substantially by detecting a substantial number of terrestrial mass planets around the closest stars. Of course, interesting science will result before the survey is completed, since the close-in planets will be found relatively quickly, or if such planets are uncommon strong upper limits can be established quickly.

5.5.3 PRVS in the North or South?

In the simulations presented above we have assumed that PRVS will be located at Gemini North. We made this choice based on two criteria. (1) The height of the site means that telluric contamination is significantly less at Gemini North improving all RV measurements (see Table 2). (2) We already know significantly more about the properties of Northern M dwarfs than Southern M dwarfs. The only scientific reason to site PRVS in the South would be the Solar System's 20 pc or so elevation above the galactic plane. This means that there will be a slight over-abundance of targets in the South dependant of the exact scale height of the population (for M dwarfs approximately 300pc). However, if one looks at the known M, L and T dwarfs within 10pc, there are somewhat more systems known in the North (95 out of 174). With the focus of UKIDSS, PannStars and Pathfinder on the discovery and characterisation of nearby dwarfs we expect this gap to widen. As well as providing new objects UKIDSS and PannStars will provide considerably more reliable multi-band photometry and astrometry than would otherwise be available for targets in either hemisphere. This will enable the activity and multiplicity to be constrained a level appropriate for PRVS. Pathfinder (to be sited at HET) is well placed to give us first epoch RV points and $v \sin i$ values for a Northern sample.

5.6 PRVS PATHFINDER

The achievement of m/s radial velocity precisions using common-user telescopes is one of the major technological breakthroughs of recent years. This achievement should not be taken lightly. This was only possible following a development programme lasting many years. Precision radial velocity techniques have been developed and improved using locally available equipment where new techniques and equipment maybe tested and integrated. The path from solar observation by Becker (1976), Koch & Woehl (1984) to pioneering stellar observations using HF gas cells (Campbell & Walker 1979, 1988) to today's achievement of sub m/s RMS velocities with Keck+HIRES, ESO3.6m+HARPS, HET+HRS, VLT-UVES AAT-UCLES is one that leads through several spectrographs, detectors and revisions of calibration methodology. Moving into a wavelength regime where there is no tradition of radial velocities means there is relatively little legacy work and that the PRVS project is exceedingly challenging. It is perhaps unrealistic that in this design study we can foresee and fully specify all the real world pitfalls and interactions that we will need to overcome in over to achieve 1 m/s radial velocities in the infrared. Thus from the outset we have felt it essential to devote significant resources and energies toward a pathfinder project. Our goal is produce an instrument that demonstrates our ability to measure precision radial velocities in the infrared and at the same time focuses our attention on the key technical and software issues to be overcome. In the first phase this is a laboratory based experiment to measure earth rotation by intensive measurements of the Sun. In the second phase the instrument will be moved to HET and measures precision radial velocities of stars with known large amplitude exoplanets. In the third phase PRVS pathfinder will carry out a radial velocity survey of M dwarfs at the HET.

To date only visible echelle spectroscopy using either I_2 or emission line references have yielded precisions on the order of a few m/s. No instruments have published results measuring 'precision' radial velocities in the Near Infrared. However, exciting science results are already being obtained in the infrared with existing facilities at much lower precisions. For example, Stassun et al. (2006) determine the orbits of a binary brown dwarf pair using PHOENIX/Gemini. Using 6 nights of NIRSPEC/Keck time, Martin et al. (2006) have surpassed the precision achieved by previous optical radial velocity work (based on substantial UVES/VLT time). These infrared radial velocity measurements of the nearby brown dwarf LP944-20 report an RMS precision of 360 m/s. Charbonneau and collaborators have a PHOENIX/Gemini programme for which we understand approximately 100m/s precisions are being achieved using telluric features (e.g., Doppmann, White & Charbonneau 2005). In time it should be possible to increase the sensitivity of such tellurically calibrated programmes down to mean atmospheric velocities of 10-25 m/s that are now been achieved in the optical, e.g., Johnston (2006) and Gray & Brown (2006). However, to realise our goal of detecting terrestrial mass planets and to be fully competitive with optical programmes a more precise calibration is required. Below we describe our PRVS Pathfinder instrument that uses emission line calibration (the merits of infrared gas cells are discussed in the appendix). In the 9 months since project's inception, we have already gained RMS precisions of better than 10 m/s on the Sun in the Y band giving us confidence that the stated goals of PRVS maybe achieved.

5.6.1 RVS Pathfinder description

5.6.1.1 Pathfinder goals

The PRVS pathfinder is a brass board instrument meant to explore issues associated with achieving meter/sec (m/s) precision in the Y, J and H bands. The major goals are:

- Demonstrate ability to do Precision Radial Velocities (PRV) in Y, J & H
- Explore sensitivity to telluric contamination
- Test calibration techniques
- Understand modal noise effects in NIR

Once we have confidence that we can achieve PRV over a reasonable time scales we hope to move the pathfinder to the Hobby-Eberly telescope to validate our approach by recovering a known planet system.

5.6.1.2 Spectrograph

The PRVS pathfinder is a brass board instrument meant to explore issues associated with achieving m/s precision in the Y, J and H bands. It is built up mainly of existing in-house components retired or borrowed from other projects.

5.6.1.3 Optical Design

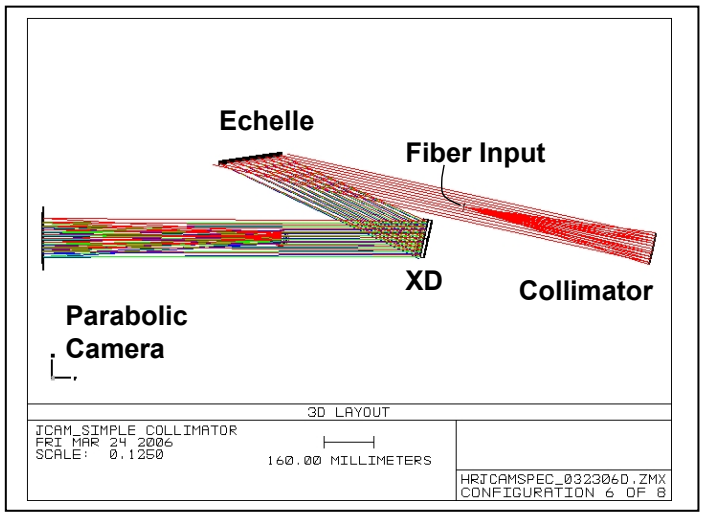

Figure 5-33 Zemax spectrograph layout

In our discussion we use the notation of Schroeder (2000). We use a straightforward in-plane design with a R2 echelle and a 100 mm collimated beam diameter. The Echelle is used at an unusually large θ angle of 12 degrees in order achieve the desired resolving power of $\lambda/\Delta\lambda$ ~50,000. Figure 5-33 shows the Zemax optical layout of the system we have implemented. We will discuss the fibre feed more fully below but the fibre forms a pseudo slit. The collimator is a simple 609 mm parabola. The collimated beam is dispersed by a gold coated 31 line/mm Θ_{blaze} = 63.4 (R2) echelle on a 110 x 210 mm Zerodur substrate. With θ =12° the incident angle, $\alpha = \Theta_{blaze} + \theta$, is 75.4 degrees leading to a substantial vignetting of the collimated beam with the 200 x 100 mm grating blank size we have. At the grating the effective collimated beam is 100 mm high and about 50 mm wide. The diffracted beam is cross dispersed by a 150 l/mm Θ_{blaze} = 2.15 degree grating we happened to have on hand. The efficiency of this in-house but

non-optimum cross disperser (XD) is low in the region 0.95 to 1.35 microns that we are studying on at this time. The efficiency is relative to the blaze peak is about 22%.

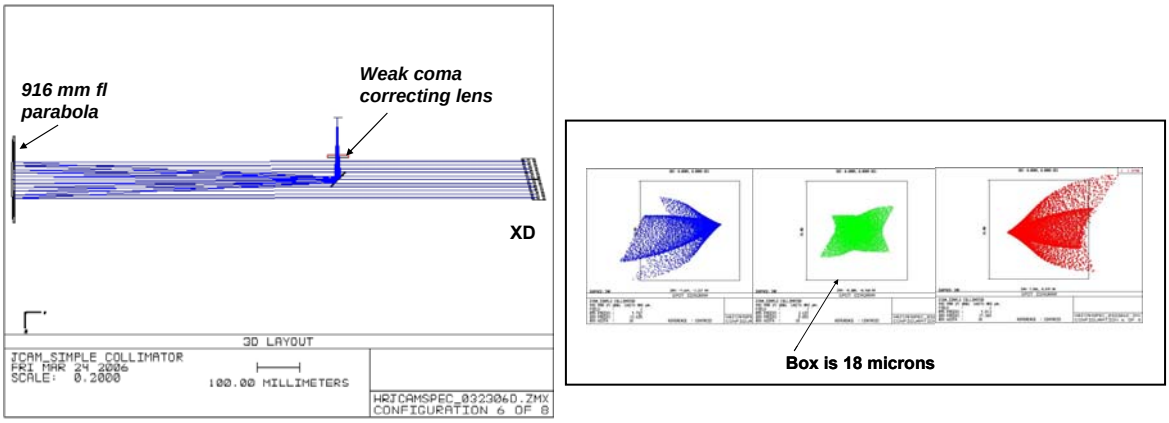

Figure 5-34 Camera layout (left) and Zemax spot diagram (right).

The Camera in this instrument is, like the collimator, a simple parabola. In this case it is a 154 mm diameter 916 mm focal length mirror. We use a weak lens near the focus to correct much of the coma which gives the camera an effective 800 mm focal length. The camera beam is folded so as to allow the dewar to be mounted vertical. This allows the LN_2 to always cover the cold plate on which the detector is mounted. Figure 5-34 shows the camera layout and spot diagram over the field of view (FOV) of the detector in the focal plane. It is clear that the coma is controlled to about 1 pixel at the edges of the detector. As we only have about 2.3 pixels per resolution element, this is important. Indeed we would like to do substantially better in the long run but this was judged sufficient for our initial tests.

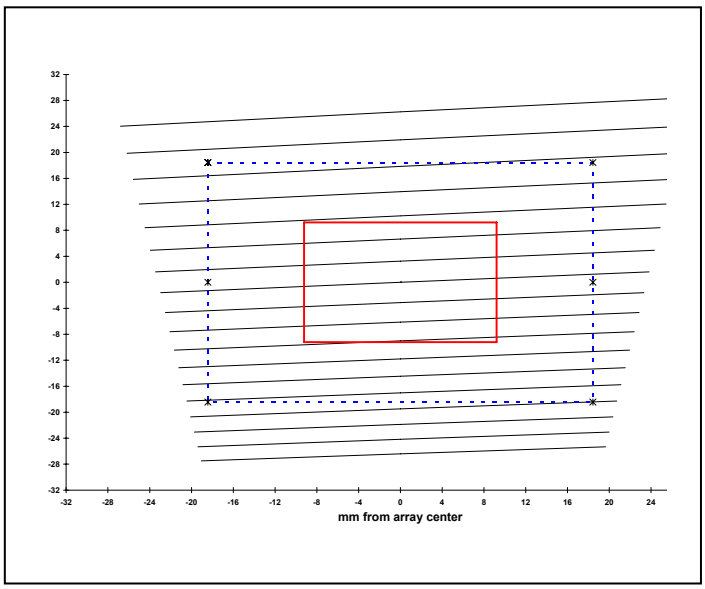

Figure 5-35 Array format

5.6.1.4 Format on the array

With the Hawaii 1k detector discussed below, our focal plane is only 18.4 mm square. The system is designed to yield $\lambda/\Delta\lambda$ ~52500 with 2.36 pixels per resolution element. At 1.0 mm we cover about 44% of the Free Spectral Range (FSR) in an echelle order; this decreases to 33% at 1.3 mm. Figure 5 shows the format of the detector (red line) with one FSR for each echelle order for the PRVS pathfinder configuration. Order 48, which has a blaze peak at 1.15 μm, is roughly centered on the array in this figure. At the short end of the 0.98 to 1.35 micron region we can get 8 orders lie on the array but only about 5 are visible at the long end of the J band.

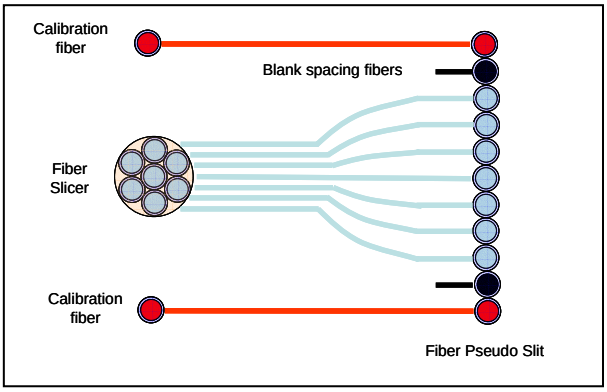

Figure 5-36 Fibre Input concept

5.6.1.5 Fibre Input

The fibre feed is given in Figure 5-36. We use a fibre slicer for the object input. The stacked 7 slicer fibres comprise up the pseudo slit are flanked by fibres that are fed by the calibration lamps. Our current slicer uses 100 micron core, 125 micron cladding diameter fibres and thus has a 49% geometrical throughput. Figure 5-37 (left) shows the polished input end and (middle) shows the pseudo slit which has two calibration fibres, one above and one below the 7 slicer fibres each separated by a blank fibre Figure 5-37 (right) shows the slicer/calibration fibre assembly with laser light illuminating the slicer input. The laser output indicated quite decent FRD although we have yet to quantify this precisely.

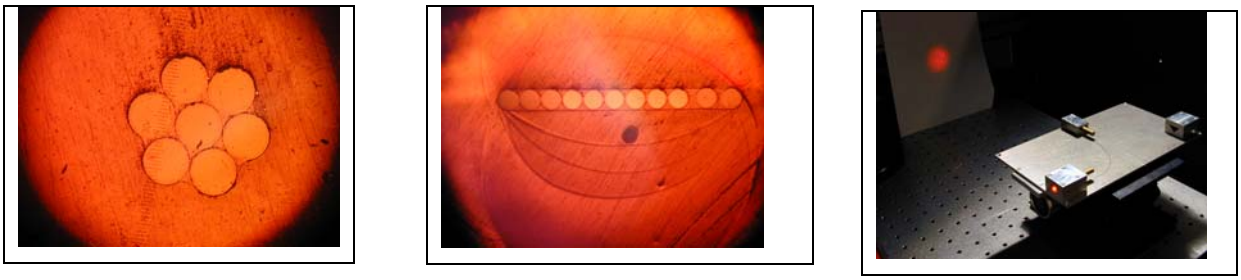

Figure 5-37 The photographs show fibre slicer input (left), fibre slicer pseudo slit with calibration fibres (middle) and slicer pseudo slit (right).

5.6.2 Mechanical Implementation

The entire spectrograph is constructed using mostly standard optical mounting hardware on a small 8 x 2 ft. optical table. The fibre slicer and the detector on mounted on custom made units. This table sits in a lab that has infrequent access and is temperature controlled within a 2 degree band on most days. Figure 5-38 shows the spectrograph in the lab with some of the baffling installed but before thermal insulation was installed.

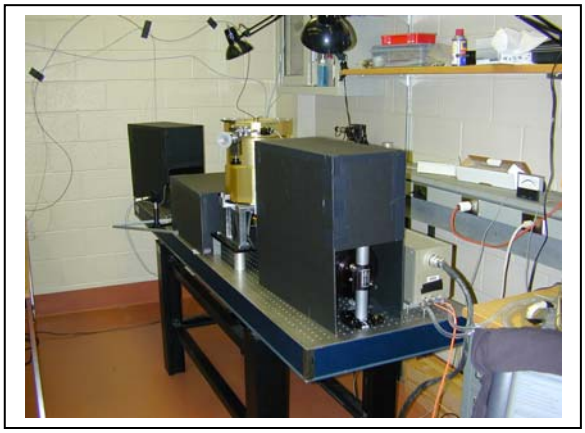

Figure 5-38 Spectrograph in the laboratory

5.6.2.1 Control System

The echelle and XD gratings are in rotational stages and camera is mounted on a linear stage. All these stages are driven with a DC servo motor with incremental encoder position feedback. We use a Newport ESP 300 motion controller with a RS232 interface to a PC for setting and tracking positions. In an ideal situation, we would like not to change anything. However, given the small size of the detector compared the spectral range of interest, we require precision control over both the echelle and cross disperser. The ability to establish and adjust focus with a precision control system is also highly desirable. In reality, we have not adjusted focus since late June.

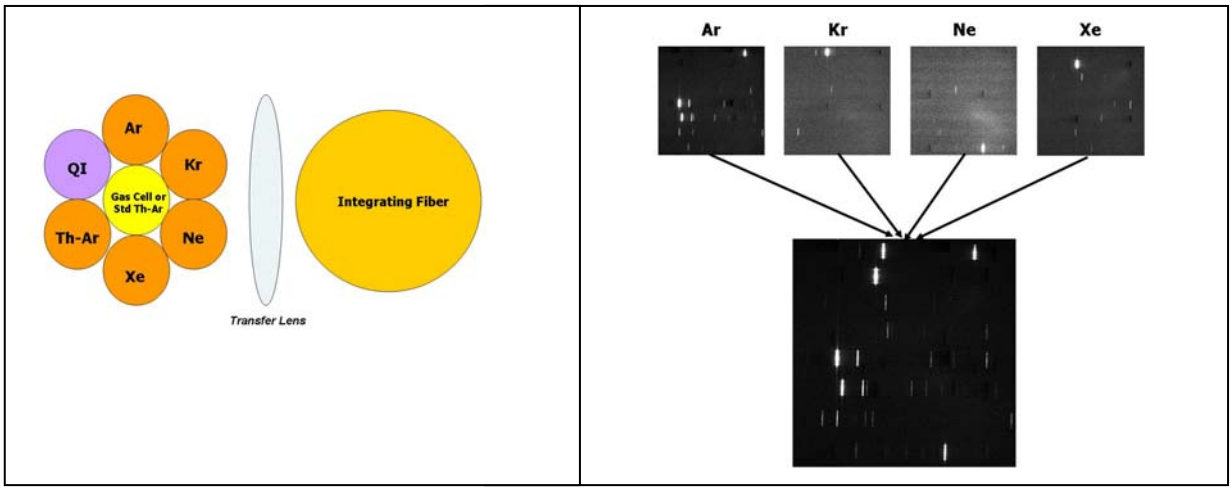

Figure 5-39 Optical fibres arrangement (left) to combine the lamp signals into a single integrating fibre, the output spectrum is shown on the right.

5.6.2.2 Detector & Dewar system

Our detector is a Hawaii 1k science grade array. The systems was provided by IR Labs in Tucson Arizona and uses a SDSU Gen II controller. The dewar is LN2 cooled. Inside the dewar radiation shield we have filter holder mounted to the same cooling block as the detector. The temperature is monitored and is typically 84.3 ^{o}K. Filters currently used are 6 mm PK50 plate to attenuate thermal background beyond 2 microns and a short-pass filter with a cut-off at 1.38 microns and blocked to at least 10^{-3} to 2 microns. The short pass filters are far from optimum and can be used only for the first phase of tests where the relatively short exposures needed for the sun have minimal thermal background. We have not exhaustively characterized the detector but our best current estimate of the gain is 6.1 electrons/ADU and a read noise of 20 e^{-}. We use single destructive readouts at this time.

5.6.2.3 Calibration Unit

The calibration unit has Ar, Kr, Ne and Xe pen lamps as well as a Quartz Iodine (QI) flat field lamp. In the first week of September we added a Th-Ar lamp. We have implemented a scheme using optical fibres to combine the lamp signals into a single integrating fibre as illustrated in Figure 5-39.

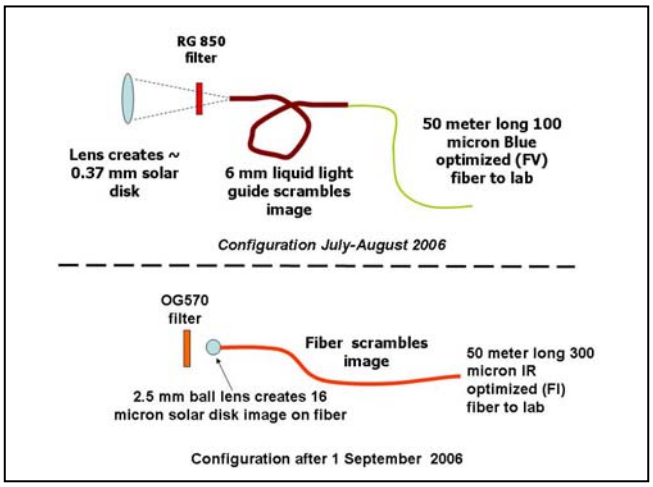

Figure 5-40 Fibre arrangements for obtaining integration Solar disk.

5.6.2.4 Solar Feed

The signal required for our experiment is the integrated solar disk. This is obtained by imaging the Sun onto a fibre which scrambles spatial information. We have used two configurations for this purpose, see Figure 5-40. Both are mounted on an 8 inch Meade telescope that provides solar tracking. Prior to September, we used a simple lens to image the solar disk onto a liquid light guide which was coiled to scramble the image. A RG850 filter is used to protect the light guide. An existing Polymicro 100 micron core FVP fibre cable transmitted the light from the roof of Davey Laboratory to a spectrograph room. This requires approximately 50 meters of cable. The FVP fibre has poor transmission past ~800 nm but worked adequately in the Y band were we have focused our efforts so far. This cable was replaced 1 September with a Polymicro FIP 300 micron core fibre cable, again 50 meters in length. This cable is similar to what we propose for PRVS. The new cable utilized a 2.5 mm ball lens which makes a sub-solar diameter

aberrations dominate the image on the end of the fibre. The fibre end has ~10 degree FOV so tracking errors should not compromise obtaining integrated solar disk light.

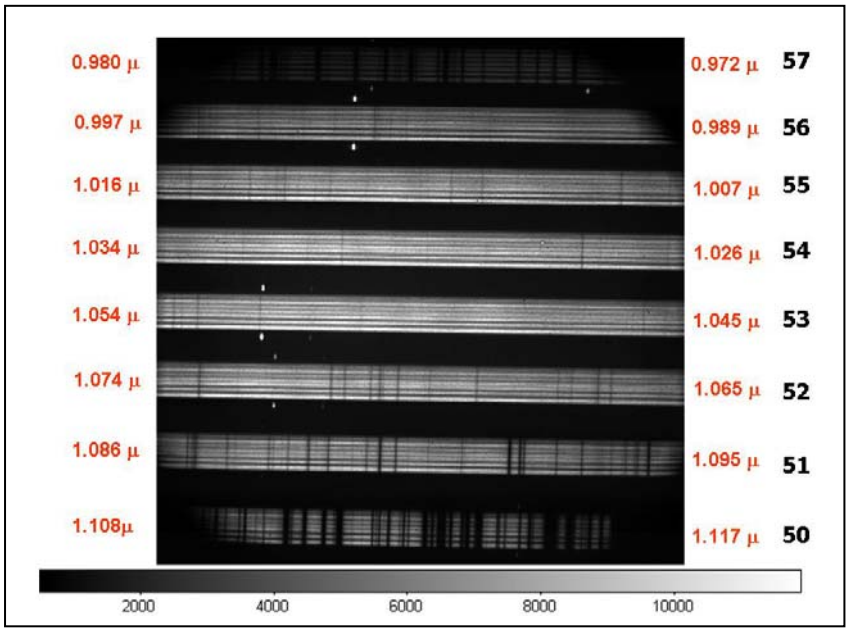

Figure 5-41 Y band spectrum recorded by PRVS pathfinder (August 2006).

5.6.3 Experimental Design

To explore the issues involved with PRV in the near infrared we decided to study our ability to measure the earth rotation signal. This has an amplitude of a few hundred m/sec. This should allow us to make progress on our first three goals. Below we present the progress to date on these goals. Our program has concentrated on a region of the Y band selected to have solar features and enough calibration lines to track spectrograph instabilities. This region is illustrated in Figure 5-41. The numbers on the right indicate the echelle order numbers. Wavelengths increase from right to left and from top to bottom. The red numbers to the right and left of each order indicate the extreme wavelengths cover on the chip in that order. In this region the detectors covers about ~40% of a free spectral range.

5.6.4 Progress on Goals

5.6.4.1 Ability to measure PRV

We have evolved considerably since early July when we began serious data collection and reduction to see a solar signature of earths rotation. Figure 14 illustrates the best results we obtained before we updated our fibre feed and calibration system in September. The orange points represent the CCF results obtained using order 52 and the method described earlier for the simulated M star data and the line is the expected earth rotation signal. The formal error for each point form the CCF is typically 8.5 m/s but there is clearly a systematic effect. This is seen form the residual plotted at the bottom of the chart. The RMS deviation form the expected

earth rotation is ~15 m/s. There is some evidence that that some part of the departure could be due to changing telluric absorption as the data was taken with variable skies and high humidity.

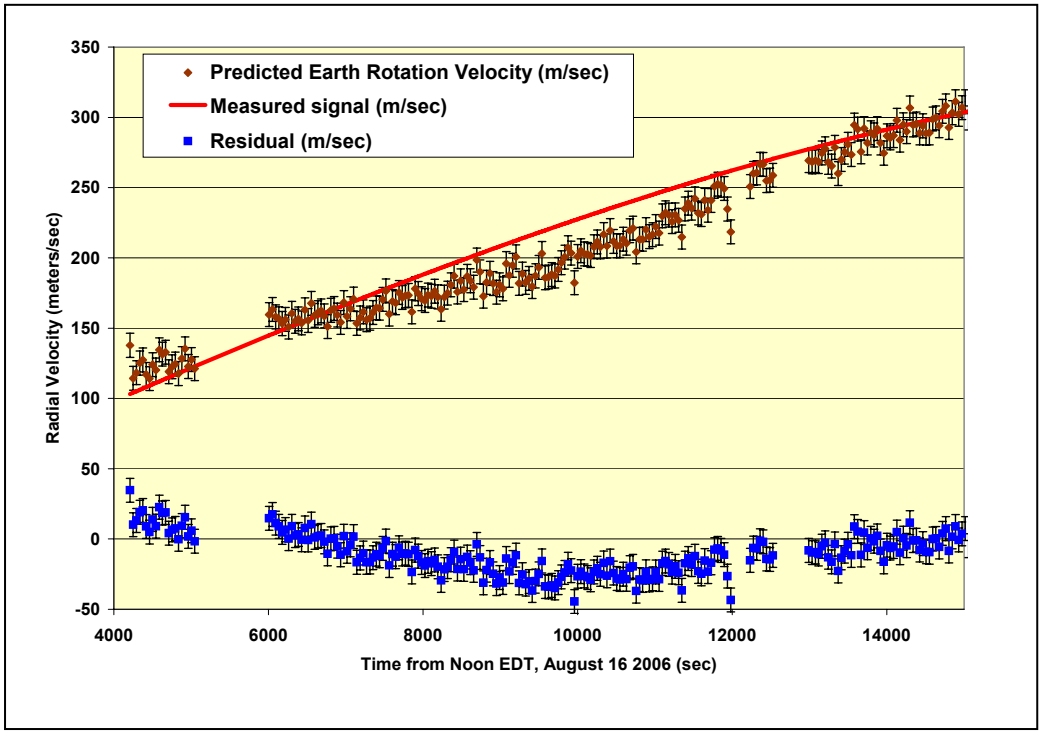

Figure 5-42 A comparison between expected, observed (and residuals) for solar observations.

5.6.4.2 Calibration techniques

We have learned several things regarding the calibration. Perhaps foremost is that when we went for the combined Ar,Kr, Ne, Xe to Th-Ar alone, the number of available reference lines increased by more than a factor of three as is illustrated in Figure 5-43. Secondly, with the closeness of the calibration lines to the object spectrum, separated by one fibre as is the baseline design for PRVS, one has to be exceptionally vigilant on data extraction to avoid contamination of the calibration spectrum by the solar spectrum and visa-versa. We also learned there is significant optical cross talk between adjacent fibres which was somewhat surprising as we measured this in the visible for the Hobby-Eberly MRS project and found it to be less that 10^{-5} but is it considerably more at 1 micron.

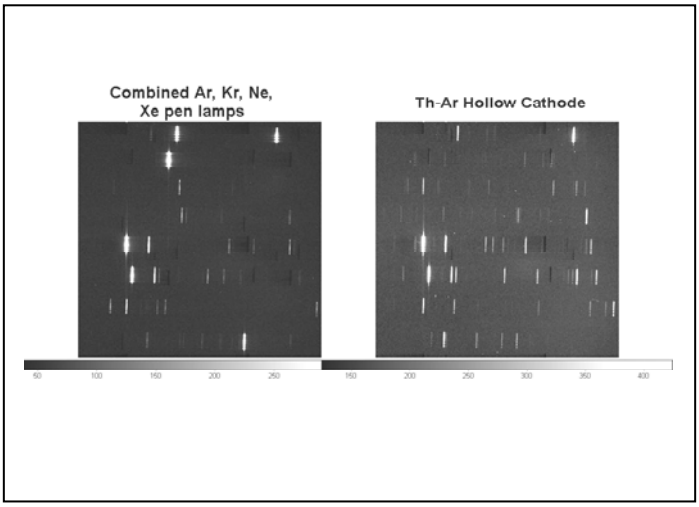

Figure 5-43 Comparison of lines from pen light sources.

5.6.4.3 Modal noise behaviour

We have shown that we can control modal noise in the Y band (discussed in the Fore-Optics Fibre Assembly description, section 3.1.4) but have yet to demonstrate the same in H where it is much more critical.

5.6.5 Plan for the future

We will continue to get Y band data, albeit with a Th-Ar reference, through until around 15th September. We will then change out the short-pass filter to one that has a cut-off at 1.8 microns and select a H band region to look at. We also will do a low sensitivity survey for reference lines throughout the 0.98-1.75 microns range. This will study our ability to control modal noise throughout the PRVS wavelength range.

In late 2006 or early 2007 we plan to move the instrument to HET and have it working on telescope for a commissioning run early in the new year. We will then start a programme of recovery of existing high amplitude planets with an emphasis on understanding our systematics and long-term calibration plans. This process is expected to last at least 6 months though will overlap with our full science phase of measuring v sin i values for PRVS targets and getting first epoch radial velocity measurements for a sample.

5.7 SCIENTIFIC IMPACT

It is hard to underrate the stunning scientific impact of high precision optical radial velocity studies. Our desire is to carry this success into the infrared regime. Our modelling of M dwarf radial velocity signals and experimentation with our pathfinder show that PRVS is feasible. PRVS is thus placed to constrain several exceedingly promising fields of exoplanetary science that might otherwise only be achieved at optical wavelengths by building another generation of larger telescopes. Key answers regarding our knowledge of exoplanets will emerge from a PRVS survey such as:

- How do the properties of exoplanets change from Sun-like to low-mass stars?
- Does the mass of the planets of low-mass stars simply scale with the mass of the central object?
- Do we find the same eccentricity distribution as in solar-mass stars?
- Do we find the same dependence with metallicity as in solar-mass stars? Together with the optical surveys this will enable the mass and metallicity dependence of planet formation to be thoroughly investigated.

Thus PRVS should be able to lay claim to some key historical discoveries. Key headlines emerging from PRVS should be:

- Earth-mass planets
- Earth-mass planets which are habitable
- Earth-mass planets which are habitable around the closest stars.
- How likely are habitable zone planets
- Census of nearby habitable zones
- Formation mechanisms for habitable zone planets

These headlines will inspire astrophysicists, scientists, educators and the general public. PRVS will provide direct inspiration for disciplines such as astrobiology and comparative planetology. The growing interest in exoplanets more generally and the probability of space missions making direct measurement of exoplanets means that PRVS should have a profound affect on the scientific landscape of the early 21st century.

5.7.1 Competition

Some large telescopes already have high resolution infrared spectrographs. CRIRES at the VLT and Phoenix at Gemini South already have similar spectral resolution to that proposed for PRVS though neither is built with stability or radial velocity calibration specifically in mind. Furthermore, they are not cross-dispersed which means their free spectral range is much smaller and they do not have such a good throughput as PRVS. On the timescale of PRVS there may be significant competition from imaging and interferometry projects, though in general the sensitivity of such projects is to young systems with relatively large orbits rather than those in the habitable zones. Thus far no radial velocity exoplanet has yet been definitively confirmed by an imaging system. Microlensing surveys have recently had considerable success at detecting low-mass exoplanets (e.g., Beaulieu et al. 2006) and it is likely that the expanding capabilities of these networks may enable a statistically meaningful sample to be built up within the next five years. In

addition, there is likely to be some overlapping science fulfilled by the many transit surveys, in particular from those with high sensitivity and/or infrared sensitivity: namely COROT, Kepler, UKIDSS and VISTA. The transit projects also have the potential to yield low-mass exoplanets though are only sensitive to a much smaller fraction of exoplanets (and generally at much larger distances). So while they do have great potential to yield statistical properties and useful benchmark objects, they are unlikely to tell us much about nearby planets or provide objects suitable for detailed scrutiny by other techniques. Based on the experience with the existing transit surveys, these missions will require extensive radial velocity follow-up and so their science will actually depend on instruments such as PRVS. Lastly, while transit projects significantly outnumber radial velocity ones (e.g. exoplanet.eu) they have met with little success. There are many reasons for this, however, it is noteworthy that Kepler, the best-funded transit project, will have its own dedicated radial velocity instrument (currently known as HARPS-N which will be an exact replica of HARPS, Mayor, 2006, private communication). However, perhaps the most significant competition will come from other infrared radial velocity instruments such as NAHUAL, GIANO, WINRED, TEDI and our own pathfinder instrument. While it will be essential to learn lessons from these projects, none are significantly further forward or appear to have as developed ideas/projected precisions.

PRVS is a challenging project but it is well-placed to triumph in this most exciting field. The discovery of Earth-mass planets in the habitable zones planets of the nearest stars is a historic feat which is likely to demand an even greater audience than the discovery of exoplanets.

5.8 REFERENCES

Abt H., 2000, ApJ, 544, 933
Adams F.C., Bodenheimer P., Laughlin G., 2005, Astronomische Nachrichten, 326, 913
Alibert Y. et al., 2005, A&A, 439, 1205
Alibert Y. et al., 2005, ApJ, 626, 57L
Allen P. et al., 2006, ApJ, 625, 385
Apai D. et al., 2004, A&A, 427, 245
Bailer-Jones, 2004, A&A 419, 703
Baraffe I. et al., 2004, A&A, 419, L13
Barber et al. 2006, MNRAS, 386, 1087
Beaulieu et al., 2006, Nature, 439, 437
Berger, et al., 2005, ApJ 627, 960
Berger, 2006, ApJ 648, 629
Brott, I., & Hauschildt, P. H. 2005, in The Three Dimensional Universe with Gaia, eds. C.
Bouchy, F., Pepe, F., & Queloz, D. 2001, A& A, 374, 733
Butler et al. 1996, PASP, 108, 500
Butler R.P. et al., 2004, ApJ, 617, 580
Butler R.P. et al., 2006, ApJ, 646, 505
Campbell B., Walker G. A. H., 1979, PASP, 91, 540
Campbell B., Walker G.A.H., 1988,
Chabrier G., Kuker M., 2006, A&A, 446, 1027
Chauvin G. et al., 2004, A&A, 425, L29
Chauvin G. et al., 2005, 438, 25
Connes, P. 1985, Astr. Sp. Sci., 110, 211
Croll et al., 2006, ApJ 648, 607
Cruz K. et al. AJ 126, 2421, 2004

Delfosse X. et al. 1998, 331, 581
Delfosse X. et al., 2004, ASP Conference Series 166, 318
Deming D. et al. 2005, ApJ, 622, 1149
Deming D. et al. 2005, Nature, 434, 704
Deming D. et al. 2006, ApJ, 644, 560
Desidera 1999, PASP, 111, 1529
Dole, S., "life on Other Planets", New Yrok, Blaisdell Pub.
Doppmann et a., BAAS 207, 7426
Duncan D. et al. 1991, ApJS,76.38 (2005, yCat.3159)
Duncan et al., 2005, Catalogue version of Duncan et al, 1991
Endl M. et al., 2006, astroph, 6121
Erskine, D. J. 2003, PASP, 115, 255
Galland F. et al., 2005, A&A, 444, 21L
Galand F. et al., 2005, A&A, 443, 337
Galland F. et al., 2006, A&A, 447, 355
Galland F. et al., 2006, A&A, 452, 709
Grether et al., 2006, ApJ 640, 1051
Gray & Brown, 2006, PASP 118, 1112
Guenther E.W., 2005, in: High resolution IR spectroscopy in astronomy, eds Kaufl H. et al., p. 489
Guenther E.W., 2006, Tenth Anniversary of 51 Peg-b: Status of and prospects for hot Jupiter studies. Colloquium held at Observatoire de Haute Provence, France, August 22-25, 2005. Edited by L. Arnold, F. Bouchy and C. Moutou. Published by Frontier Group, Paris
Hawley S. et al. 2000, ASP Conf. 212, 252
Hatzes A. et al. 2002, Astronomische Nachrichten, 323, 392
Hatzes A., 2005, in: High resolution IR spectroscopy in astronomy, eds Kaufl H. et al., p. 482
Henry, Donahue & Balinuas 2002
Hillenbrand L.A., Raymond R.J., ApJ, 604, 741
Hillenbrand & White, 2004, ApJ, 604, 741
Ida S., Lin D.N.C., 2004a, ApJ, 604, 388
Ida S., Lin D.N.C., 2004b, ApJ, 616, 567
Ida S., Lin D.N.C., 2005, ApJ, 626, 1045
Jayawardhana R. et al., 2003, AJ, 126, 1515
Johns-Krull &Valenti 1996, ApJ, 459, 95L
Jones & Tsuji, 1997, ApJ 480, L39
Jones H. R. A., et al., 2005, MNRAS, 358, 105
Jones H. R. A., et al., 2006, ApJ, 646, 505
Joshi et al., 1997, Icar, 129, 450
Kasting et al., 1993, Icar, 101, 108
Klein R. et al., 2003, ApJ, 593, L57
Koch A., Woehl H., 1984, A& A, 134, 134
Kornet K., Wolf S., Rozyczka M., 2006, A&A,
Laughlin G. et al., 2004, ApJ, 612, L73
Lineweaver C.H., Grether D., 2003, ApJ, 598, 1350
Lissauer J.J., 1987, Icarus, 69, 249
Liu M.C., Najita J., Tokunaga A.T., 2003, ApJ, 585, 372
Lord, S. D. 1992, NASA Technical Memorandum 103957
Marcy G.W., Butler R.P., 1996, ApJ, 464, L151
Marcy G.W. et al., 2001, ApJ, 556, 418

Marcy G.W. et al., 2003, in Scientific Frontiers in Research on Extra-Solar Planets, PASP, p. 1
Martin E.L. et al, 2006, ApJ 644, L75
Mayor M., Queloz D., 1995, Nature, 378, 355
Mohanty, S. & Basri, G. 2003, ApJ, 583, 451
Mohanty S. et al., 2004, ApJ, 609, L33
Morales-Calderon M. et al., 2006, astro.ph, 7537
Muench A.A. et al., 2001, ApJ, 558, L51
Narayan, Cumin & Lin, 2005, ApJ, 620, 1002
Natta A. et al., 2002, A&A, 393, 597
Paulson D.B. et al., 2002, AJ, 124, 572
Partridge H., Schwenke D., 1997, J. Chem. Phys., 106, 4618
Pavlenko Y. et al., 2005, Astronomische Nachrichten, 326, 934
Peale S.J., Lee M.H., 2002, Science, 298, 593
Pinfield, Jones & Steele 2005, PASP, 117, 173
Pollack J.B. et al., 1996, Icarus, 124, 62
Press, W. H. et al., 1992, Numerical Recipes, (Cambridge University Press)
Raymond S.N., 2006, ApJ, 643, L131
Raymond S.N, Mandell A.M., Sigurdsson S., 2006, Science, 313, 1413
Reid et al. AJ 128, 463, 2004
Rivera et al., 2006, BAAS 37, 1487
Rockenfeller, Bailer-Jones & Mundt, 2006, A&A 448, 1111
Saar S., Donahue R.A., 1997, ApJ, 485, 319
Saar S. et al., 2003, CS12, 694
Saar S., Linsky J., 1985, ApJ, 299, 47
Santos N.C. et al., 2004, A&A, 426, L19
Sato B. et al. 2005, ApJ, 633, 465
Setiawan et al., 2004, A&A, 421, 241
Schroeder, D., 2000, « Astronomical Optics », San Diego, Academic Press.
Stepanov A.V. et al., 1995, A&A, 299, 739
Sterzik M.F. et al., 2004, A&A, 427, 245
Stassun et al. 2006, Nature, 440, 311
Tabachnik S., Tremaine S., 2002, MNRAS, 335, 151
Tinney & Tolley, 1999, MNRAS, 304, 119
Turnbull & Tartar, 2003, ApJ Suppl 145, 181
Turon, K.S. O'Flaherty, & M.A.C. Perryman, (ESA SP-576), p. 565
Wallace et al. 1993, NSO Technical Report #93-001
Welsh et al., 2005, AAS 406, 4101
West A.A. et al., 2004, AJ, 128, 426
West A.A., 2006, AJ, in press (astroph/06009001)
Wright J. et al. 2005, PASP, 117, 657

6. OTHER SCIENCE CASES

There are many other scientific cases that PRVS would be ideally placed to take over from the current generation of spectrometers. Certainly the near-infrared echelle spectrometers available to the Gemini community, e.g., PHOENIX, CGS4, CSHELL (and NIRSPEC) have already had long and distinguished careers. They have all been used for an extremely wide range of science. Although PRVS has a clearer science focus than the currently available instruments, this does not detract from its ability to do a wide variety of high-profile science. The stringent instrument requirements for precision radial velocities are also crucial for many other cases. In Table 5 we list some of the areas that PRVS would be exceeding well-placed to exploit, and a subset of these is elaborated in Section 6.9 to 6.15. Little emphasis is placed on cases that can be addressed using existing or upcoming facilities such as NIRSPEC (Keck) and CRIRES (VLT). Since it contains many general cases for high resolution infrared echelles, we refer the reader to the proceedings of a recent workshop: `High resolution Infrared Spectroscopy in Astronomy' (2005, Springer, eds Kaufl H.U., Siebenmorgan R., Moorwood A.), which describes studies of the chemistry, structure, winds and climatology of planetary atmospheres; comets; stellar abundances, pulsations, magnetic fields, disks, inflows, outflows, and the chemistry and kinematics of the interstellar medium (H_2O, OH, etc., and particularly H_3^+).

Science topic	**PRVS contribution**	**Requirement**
Planetary atmospheres	Chemical composition & physics of Solar System planetary atmospheres	Wide spectral coverage
Transiting exoplanetary atmospheres	Measurements of exoplanetary atmospheric composition.	1-1.8μm accurate flatfield accuracy
Brown dwarf spectroscopy	Atmospheric spectroscopy to define BD models (mass, gravity, "weather"). Doppler imaging of BD surfaces. Link to planetary atmospheres.	Wide wavelength coverage Resolution ~10km/s
Absorption lines against GRBs (rapid follow-up).	Follow-up spectroscopy against bright GRBs to measure gas and metallicities at high redshifts. Measure lines of (eg) FeII, MnII, CrII, ZnII for z>2.5	Rapid time to get on-source. Resolution ~10km/s. Wide simultaneous coverage. (Also absorption against bright QSOs)
Stellar magnetic fields	High sensitivity measurements of magnetic fields using Zeeman splitting	R~50,000
Jet & shock physics	Use [FeII] lines to measure extinction, excitation, electron density across line profiles	Simultaneous coverage from 1.0-1.7⌈m Resolution ~ few km/s
Hot protostellar disks	Use atomic lines (eg [FeII], CI, H_2) to probe conditions in disk atmospheres. Measure over line profile to understand geometry.	Simultaneous coverage from 1.0-1.7⌈m Resolution ~ few km/s

Doppler reflected light studies of planets	Doppler shifted stellar light scattered off planet; measurement of albedo, atmospheric composition.	Wide spectral coverage Flat fielding to <0.5% Resolution of few km/s
Rotational velocities of young stars and low-mass stars	Distribution of vsini in young clusters, and of low mass stars	Wide spectral coverage R~50,000
Low-mass spectroscopic binaries	Fraction of spectroscopic M binaries, mass ratios & orbital parameters	Wide spectral coverage R~50,000

Table 5 Other Science from PRVS

6.9 PLANETARY ATMOSPHERES

The spectroscopic study of planetary (and, in some cases, lunar) atmospheres using ground-based facilities is an extremely well established technique for obtaining information about their chemical composition and other properties. In the United States, it has been well understood for several decades that preparations for space missions, the interpretation of *in situ* spacecraft measurements, and the following up of outstanding questions post-mission, benefit enormously from the ability to make one-off measurements and long-term studies from terrestrial telescopes. Hence, for example, the long-running and extremely successful NASA IRTF with its 50% solar system remit: without the IRTF, one can argue, the data obtained by the Galileo probe would have been uninterpretable. This understanding of the importance of ground-based planetary observations is less well established in Europe (particularly in the UK), but has grown in recent years. This is particular pertinent for the JUNO mission scheduled for 2010. PRVS can provide complementary data allowing the dynamics of the jovian magnetosphere and the coupling between the magnetosphere and the upper atmosphere. In particular, the polar orbit will allow JUNO to thoroughly investigate the powerful auroral emissions, in terms of intensity and location, mapping them back into the magnetosphere and correlating them with particle flux and magnetic field measurements.

The infrared region of the spectrum, particularly the near infrared, yields vital information about the abundance and distribution of key molecular species such as H_2, CO_2, CH_4 (and other hydrocarbons), NH_3, H_2S, HCN and many others. By choosing the exact wavelength region/window for study, one can "tune" the observations to a particular atmospheric pressure level of interest. Depending on the temperature of the atmospheric region being studied, it is even sometimes possible to obtain information on H_2O, despite its abundance in the Earth's atmosphere. In more recent years, giant planets have been studied using infrared emission from the simple H_3^+ molecular ion as a probe of their uppermost atmospheric regions, studies which have resulted in considerable progress in understanding the coupling between the local space environment (magnetosphere) and the planet itself.

Much of the ground-based spectroscopic work on planetary and lunar atmospheres has made use of relatively moderate resolution instruments ($\lambda/\Delta\lambda \sim n{,}000$, where n is between 0.1 and 6) to obtain information about temperatures and local and column densities. The improvements in spatial resolution, so that resolutions are regularly seeing limited, and sometimes even diffraction limited, now means that features of the order of 1000 km or less can be studied on a planet like Jupiter. Raster-scanning using long-slit (e.g. 60 × 0.5 arcsec) instruments such as CGS4 (UKIRT) and SpeX (IRTF) enable chemical and temperature maps to be created, which can sometimes also trace long-term atmospheric evolution: for example, the HCN distribution on Jupiter has

been followed post-Comet Shoemaker Levy 9 impact (1994 July), revealing important information about the planet's atmospheric mixing behaviour.

In parallel with moderate spectral resolution studies, higher resolution work – using, in particular, the (robust but ageing) CSHELL spectrometer on IRTF - has made possible the measurement of planetary atmospheric dynamics through studying the Doppler shifting of key emission lines as a function of precise planetary location. It has proved possible to use these studies to characterise the degree to which the space environment is controlled by *external* solar radiation and solar wind inputs, as against *internal* (e.g. atmospheric escape, lunar generated tori and plasma sheets, planetary rotation) sources of energy and material. But we are now right up against (if not already over) the limits of what can reasonably be expected from existing instrumentation. It is clear that if further progress is to be made in understanding how planets interact with their space environments, how that interaction maps onto the planet itself, and how that interaction evolves, then new high-spatial, high-spectral infrared instrumentation is urgently required.

There are many different studies which might be undertaken on Solar System planets such as cloud structure models for Uranus (e.g., Sromovsky et al. 2006), studies of TransNeptunian objects, composition of Near-Earth Objects. Here we focus on a Solar System case utilising the radial velocity stability of PRVS.

6.9.1 Doppler Measurement of Winds in the Atmospheres of Mars and Venus

While it has been possible to develop sophisticated general circulation models for the atmospheres of planets such as Mars (Forget et al. 1999) and Venus (Yamamoto & Takahashi, 2004), the data available to test and constrain these models is currently very sparse. PRVS should enable a new technique of direct Doppler measurements of winds in the middle atmospheres of these planets using observations of the O_2 airglow emission.

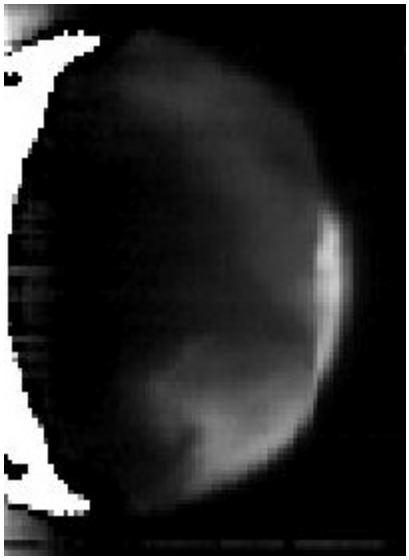

The atmospheres of both Mars and Venus produce intense airglow emission in the 1.27μm $^1\Delta$ band of O_2. This can reach intensities of up to 10MR (Mega-Rayleigh) or more (for comparison in the Earth atmosphere the 5577 airglow line is typically ~300 R and the strong OH lines in the near-IR may reach 10^4 to 10^5 R). The airglow emission was discovered by Noxon et al. (1976) for Mars and by Connes et al. (1979) for Venus. An example is shown to the left, illustrating the airglow distribution over the nightside of Venus (AAT/IRAS2 – Dec 2005). Sunlit crescent is to the left, and peak emission is at the anti-solar point.

The Venus night airglow occurs at altitudes of ~100 km, and this is an interesting transition region between the zonal atmospheric "superrotation" with speeds of ~100m/s, seen at the cloud levels (40-70km), and a subsolar-to-antisolar flow that is thought to be the dominant circulation pattern at altitudes above 120km. This appears to be a region of instability as shown by substantial variability in the O_2 intensity and spatial distribution (Crisp et al., 1996). The dynamics in this region can currently be observed by CO submillimetre observations with large beam sizes (> 10 arcsec) that provide only very coarse spatial information across the planet (Clancy et al., 2005). These show winds that may vary by >50 m/s

over 3000 km spatial scales. Doppler measurements of the O_2 airglow would allow the winds in this highly variable region to be studied with much higher spatial resolution, and probably higher accuracy.

The O_2 airglow on the Mars day-side arises from photolysis of ozone, and is an important tracer of photochemistry (Krasnopolsky, 2003). It arises at altitudes of 20-50km, at which models (Read & Lewis, 2004) predict that the zonal (EW) winds should be strong (50-150m/s). CO submillimetre measurements can also probe this region but spatial resolution is very coarse. Doppler measurements of O_2 emission could provide an important test of Mars GCMs at this altitude.
Doppler measurements of these lines are unlikely to be possible with conventional slit spectrometers, even with high spectral resolutions. This is because the spatial structure of the O_2 emission will give rise to uneven slit illumination that will yield spurious velocities. Only instruments, such as PRVS, designed to minimize such effects and provide precision velocities are likely to be capable of undertaking such studies.

Clancy, R.T., Sandor, B.J. and Moriarty-Schieven, G., 2005, DPS meeting #37, 54.04.
Connes, P., Noxon, J.F., Traub, W.A., Carleton, N.P., 1979, *ApJ*, **233**, L29.
Crisp, D. et al., 1996, *J. Geophys. Res.*, **101**, 4577.
Forget, F. et al., 1999, *J. Geophys. Res.*, **104**, 24155.
Krasnopolsky, V.A., 2003, *Icarus*, **165**, 315
Noxon, J.F. et al., 1976, *ApJ*, **207**, 1025.
Read, P.R., Lewis, S.L., 2004, *The Martian Climate Revisited: Atmosphere and environment of a Desert Planet*, Springer-Praxis.
Yamamoto M., Takahashi, M., 2004, *Geophys. Res. Lett.*, **31**, L09701.

6.10 PROBING THE ATMOSPHERES OF TRANSITING EXOPLANETS

The RV technique has been very successful in providing a large database of exoplanets. However, detailed investigations of these systems cannot be undertaken. This situation is very different in the rare cases that the orientation of the orbit is such that the planet transits its host star. Not only can this give the accurate mass and radius of the exoplanet, but the transit itself is suitable for many detailed follow-up studies. Of great interest is transmission spectroscopy, whereby during a transit light that passes from the star through the outer parts of the planet's atmosphere has impressed on it a spectrographic signature of the atmospheric constituents; this can be observed as extra absorption on top of the stellar spectrum. The major absorption lines in Jupiter-mass exoplanetary atmospheres will be molecular species such as H_2O, CO and CH_4. For transiting planets, these lines will be seen in difference spectra in and out of transit, as the effective planetary diameter will depend on wavelength. With suitable models, this allows one to determine many properties of the planetary atmospheres, such as cloud heights, heavy-element abundances, temperature and vertical temperature stratification, and wind velocities. Note that the atmospheric spectra are likely to be easier to detect against hotter stars, where the photospheric emission is a smooth blackbody curve without molecular absorption lines. However, for smaller stars, the *fractional* absorption during transit will be larger: consequently a Neptune-size planet transiting an M6 star would have the same percentage flux decrement as a Jupiter-size planet transiting a Solar type star.

The crossings of a hot Jupiter in front of the bright star HD 209458 are providing a wealth of fundamental information about this exoplanet, such as mass, radius and density (Charbonneau et

al. 2000; Henry et al. 2000; Mazeh et al. 2000). They have also allowed atmospheric transmission spectroscopy to be performed. *HST* observations, free from telluric contamination, have been a great success. First the sodium D feature was discovered by Charbonneau et al. (2002) with a relative depth of 0.02%, followed by the detection of very strong absorption at the 5–10% level in the ultra-violet from hydrogen, oxygen and carbon (Vidal-Madjar et al. 2003, 2004). The latter most likely comes from the "exo-sphere" of HD209458b, an extended cometary tail of gas evaporating from the planet, caused by its migration close to the star (e.g. Schneider et al. 1998). Due to the limited photometric stability and telluric contamination, ground-based transmission spectroscopy have been less successful. Despite this, work in the near-IR is starting to set constraints on exoplanetary atmospheric models (Moutou et al., 2003; Deming et al., 2005).

We have developed a new method of transmission spectroscopy, more suitable for the ground-based observatories, which utilises the Rossiter effect. PRVS will be the perfect instrument for exploiting this new technique, and will be particularly powerful for probing molecular bands in Jovian planets transiting fast-rotating M dwarfs. It will not only allow determination of the detailed chemistry and composition of the exoplanetary atmosphere, but potentially also constrain planetary rotation, temperature structure, cloud cover, cloud heights, and wind velocities in their upper atmospheres.

6.10.1 Characterisation of the thermal signal of exoplanets

Our ability to detect and characterise the atmospheres of extra solar planets is important if we are to understand how these objects form and evolve. Current technology means that we are now in a position to achieve this goal for the class of objects known as 'hot Jupiters' or Close in Extrasolar Giant Planets (CEGPs) which exist in close proximity to their parent star. Strong irradiation is expected to play a key role in the physical composition of CEGP atmospheres. Current predictions of the form and strength of the emergent spectrum indicate that PRVS can be used to directly measure the planetary signature in a number of systems.

To date three stars with orbiting Hot Jupiters (initially inferred from radial velocity studies) have been observed spectroscopically (e.g., Leigh et al. 2003a,b) at high dispersion in the optical in an attempt to measure the stellar reflected light from the planetary atmosphere. Various models have been invoked to put limits on the fraction of reflected light in these systems which is a function of orbital phase, atmospheric composition and wavelength. These results indicate an upper limit on the grey albedo of the planet HD 75289 of 0.12 for instance, implying $F_P / F_\star < 3e^{-5}$! In the near infrared however, rather than searching for an attenuated copy of the stellar spectrum, we will search for the direct thermal spectrum emerging from the heated atmosphere.

A number of attempts to model the emergent spectrum of CEGPs have been made in recent years. Sudarsky et al. (2003) have calculated emergent spectra for planets with a range of orbital separations from the parent star, including the so-called class of 'hot roasters'. These authors also presented spectra in the 0.4 - 5 μm region for specific systems. For HD 209458, they found a phase averaged flux ratio of $F_P / F_\star < 0.0008$. A re-evaluation of the Sudarsky models by Richardson et al. which include phase dependent effects have yielded flux ratios of up to 0.0013 for a cloudless atmosphere in the case of HD209458. Here, the incident radiation is completely absorbed and re-emitted on the day-side of the planet. A more recent study by Barman et al. (2005) which models the day-night gradients has yielded similar results to previous studies. For no redistribution of heat (re-emission of radiation on dayside), they find $F_P / F_\star < 0.00125$, while

uniform redistribution of the incident radiation yields $F_p / F_* < 0.00089$ at all phases for HD 209458. It is thus apparent that the NIR spectroscopic signature is likely to be at least an order of magnitude greater than the reflected light signature.

Thus it is appropriate to extend previous reflected-light searches towards the near-IR where thermal emission from CEGPs are predicted to make a 25-30 times higher contribution toward the total flux received from the star-planet system. The detection of thermal emission during the secondary transit of TrES-1b indicates flux ratios of 0.0007 at 4.5 microns and 0.0022 at 8.3 microns, consistent with the Sudarsky et al. (2003) model, whilst the more recent HD189733b result (Deming et al. 2006) returns a higher than predicted planet/star contrast of 0.0055, albeit at longer IR wavelengths. The TRES-1 observations are consistent with the models though the HD189733b signal suggests the models are seriously underestimating the thermal flux.

Whereas the TrES-1b, HD209458b and HD189733b thermal detections were photometric, we believe a spectroscopic approach can deliver significant information about the atmospheric nature of the target system. We will be able to determine the following important characteristics.

(1) Projected orbital velocity, K_p , which when combined with existing stellar radial velocity results will yield the orbital inclination of the system and the true planet mass.

(2) Planet/Star flux ratio, which would allow predictions for the atmospheric temperature and/or radius, and subsequent comparisons with existing theoretical models

(3) With strong detections we can measure phase function of the planet. Barman et al. (2005) obtain a phase function for their different models. In the case of no redistribution of heat, the flux ratio as a function of phase drops away rapidly as the planet moves away from conjunction (i.e. phase = 0.5). When heat is redistributed uniformly over the inner face of the planet, this drop of in flux ratio is initially less pronounced, whereas efficient redistribution of heat will show now variation in F_p / F_* with phase.

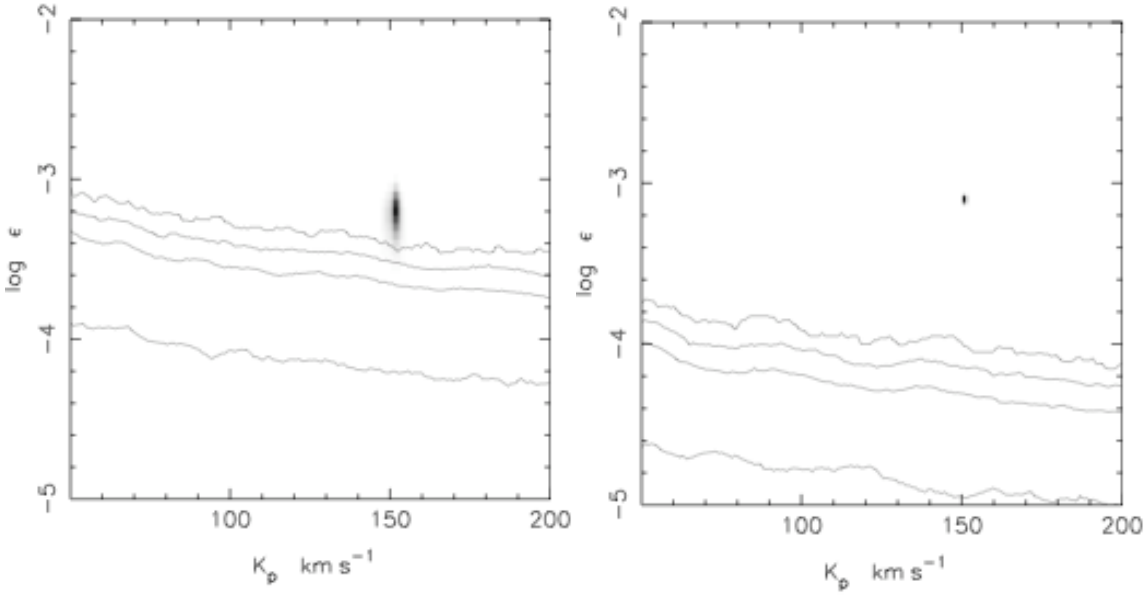

Figure 6-1 Chisq flux ratio-Velocity amplitude plot for HD17949b (*a*=0.044 AU, *P*=3.09d, *M*sin*i*=0.916M_{Sun}, 1000K COND model planet, 6000K Kurucz model star, *R*p=1.6R_{Sun}. The planet is correctly recovered at log10 (ε) = log10 (F_p / F_*) = -3.09 and K_p = 153. The maximum F_p / F_* flux ratio is 0.0008 when the full irradiated inner face is seen (i.e. phase 0.5). The phase function used is Venus-like phase function which is similar to the results in Barman et al. (2005). The maximum value of ε = F_p / F_* is 0.0008 (1 part in 1250) and is consistent with Sudarsky et al. (2003) models for HD209458.

We would obtain densely sampled time series spectra of the star plus planet. Each observation will contain a stellar spectrum and a phase dependent Doppler shifted spectrum of the planet. We would observe the system when the planet is close to conjunction, but not eclipsed by the star (i.e. at phases close to and on either side of 0.5). Thus, if the inner face of the planet is strongly heated through irradiation, and the heat is not effectively redistributed, we expect the strength of the planetary signature to be at it's greatest at these phases. This will enable us to maximise our chance of detecting the planetary signature. By observing at these phases, we will also sample the greatest range of Doppler shifts of the planetary spectrum. We construct a high S/N ratio model of the stellar spectrum to accurately subtract the unshifted starlight from each observed spectrum. This will additionally have the benefit of largely removing the telluric water vapour lines prevalent in this part of the spectrum. We will additionally monitor the strength of these features, which vary through the night, by observing a bright telluric standard star. The residual spectrum will contain a Doppler-shifted copy of the planetary spectrum which at this stage is still deeply buried in the noise. To overcome this, we model the planet's spectrum as the convolution of an unknown Doppler-shifted mean line profile and an absorption line pattern for a Sudarsky et al. (2003) class V hot Jupiter. The profile is recovered through use of a least-squares deconvolution method. We can model the changes for each possible projected orbital velocity amplitude K_p , incorporating time-dependent changes in Doppler shift and to a lesser extent, brightness. We then scale this model to give the best inverse-variance weighted fit to the data. The statistical significance of the result is assessed using boot-strap statistical procedures based on the random re-ordering of the data in a way that scrambles phases while preserving the effects of any correlated systematic errors. This process yields the joint probability of the model parameters as a function of orbit velocity, K_p , and planet/star flux ratio. To calibrate any candidate detection, we construct a simulated planet signal that is added to the extracted spectra prior to analysis. By ensuring the fake planet is recovered correctly by our procedures, we can be confident of a calibrated detection in the presence of a genuine planet signal.

The input S/N ratios vs output S/N ratios are tabulated below:

Band	λ (μm)	In S/N	Out S/N	No. echelle orders	No. of lines	log_10(ε)
Y	1.00-1.08	400	1380	8	2528	3.20
J	1.20-1.32	200	2500	12	3002	3.18
H	1.50-1.75	200	4700	25	5094	-3.15

In the Y band, the lines are very weak and closely spaced. To get a detection above the 99.99% confidence level, it was necessary to start with an input S/N ratio of 400. The values for log ε, which correspond to star/planet flux ratios of 1575, 1515 and 1430 respectively in these bands are pretty close. The values are derived by assuming ε = -3.08 (star/planet flux ratio = 1250) for the K band for HD 209458. The Burrows spectrum for 0.05AU CEGP objects were used to get the values for Y, J, H after scaling the spectrum to give 1250 for the 2.2 micron K band. Our chosen example of HD 179949 is a F8 main sequence star with an apparent visual magnitude of V=6.25. While it is probable that it will be plausible to do this with CRIRES, the lower throughput and lack of multiband capability means that it will be very much slower and will be difficult to apply to all the CEGPs.

6.10.2 A new method using the Rossiter effect

Snellen (2004) has developed a method for probing the atmospheres of transiting exoplanets, making use of the Rossiter effect. This will be particularly powerful in the near-infrared using PRVS. Anticipating the discovery of exoplanets transiting fast-rotating M dwarfs, using this new technique PRVS could improve the precision currently obtained with the *HST* by 1–2 orders of magnitude.

Due to the rotation of the host star, a transiting planet will first block off light from the approaching and then from the receding parts of the stellar surface. This results in an artificial wobble in radial velocity, an effect first observed by Rossiter (1924) for the eclipsing binary β Lyrae. The amplitude of this signal is directly proportional to the effective size of the transiting planet, and the wavelength dependence of this effect can reveal atmospheric absorption features in the same way as with transmission spectroscopy. The advantage of this method is that it does not rely on accurate photometric comparison of spectra in and out of transit, but instead depends on relative velocity shifts of stellar absorption lines in the same in-transit spectra.

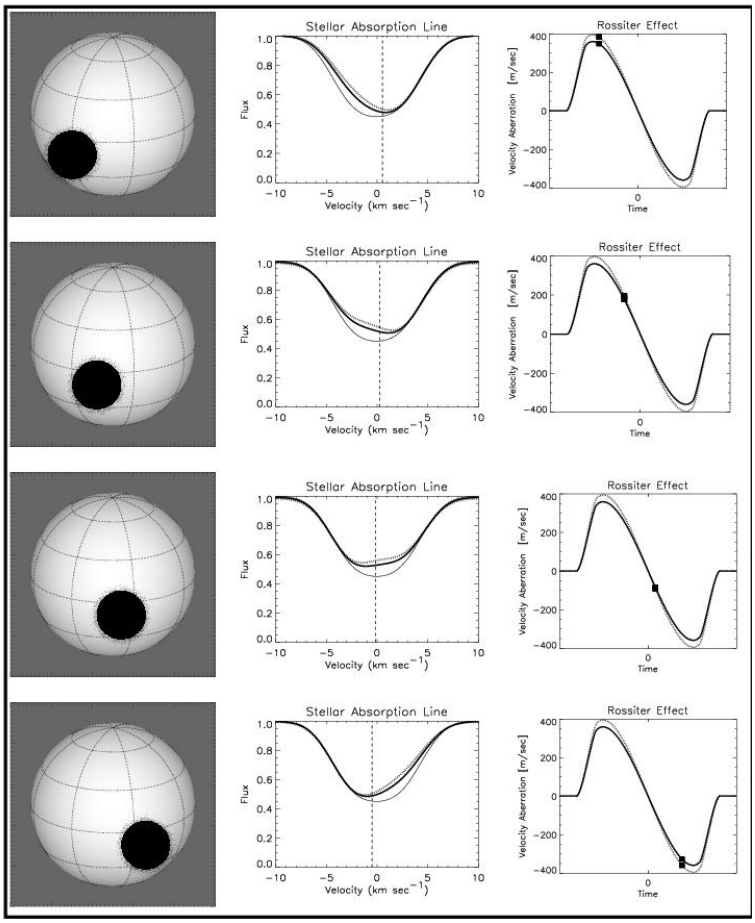

Figure 6-2 Illustration of the Rossiter effect, caused by a dark object transiting a rotating star. Since the object subsequently blocks the approaching and receding parts of the stellar surface, a change in the profile of the rotationally broadened stellar absorption line occurs, which results in an effective red and blue shifting of the line. The perturbed and unperturbed absorption line profiles are shown in the middle panels by the thick and thin solid lines respectively. The resulting Rossiter effect is shown in the panels to the right. The effect of extra absorption caused by a possible atmosphere is indicated by the dotted lines. In fast-rotating M dwarfs, the transit of a Jupiter-size planet will produce a Rossiter effect with an amplitude of 1–2 km/s.

We have successfully applied this new method to the sodium D absorption feature of HD209458b using archival VLT/UVES data (Snellen 2004). The amplitude of the Rossiter effect (about 40 m/s) was found to be 1.7 ± 1.2 m/s higher in the sodium D lines than in the weighted average of all other absorption lines in the observed wavelength range, corresponding to an increment of 4.3 ± 3% (1.4σ - see Figure 6-3). Although this is not a formal detection, the uncertainty in this measurement compares to a photometric accuracy of 5×10^{-4} for conventional atmospheric transmission spectroscopy, more than an order of magnitude better than previous attempts using ground-based telescopes (0.05% compared to 1-2%). In addition, the data showed that specifically designed observations would result in a further increase in accuracy of a factor 2–3.
An additional bonus is that this effect can be used to obtain the alignment between exoplanetary orbital axis and the stellar spin axis, and has recently been used to measure this to an accuracy of ~1 degrees (Winn et al., 2006).

6.10.2.1 Probing exoplanet atmospheres with PRVS

The near-infrared is a particularly interesting wavelength regime to probe the atmospheres of transiting exoplanets, since this is where their transmission spectra are dominated by the molecular bands of H_2O, CO and CH_4 (see Figure 6-4). The great advantage of these particular features is that they involve many tens of absorption lines and that therefore potentially a √n increase in precision can be achieved with the simultaneous broad wavelength coverage of PRVS. Probing the Rossiter effect with PRVS will be most powerful with late-type M stars for three reasons:

1 The near-infrared molecular absorption lines in M dwarfs (needed to measure the Rossiter effect) are much stronger than in solar-type stars.
2 M dwarfs are relatively bright in the near-infrared, and the ratio of planetary to stellar size is much more favourable (by more than an order of magnitude for spectral type later than M6).
3 Almost all late-type M dwarfs are fast rotators, while the amplitude of the Rossiter effect is directly proportional to the star's rotation velocity.

The strengths of the planetary absorption features will give us great insights in the detailed physics in the upper atmosphere, and e.g. depend on photo-ionisation from the intense stellar radiation, chemistry and chemical composition, temperature structure and the formation of clouds (Figure 6-3). If sufficient precision can be achieved, cf. for a Jovian planet transiting a bright, fast-rotating late M dwarf, potentially the absorption line profiles could be measured. This would constrain planetary rotation and the wind velocities in the upper atmosphere (Figure 6-3). This precision would only be possible by finding a relatively large planet transiting an M dwarf; nevertheless this provides an amazing prospect that we could obtain such detailed information about an exoplanetary system.

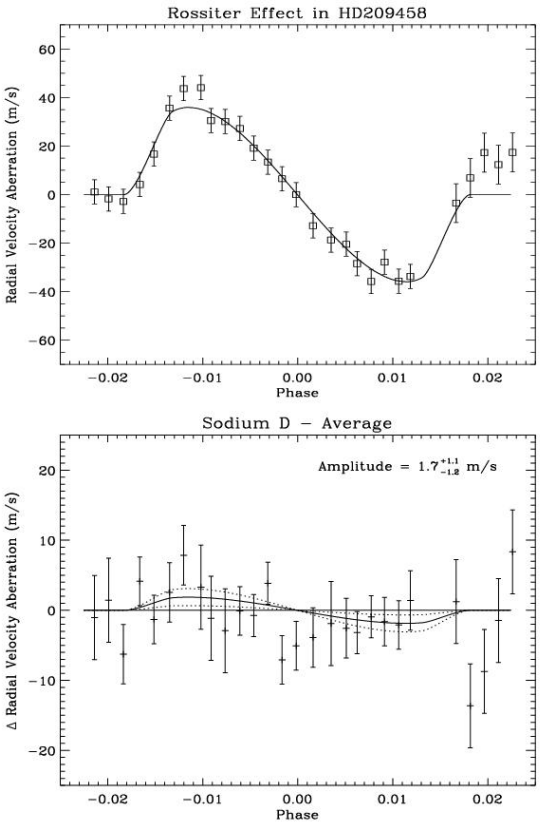

Figure 6-3 The Rossiter effect as observed for HD 209458 using an archival UVES/VLT dataset covering 4 transits showing the relative excess in the Rossiter effect for the two sodium D lines. 1σ confidence limits are indicated by the dotted lines. The best-fit model shows an excess of 1.7 (+1.1, -1.2) m/s (1.4σ).

6.10.3 Technical Information

6.10.3.1 The brightest transited M dwarfs

Although so far only three bright transiting system (HD209458a/b, HD189733, and HD149026 at V=7.6-8.2) have been discovered, (with a few other systems at much fainter magnitudes), it can be expected that many more of such systems will be discovered before the end of the decade. An important question for this project is at what magnitude the brightest M stars with transiting exoplanets will be found? This can only be roughly estimated because no detailed statistics of the M dwarf exoplanet population are available (only two M dwarf/planet systems have been found so far, but this is still driven by selection effects). Assuming that the exoplanet population for M dwarfs is the same as for solar-type stars (not the expectation in some models due to the lower gravitational field and lower disk mass), we can predict that about 1.5% of the M dwarf population will have hot Jupiters, with 15% percent of those having a viewing angle such that they transit. However, as noted above, the smaller radius means that transiting Neptunes may be detectable around M stars, increasing the number of potential targets considerably. Just taking the case of transiting Jupiters, this implies that roughly the 400-500th brightest M dwarf will have a transiting planet. Data from the Research Consortium of Nearby Stars (RECONS) indicate that such a star will be at a magnitude of J=~11.

Another way to look at the problem is to ask how many M-star transits may be discovered that are observable rather than which is the brightest. Ground-based all-sky surveys, such as SuperWASP, will not go deep enough (they are visible wavelength searches) to see J=11 M dwarfs with a 1% photometric accuracy (limit V~13, V–J >3). *Kepler* and *COROT* similarly do not expect to observe many M stars. The real hope, therefore, is for transits of M dwarfs resulting just from RV measurements based on the PRVS survey. From Section 5, we will observe a total of ~700 M dwarfs. Based on the statistics above, we may therefore have only one more transiting Jupiter from our survey, but with the potential of many more lower-mass transiting planets. Overall it seems like there may be a few to follow up. Therefore although by using many lines we may be able to detect planet atmospheres in M dwarf transits fainter than J=11, the limit is probably set by the number of M-dwarf transits discovered.

6.10.3.2 Amplitude of the Rossiter effect for fast-rotating M dwarfs

The Rossiter effect in the well-known HD 209458b system has an amplitude of 38 m/s, which is governed by the rotation velocity of the star, and the ratio of the size of the planetary and stellar disk. Not only will this ratio be more favourable for late M star/Jupiter systems by about a factor 10, late M dwarfs are known to be fast rotators (see Figure 5-17). Assuming a rotation velocity v sin i of 10-20 km/s, the Rossiter effect will have an amplitude of 1-2 km/s, a factor 25-50 times higher than in HD 209458.

6.10.3.3 Expected accuracy

The accuracy of this experiment is photon noise limited. To sample the Rossiter effect during a ~1hr transit adequately, the observations need to be divided into exposures of 5 min. A S/N~250 per pixel per exposure will need to be reached for a J=11 star, which will roughly result in an accuracy in relative position of 10 m/s for the strongest lines, for each of the 10-15 exposures during a transit. This means that the amplitude of the Rossiter effect can be measured to an accuracy of ~2-3 m/s per line, corresponding to a S/N=400-800. The detection of sodium in the atmosphere of HD 209458b (Charbonneau et al. 2002) at a photometric level of 0.023% corresponds to a variation in the scale height in HD 209458b of 700km (0.7% of its radius). The accuracy derived above means that for a fast-rotating M dwarf, using a single absorption line, variations in the effective radius of a Jupiter-size planet of 0.1%, corresponding to ~50-100km could potentially be detected per stellar line. The great advantage of PRVS will come from the fact that the molecular features consist of tens to hundreds of lines can be observed simultaneously, resulting in a sensitivity gain of an order of magnitude.

Finally, there is the tantalizing prospect of detecting the atmosphere of terrestrial planets. Ehrenreich et al. (2005) presented the first study of atmospheric signatures of transiting Earth-size planets. They estimate the effective size of the planetary disk in atmospheric absorption features to be ~6/84 larger (their model C1). Hence the Rossiter effect would be 5% larger at these wavelengths. Assuming a late M-dwarf with a radius of 0.1 $R_{\odot}$, and a v sin i = 10 km/s, an Earth-size planet would produce a Rossiter effect with an amplitude of 100 m/s. A 5% effect would produce a radial velocity aberration of 5 m/s, which could be detectable with PRVS.

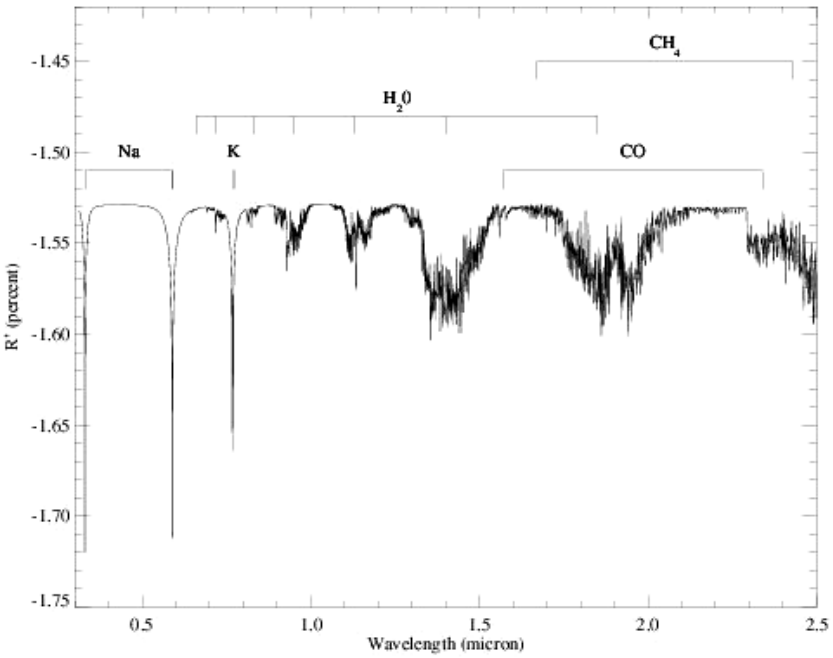

Figure 6-4 Model transmission spectrum for a transiting hot Jupiter showing the absorption bands due to H_2O, CO and CH_4 (from Brown 2001).

References:

Barman T. et al., 2005, 632, 1132
Brown T.M., 2001, ApJ, 553, 1006
Charbonneau D. et al. 2000, ApJ, 529, 45
Charbonneau D. et al. 2002, ApJ, 568, 377
Charbonneau et al., ApJ, in press
Deming D. et al., 2005, ApJ, 622, 1149
Deming D. et al. 2005, Nature, 434, 740
Deming D. et al. 2006, ApJ, 644, 560
Ehrenreich et al., 2006 A&A, 448, 379
Henry G.W. et al., 2000, ApJ, 529, L41
Leigh C. et al., 2003, MNRAS, 346, 16
Leigh C. et al., 2003, MNRAS, 344, 1271
Mazeh T. et al., 2000, ApJ, 532, L55
Moutou et al., 2003, A&A 405, 341
Richardson J. et al., 2003, ApJ, 597, 581
Rossiter R.A., 1924, AJ, 60, 15
Schneider J. et al., 1998, in Brown Dwarfs & Extrasolar Planets, eds Rebolo M., Zapatero O.
Snellen I., 2004, MNRAS, 353, L1
Sudarsky D., Burrows A., Hubeny I., 2003, ApJ, 588, 1121
Vidal-Madjar A. et al., 2003, Nature, 422, 143
Vidal-Madjar A. et al., 2004, ApJ, 604, L69
Winn et al., 2006, astro-ph/0609506

6.11 BROWN DWARFS

The brown dwarf regime connects stars to planets. It covers a mass range of a factor of 10. While intrinsically fascinating objects with a rich molecular chemistry, the most general question that we wish to answer relates to the brown dwarf mass function. UKIDSS and *Spitzer* are poised to find large numbers of new objects. However, the key to understanding these objects is to be able to take high-resolution spectra that enable compositions, temperatures and gravities to be measured. Based on L and T dwarfs, high-resolution spectra should be by far the most efficient method for gravity and thus mass determination. Furthermore high-resolution spectra will enable isotopic ratios (pristine from formation) as well as magnetic fields and weather, thus establishing links with planetary atmospheres.

6.11.1 Benchmark Brown Dwarfs

The lack of knowledge of the true masses of VLMSs and BDs at young age is a severe problem for this field of research. Infrared photometric monitoring programmes from transit programmes such as UKIDSS (Pinfield et al.) or targeted searches such as Bailer-Jones et al. (2006) performed on smaller telescopes) will discover eclipsing signals. PVRS can conduct follow-up of such systems to fully characterise system parameters.

PRVS will also allow to study the atmospheres of low-mass objects in detail, because it is possible to obtain spectra covering simultaneously Y, J and H. Such observation would allow to determine $T_{\rm eff}$, log g and the abundances, for example.

6.11.2 Surface gravities of field ultra-cool dwarfs

In the last decade, a large population of ultra-cool dwarfs has been discovered by wide-field surveys such as 2MASS, SDSS, and DENIS. The spectra of these dwarfs were sufficiently distinct from those of the M dwarfs, that the creation of two new spectral classes, L and T, was warranted (Kirkpatrick et al. 1999; Burgasser et al. 2002). The L dwarfs are a mix of very-low-mass stars and brown dwarfs (BDs) while the T dwarfs are exclusively BDs. Since ultra-cool dwarfs bridge the gap in mass between the more massive stars and less massive planets, their atmospheres and interiors exhibit an interesting mix of phenomena found in both stars and giant planets. As a result, they are an important test of interior and atmospheric models that will be critical in determining the properties of extra-solar giant planets.

Recently, focus has shifted away from finding ultra-cool dwarfs to determining their fundamental atmospheric parameters, $T_{\rm eff}$, log g, [m/H]. Typically, $T_{\rm eff}$ is estimated by combining an observationally derived $L_{\rm bol}$ with a theoretically calculated radius (assuming an age). Golimowski et al. (2004) determined the effective temperatures for a large sample of ultra-cool dwarfs using this technique but the errors can be quite large (~300K) due to the unconstrained ages of isolated ultra-cool dwarfs (typically a range of ages from 0.1 to 10 Gyr is assumed). With the exception of brown dwarfs found in binary systems, log g is the only way to derive masses for (old) field L and T dwarfs.

Determining the log g of ultra-cool dwarfs has proven to be more difficult. There have been studies that have empirically identified gravity-sensitive features in the spectra of BDs. Gorlova et al. (2003) and McGovern et al. (2004) found the K I (1.2μm) and Na I lines (1.15μm) were systematically weaker in the spectra of the young BDs compared to field BDs of the same spectral type. Although it is evident that there are gravity-sensitive features that can be used to

discriminate between field BDs and BDs found in young clusters ($\Delta \log g = 1.5$), these features (at these resolving powers) are not useful for determining more precise surface gravities of isolated field BDs.

Mohanty et al. (2004) developed a technique that uses R=31,000 red optical spectroscopy to determine the effective temperatures and surface gravities of very young BDs to ±50K and ±0.25 dex, respectively. They use the gravity-insensitive TiO bands at 0.844μm to determine effective temperatures and the temperature-insensitive Na I lines to determine surface gravities. However there are a number of problems with extending this technique to the field L and T dwarfs. First, the TiO bands weaken and disappear in the early-type L dwarfs (Kirkpatrick et al. 1999) due to the formation of dust (Lodders 2002). Second, the Na I and K I lines are highly pressure-broadened in the L dwarfs and T dwarfs. Although they may remain sensitive to changes in surface gravity, the pressure-broadened wings of the lines are difficult to model (Burrows & Volobuyev 2003). Finally, the ultra-cool dwarfs become progressively redder and fainter with decreasing effective temperature as the peak of the Planck function shifts to longer wavelengths. An obvious solution to these problems is to move the near-infrared.

There are very few published high-resolution (R>10,000) near-infrared spectrum of an L or T dwarf (though we note that a large sample of R=20,000 spectra will soon be published as part of the NIRSPEC BD survey; however, these will be limited to the J band alone). Smith et al. (2003) obtained an R=50,000 spectrum of the binary T dwarf, ε Ind Ba. The spectra included two ~7-nm-wide sections of the H and K bands. Nevertheless, they measured the $T_{\rm eff}$ and $\log g$ of the BD to ±100K and ±0.3 dex, respectively. One of the advantages PRVS brings to the study of ultra-cool dwarfs is its large wavelength coverage. At R=70,000, there will be thousands of features, both atomic and molecular, that can be fit *simultaneously* to constrain both the $T_{\rm eff}$ and $\log g$ of ultra-cool dwarfs. The work of Lyubchik et al. (2004) indicates that the Y, J and H region is rich with lines of interest. There are plans to measure the oscillator strengths for the diagnostic infrared species (e.g., Jones et al. 2005)

6.11.3 Outstanding Issues:

- ***Models:*** Although we may have given the impression that the models are 100% accurate, this could not be further from the truth. These models are very complex due to the millions of molecular lines that must be included in the opacity calculations. There can be significant differences between various modelling groups, so errors of ±50K in $T_{\rm eff}$ and ±0.25 dex in $\log g$ are optimistic at this point.
- ***Dust:*** The presence of condensates significantly alters the emergent spectra of ultra-cool dwarfs. In the L dwarfs, the condensates forms clouds that are difficult to model and add an extra degree of freedom besides the canonical $T_{\rm eff}$, $\log g$ and [m/H]. We will look into the effects of clouds once we have the new models completed. In the T dwarfs, the problem is not nearly as severe because the clouds have dropped below the observable photosphere (the effects on the chemistry of the atmospheres are better understood than the opacity contributed by the clouds). However, these are much fainter than the L dwarfs making the observations more difficult.
- ***Metallicity:*** Since the models we are using have not been computed for sub-Solar metallicities, we do not know how large an effect metallicity will have. [m/H] is the `B field' of BDs. The modellers will create sub-Solar metallicity models, but probably not before 2006.

- ***Rotation:*** Rotation will confuse things since it will both broaden and shallow-out the lines. It is not clear how this problem can be surmounted.
- ***Rotation/Spectral resolution:*** For low v sin i objects the high resolution of PRVS will be invaluable for spectral identification.

6.11.4 Weather on Brown Dwarfs

Early studies of rotation distributions in intermediate-age open clusters revealed an abrupt drop in rotation rate at the mid-F spectral types. Stars later than this break possess outer convective zones, in which dynamo activity can generate a magnetic field. This field erupts through the stellar surface into the corona where it becomes stressed by photospheric surface motions. The dissipation of this stored energy heats the coronal gas to million-degree temperatures. Some of this gas escapes along open field lines. This hot, magnetically-channelled wind carries away angular momentum, spinning the star down.

It is now a decade since Basri & Marcy (1995) discovered a surprise at the bottom of the main sequence. The L dwarf BRI 0021-0214, despite being a rapid rotator, showed very low levels of chromospheric activity. Subsequent statistical studies confirm that even among the old disk population, there is an abrupt rise in rotation rates at spectral types later than M9 or so. The projected rotation rates found in surveys of L dwarfs range from 10 to 40 km s^{-1}, corresponding to spin periods of order 2 to 8 hr. Thus although these objects are fully convective and as capable as the Sun or Jupiter of generating strong magnetic fields in their deep interiors, they have suffered no more magnetic braking than has Jupiter.

The fraction of stars showing chromospheric Hα emission (Figure 5-16) rises from 20% at M5 to 100% at M7 and M8, then declines equally steeply in the early L types (Gizis et al. 2000). X-ray emission is almost absent among L dwarfs, yet occasionally they manage to show flare activity (Rutledge et al. 2000; Schmitt & Liefke 2002; Briggs & Pye 2004; Stelzer 2004). L dwarfs also exhibit quasi-periodic photometric variability, whose nature remains a mystery (Bailer-Jones & Mundt 1999, 2001; Martin et al. 2001; Clarke et al. 2002a,b). Explanations range from local magnetic suppression of convective flux to give residual star-spot activity to patchy "weather" patterns giving holes in the dusty cloud decks of the cooler L dwarfs. Past attempts to detect rotational modulation in the equivalent widths of dust-sensitive spectral features have not yielded detectable signals, even in objects exhibiting broad-band photometric variability (Bailer-Jones et al. 2002, Rockenfeller et al. 2006, Clarke et al. 2003). This suggests the weather patterns may be quite complex. They will not produce measurable spectral signatures at the low spectral resolutions employed to date, unless there is a strong hemispheric asymmetry in the dust distribution.

6.11.5 Immediate Objective:

The line profiles of the late M and L dwarfs are so strongly broadened by rotation that we will be able to bring both conventional Doppler imaging techniques to bear on them. PRVS will allow us to map brown-dwarf weather patterns in detail using a variant of conventional Doppler imaging.

The influence of weather on the variability of brown dwarfs can be understood in terms of the effect of dust opacity on the emergent spectrum. Detailed modelling by Allard et al. (2001) shows that dusty atmospheric models generally give the best fits to the observed spectra of low-mass objects. Models in which the dust has precipitated out of the atmosphere have deeper,

hotter photospheres and stronger absorption lines from molecular and atomic species in the overlying layers. This contrast in spectral properties between clear and dusty regions is expected to distort the rotation profiles of individual absorption lines. Dark star-spots produce pseudo-emission bumps in the profiles of hotter, magnetically active stars in much the same way. We have simulated the temporal variations in the average rotation profile of a star with T_{eff}=1,900K and v sin i = 60 km s^{-1} (Figure 6-5). Rotationally-broadened line profiles synthesised from a stellar model with a complex pattern of dusty and clear patches show strong travelling wave distortions, even though their total equivalent widths do not vary significantly. We can, moreover, recover maps of the dust distribution over the stellar surface using MaxEnt image reconstruction algorithms.

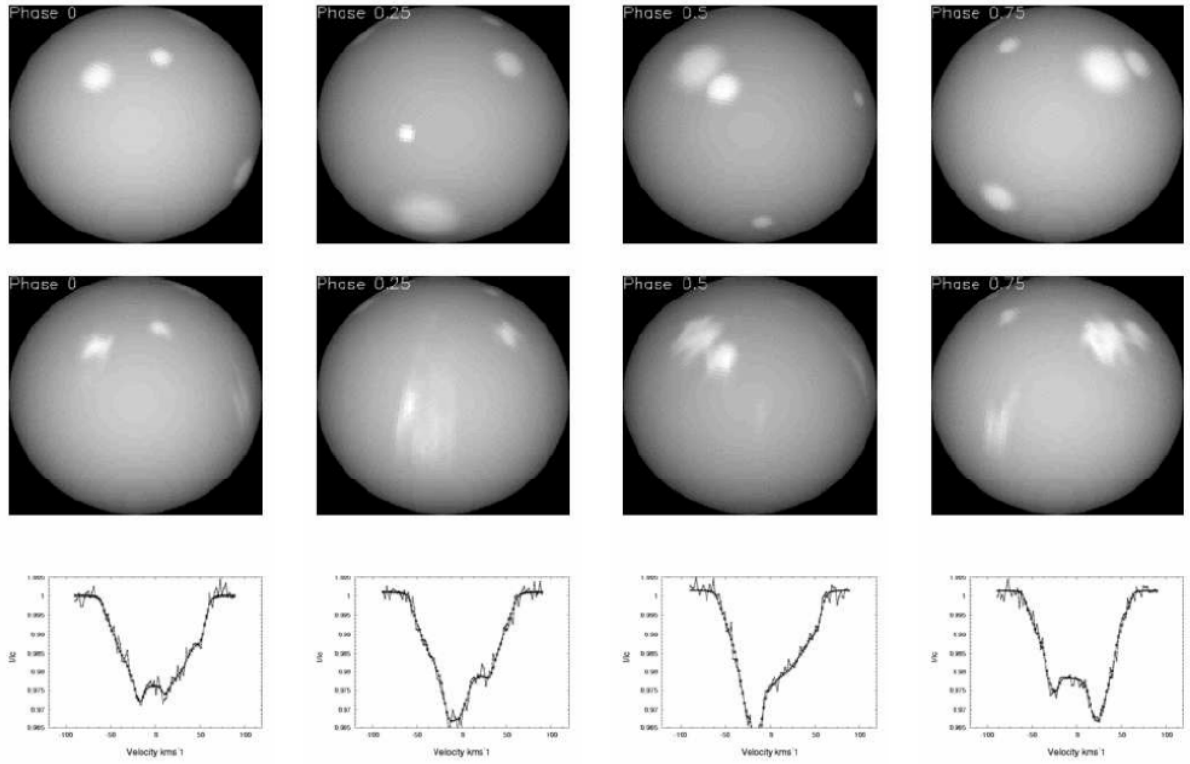

Figure 6-5 Upper row: **Simulated H-band images of weather patterns in an L dwarf with a dusty atmosphere having T_{eff} = 1,900K, and clear patches with T_{eff} = 2,100K. Models supplied by P. Hauschild (priv. comm.) show that average absorption-line strengths of all species are enhanced by a factor ~4 in the clear patches, which cover 3.5% of the stellar surface and yield a 0.015-mag photometric modulation at H.** Lower row**: The resulting rotationally broadened profiles generated with the St Andrews Doppler tomography code have v sin i = 60 km s^{-1} and S/N = 1,000. They show clearly that the rotation profiles are strongly distorted by the clear patches in the cloud deck, but the equivalent width remains roughly constant.** Middle row**: The image reconstructed from the synthetic data recovers the locations and sizes of the clear patches reliably in the hemisphere facing the observer.**

6.11.6 Technical feasibility and instrument requirements:

The Doppler imaging technique relies on having large numbers of spectral features which are broadened primarily by the rotational Doppler effect. The surface resolution attainable on the stellar surface is determined by the ratio of the width of the rotation profile to the intrinsic line

width convolved with the instrumental profile. Basri & Mohanty (2002) used the models of Allard et al. (2000) to find that turbulent velocities in the photospheres of M and L dwarfs drop from 20 m s^{-1} at 3,000K to 2.5 m s^{-1} at 1,500K. The core widths of intermediate-strength absorption lines of most atomic and molecular species are thus of order 2 km s^{-1} FWHM at T_{eff} = 3,000K. At a resolving power R=70,000, PRVS will thus be able to resolve most of the spectral information in a non-rotating star. The spectra of these objects are densely packed with atomic and molecular lines throughout the Y, J and H windows. Over a wavelength range $\Delta\lambda$ centred on wavelength λ, the maximum number of resolvable features is of order $R\Delta\lambda/\lambda$. Over the Y, J and H bands we can thus resolve many thousands of distinct molecular and atomic spectral features. Using lists of known transitions and the least-squares de-convolution method of Donati et al. (1997), we can recover a composite rotation profile whose S/N is of order 0.3 $N^{1/2}$ times the mean S/N in the spectral region observed. In order to avoid excessive rotational blurring during the exposure, we require that the exposure time be less than 10 percent of the rotation period. The brightest field L dwarfs typically have J~11, v sin i = 20 km/s and P_{rot} = 4 hr. Taking a typical case, we thus require S/N > 50 at J~11 in a 15-min exposure. This is however somewhat beyond CRIRES. For example, one of the brightest known L dwarfs is 2MASSW J0036159+182110 (L3, vsini=40km/s). The current CRIRES S/N calculator gives S/N = 6 (J=12.44) or S/N = 7 (H=11.58) in 300s at a resolution of 50,000. Based on its essential sensitivity figures PRVS would be approximately a factor of 2 faster along with 20 times greater spectral coverage. From models we estimate that PRVS will offer simultaneous sampling of approx 10,000 lines over the Y, J and H bands. Using deconvolution techniques gives a S/N boost of $\sim 0.3\sqrt{10000}$ and we obtain S/N > 1000 with deconvolution. While the discovery of brighter objects, primarily with UKIDSS and PannStarrs will probably enable this project to be attempted before the advent of PRVS such studies are unlikely to be conclusive or allow any sampling of stars with a variety of spectral characteristics.

References:

Allard F. et al., 2001, ApJ, 556, 357
Bailer-Jones C.A.L., Mundt R., 1999, A&A, 348, 800
Bailer-Jones C.A.L., Mundt R., 2001, A&A, 374, 1071
Barnes J., 2003, PhD thesis, University of St. Andrews
Basri G., Marcy G.W., 1995, AJ, 109, 762
Briggs K.R., Pye J.P., 2004, MNRAS, 353, 673
Burgasser A.J. et al., 2000, AJ 120, 473
Burgasser A.J. et al. 2002, ApJ, 564, 421
Burrows A., Volobuyev M., 2003, ApJ, 583, 985
Clarke F.J. et al., 2002a, MNRAS, 332, 361
Clarke F.J. et al., 2002b, MNRAS, 335, 1158
Clarke F.J. et al., 2003, MNRAS, 341, 239
Donati J.-F. et al., 1997, MNRAS, 291, 658
Durney B.R. et al., 1993, Solar Physics, 145, 207
Fleming T.A. et al., 2000, ApJ, 533, 372
Gizis J.E. et al., 2000, AJ, 120, 1085
Golimowski D.A. et al., 2004, AJ, 127, 3516
Gorlova N.I. et al., 2003, ApJ, 593, 1074
Hinkle et al., 2003, AAS 35, 126
Jones H.R.A. et al., 2005, AN, 326, 920
Kirkpatrick J.D. et al., 1999, ApJ, 519, 834

Lodders K., 2002, ApJ, 577, 974
Lyubchik Y., 2004, A&A, 416, 655
Marley M.S. et al., 2002, ApJ, 568, 335
McGovern M.R. et al., 2004, ApJ, 600, 1020
Mohanty S. et al., 2004, ApJ, 609, 854
Hambaryan V. et al., 2004, A&A, 415, 265
Liebert J. et al., 2003, AJ, 125, 343
Martin E.L., Ardila D.R., 2001, AJ, 121, 2758
Martin E.L. et al., 2001, ApJ, 557, 822
Mohanty S. et al., 2002, ApJ, 571, 469
Mohanty S., Basri G., 2003, ApJ, 583, 451
Rutledge R.E. et al., 2000, ApJ, 538, 141
Schmitt J.H.M.M., Liefke C., 2002, A&A, 382, 9
Scholz A., Eisloffel J., 2004a, A&A, 419, 249
Scholz A., Eisloffel J., 2004b, A&A, 421, 259
Stelzer B., 2004, ApJ, 615, L153
Smith V.V. et al., 2003, ApJ, 599, L107

6.12 JETS AND ACCRETION ONTO YOUNG STELLAR OBJECTS

Herbig Haro shocks in jets and outflows from Young Stellar Objects show many prominent near-infrared lines, including FeII, FeI, H_2, SII, CI, and NI. The example shown below illustrates the rich H, J and Y bands at low resolution from such an object.

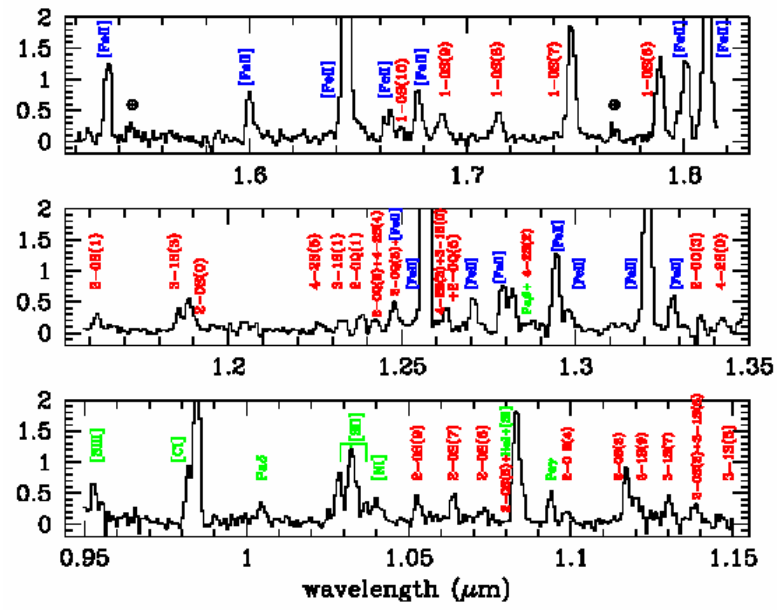

Figure 6-6 NIR spectrum of outflow jet (from Nisini et al., 2002, A&A, 395, 1035)

One important and bright species is [FeII] (marked in blue), where many lines can be detected simultaneously with PRVS. FeII shows a completely different type or region of jet shocks when compared with infrared H_2 lines. Line ratios have been used to measure extinction, excitation and electron densities in the shocks; furthermore the 4km/s velocity resolution and simultaneous wide coverage means PRVS can obtain A_v, T_{ex} and n_e *as a function of velocity*, something which has

not been explored to date. This will give important information about the physics and geometry of these fast dissociative shocks.

Two other lines seen in accreting YSOs are HeI at 1.083μm (one of the brightest HeI lines) and Paβ at 1.282μm. Indications are that these arise in the magnetospheric accretion columns leading onto the stellar surface; however, accretion is notoriously time-variable, and therefore simultaneous spectral profiles of such different species would help considerably in the diagnosis of YSO accretion.

6.13 MAGNETIC FIELDS ON STARS

Magnetic fields play a fundamental role in stellar physics across the entire Hertzsprung-Russell (HR) diagram. They have been invoked to explain phenomena such as non-thermal radio emission in O-B stars (e.g., Rauw et al. 2002}) and jets in young stellar objects (e.g., Goodson et al. 1999); they are responsible for activity in the sun and in late-type stars (e.g., Montesinos et al. 2001}), and can reach huge strengths in degenerate stars (e.g., Liebert et al. 2003). Despite the importance of stellar magnetic fields, it often proves rather difficult to obtain a *direct* measure of their strength. The most commonly employed method for that purpose is based on the Zeeman effect, whereby the $(2J + 1)$-fold degeneracy of the fine structure levels of the various spectroscopic terms is lifted by a magnetic field. This results in the splitting of lines into their Zeeman components and the polarisation of these components. Therefore, spectropolarimetric observations of a line can, in principle, yield an estimate of the magnetic field strength and its direction. However, the circular polarisation signal, characteristic of the σ Zeeman components of a split line, and the linear polarisation signal, characteristic of the π components, both depend strongly on the magnetic field direction, and can cancel to a large degree when fields change sign and orientation on small spatial scales. Sunspots are an example of magnetic structures whose polarimetric signal is barely detectable in the integrated light over the visible hemisphere. As a result, with just a few exceptions, only the large scale magnetic fields of Magnetic Chemically Peculiar stars have been measured by means of spectropolarimetry (e.g., Babcock 1958).

Zeeman *splitting* of a line, on the other hand, provides the most direct method for the detection and measurement of stellar magnetic fields and displays little sensitivity to the mean field orientation. The average wavelength displacement of the σ components from the central line position λ_0 (in Angstroms) is given by $\Delta\lambda = 4.67 \times 10^{-13} g_{\rm eff} \lambda_0^2 B$, where $g_{\rm eff}$ is the effective Lande factor and B is the magnetic field strength expressed in Gauss. From this relation it is clear that it is not always possible to measure stellar magnetic field strengths from optical spectra. For example, at λ = 5000Å and with B = 10 kG, the displacement of the σ component in a simple Zeeman triplet ($g_{\rm eff}$ = 1.0) is 0.12 Å, a value comparable to line broadening due to a rotational velocity of $v_e \sin i \sim$ 7km/s. Lines with more 'favourable' Zeeman patterns (i.e, with larger effective Lande factors and with π and σ components respectively tightly grouped together) can give rise to separations about a factor of 3 larger than the above estimate. Nevertheless, only about fifty Magnetic Chemically Peculiar stars whose projected rotational velocities are sufficiently small and whose magnetic fields are quite strong have been observed with high enough resolution to separate their spectral lines into their Zeeman components (see e.g., Mathys et al. 1997).

Because the displacement of the Zeeman components is proportional to the square of the wavelength, while the non-magnetic line broadening increases only linearly in wavelength,

disentangling magnetic effects from other broadening mechanisms becomes much easier with high resolution spectroscopic observations in the near-infrared, rather than the optical, wavelength region. The first attempt to directly measure the solar magnetic field strength from the Zeeman splitting of a near-infrared line was carried out by Harvey & Hall 1975). They observed the FeI $3d^6 4s5s\,^7D_1$ - $3d^6 4s5p\,^7D_1^o$ 15648.510 Å line in order to take advantage of the large effective Landé factor ($g_{\rm eff}$ = 2.97) for this transition. This line has become a popular target for subsequent investigations of magnetic field strengths, via Zeeman splitting, in studies of the sun and cool stars. A comparison of the sensitivity of diagnostic methods based on observations in the visible, near-infrared, and mid-infrared ranges is given by Solanki (1994). A review of the use of near-infrared observations to estimate stellar magnetic field strengths is given by Saar (1994).

Gondoin et al. (1985) attempted to measure stellar magnetic fields from near-infrared spectral lines, applying Robinson's method (1980) which is based on the comparison between magnetically sensitive and insensitive lines. They found that the accuracy of this method is limited by the presence of blends and suggested that a better estimate of the stellar magnetic field could be obtained by comparing the profiles of magnetically sensitive lines with synthetic profiles. Leone, Vacca & Stift (2003) employed this method to determine the magnetic fields on 3 MCP stars, observed with the CSHELL instrument (R ~ 25000) on the IRTF. Because this program is being carried out on a relatively small telescope, only relatively bright sources have been targeted.

With PRVS on Gemini it will be possible to measure the magnetic field strength on a huge sample of stars. Lower strength fields can be measured in the near-infrared than in the optical. In addition, field strengths on faster rotating stars can be measured from near-infrared spectra relative to optical spectra. As Mathys (2005) has stated, ``high resolution spectroscopy in the infrared is the royal way for future studies of the low end of the magnetic field strength distribution." PRVS on Gemini is poised to lead the way down this road.

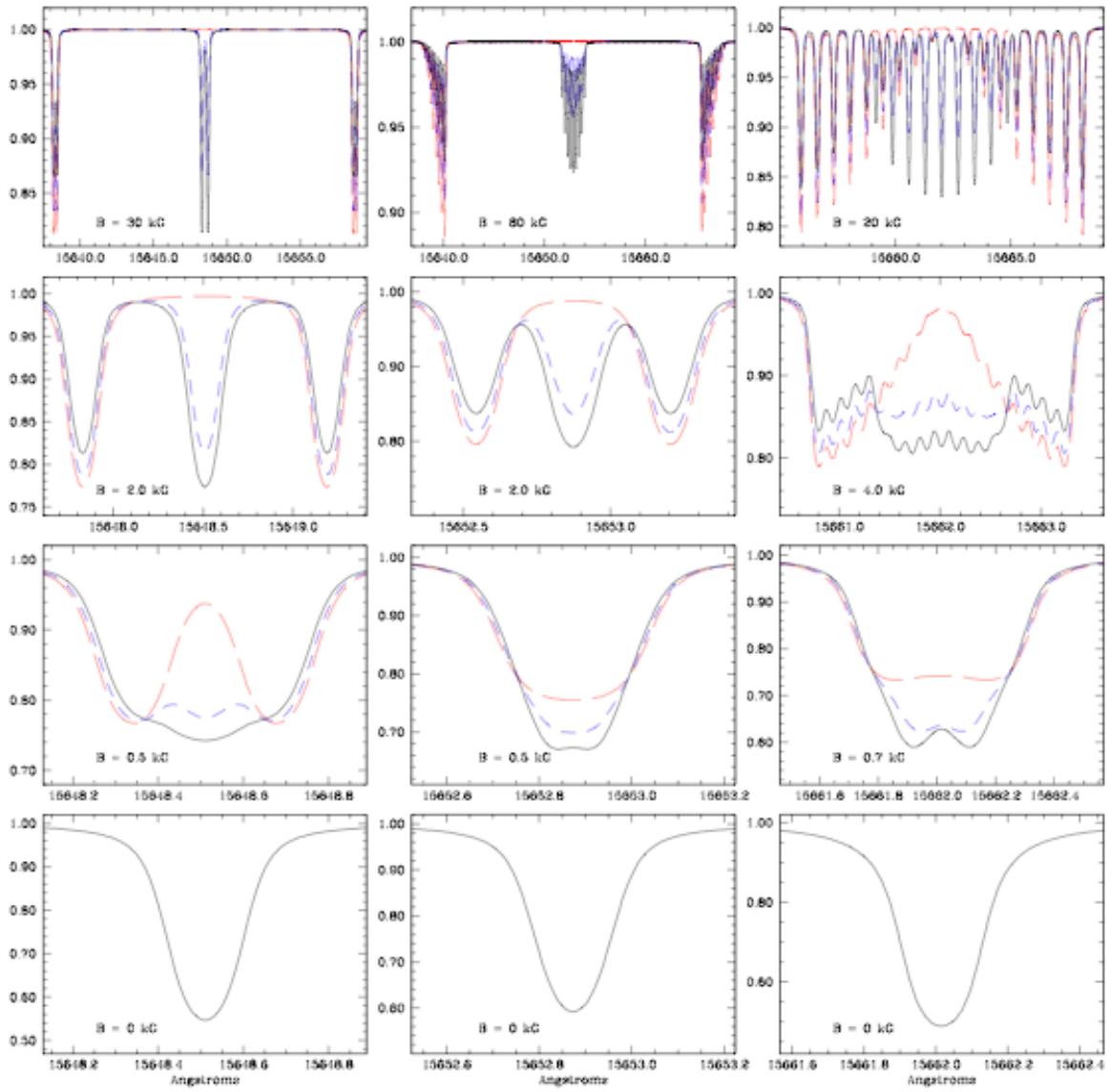

Figure 6-7 From Leone, Vacca & Stift (2003), Left panel: Intensity (Stokes~I) profile of the FeI15648Å line as a function of magnetic field strength. For a few KG field strengths, the line appears to be a simple triplet, but for strongest fields the π and σ components exhibit narrow splitting. Centre panel: The same for the FeI 15653Å line. This line also appears to be a simple Zeeman triplet for relatively weak magnetic fields; otherwise the π and σ components display noticeable splitting. Right panel: The same for the Fe I 15662Å line. As opposed to the other two lines, the overlapping π and σ components never mimic a triplet. Long dashed lines represent a purely longitudinal magnetic field, short dashed lines a 45° inclined field and solid lines a purely transverse field.

6.14 MASSES AND AGES OF NUCLEAR STELLAR CLUSTERS IN NEARBY SPIRAL GALAXIES: SCIENTIFIC JUSTIFICATION

Observations with the Hubble Space Telescope (HST) have revealed that the morphological and photometric properties of the centers of spiral galaxies on 10-100 pc scales are far more complicated than previously assumed (e.g., Carollo, Stiavelli & Mack 1998). While the majority of early-type spirals (S0a--Sab) show smooth bulge-like structures with brightness profiles that follow an $r^{1/4}$ law, almost all late-type spirals (Scd and later) have bulges with exponential brightness profiles, with lower surface brightnesses and densities than their $r^{1/4}$ counterparts. In addition, HST observations of a large sample of spiral galaxies (Carollo et al. 1998; B ker et al. 1999, 2002, 2004) have revealed that a compact, photometrically distinct, nuclear star cluster is almost always present in the center of an exponential bulge.

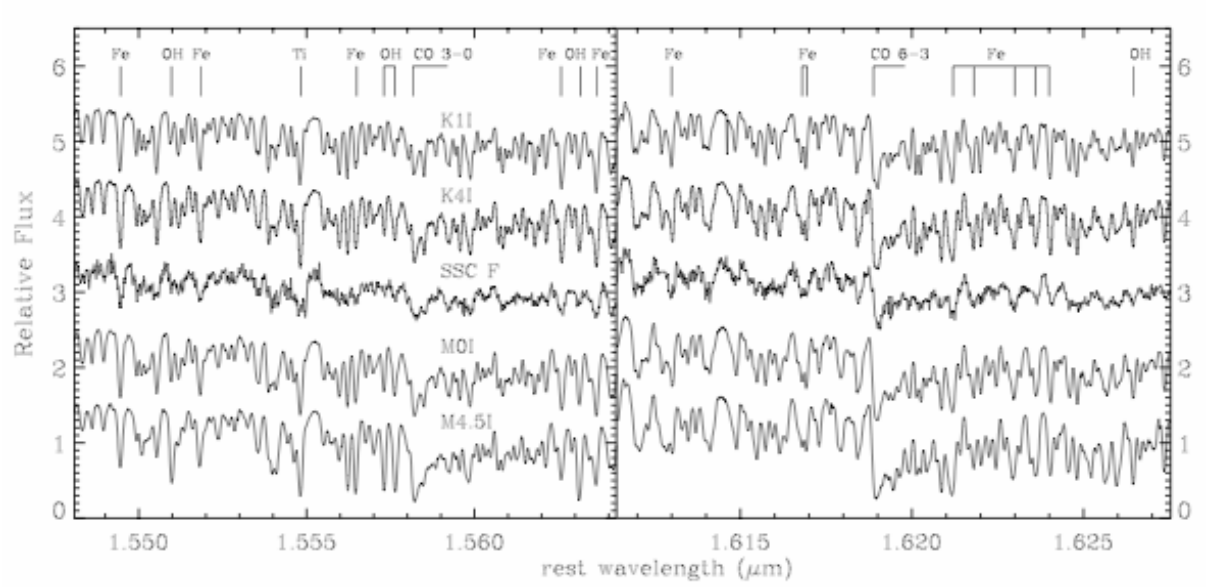

Figure 6-8 Near-IR rest-frame spectra of echelle orders 49 and 47 for M82-F and a range of template supergiants. The spectra are identically normalized, but offset vertically for clarity (zero points are -0.7, 0.3, 1.3, 2.3 and 3.3, from bottom to top). The cluster spectrum closely resembles the supergiant spectra, with the features ``washed out'' by the stellar velocity dispersion (e.g., the CO bandheads at 1.5582 μm and 1.6189 μm) from McCrady et al. (2005).

Nuclear star clusters may play an important role in the secular and morphological evolution of intermediate and late-type spirals, since it has been suggested that sufficiently massive central concentrations of stars (i.e., nuclear clusters) may disrupt the bars that are responsible for gas flow to the center of the galaxy (Merritt & Sellwood 1994; Norman, Sellwood & Hasan 1996). The nuclear clusters themselves were probably formed as a result of gas flowing to the galaxy center under the influence of nuclear bars (Carollo 1999). In this scenario, dynamical effects due to the formation and presence of the massive nuclear cluster shut off any further gas flow into the center of the galaxy and result in the dissolution of the bar via bending instabilities. The process of formation and subsequent dissolution of the bar leads to the creation of a bulge-like stellar distribution at the center of the galaxy (see Norman et al. 1996). Hence, if the stellar cluster is not disrupted by various evolutionary effects, the formation of a nuclear cluster should occur only once during the history of a galaxy. As a consequence, massive nuclear stellar clusters in spiral galaxies should display a large range of ages. Alternatively, if the cluster does not survive, the bar could re-form, leading to further gas infall and the formation of a new nuclear cluster,

which could again disrupt the bar. Such repeated cycles of bar formation, gas infall, nuclear cluster formation, and bar disruption could slowly build the bulge of a spiral galaxy over a Hubble time. In this case, most nuclear stellar clusters would be expected to be fairly young and not very massive. In order to test this model of bulge and cluster formation, it is necessary to determine the mass and age distributions for nuclear clusters in a sample of spirals galaxies.
The most direct method to determine the mass of a stellar cluster is to measure the velocity dispersion of its stars. B ker, van der Marel & Vacca (1999) used the strong CO absorption bandhead at 2.294 μm to estimate the mass of the nuclear cluster in IC 342, a nearby Scd spiral. This strong absorption feature is particularly well suited for the study of the often highly obscured nuclei of galaxies, because near-infrared wavelengths are much less affected by dust extinction than the UV and optical regimes. The same method has been used by Mengel et al. (2002) to determine the masses of super star clusters in The Antennae galaxies. Gilbert & Graham (2000), McCrady et al. (2003, 2005) and McCrady & Graham (2006) have used high resolution H-band spectra to estimate masses of super star clusters in NGC 1569 and M82. When combined with a high spatial resolution surface brightness profile obtained from HST observations, the observed velocity dispersion can be combined with a radius estimate or (for a more sophisticated treatment) modelled (e.g., with the Jeans equations; van der Marel 1994) to yield both the mass M and the mass-to-light ratio M/L of the central cluster. The latter can be used with population synthesis models (e.g., Leitherer et al. 1999) to constrain the age of the cluster. This technique for studying the nature and age of nuclear star clusters is very robust. By contrast, stellar population modelling of low-resolution spectra or broad-band colours is far more uncertain, and does not yield a measurement of the cluster mass.

An example of this analysis technique and its results are shown in Figure 6-8, which presents the CO bandhead spectrum obtained with CSHELL on the IRTF by B ker et al. (1999) for IC 342 as well as spectra of several late-type stellar templates. The inferred cluster velocity dispersion is σ=33 km/s. Combining this value with the size and brightness profile estimated from an HST V-band image, a K-band image obtained at the IRTF, and dynamical models, yields M/L_K= 0.05 and a mass of M=6x10^6 M_{Sun}. This M/L_K is surprisingly low, and the population synthesis models indicate that the cluster must be very young, ~ 10^7 years old. A similar age was obtained for the nuclear cluster in NGC 4449 by B ker et al. (2001) from an analysis of its optical spectrum.

The young ages for the clusters in IC 342 and NGC 4449 have direct bearing on questions about the nature and frequency of the star formation episodes that create nuclear clusters. The cluster in IC 342 is more luminous than most of those found in most other nearby spirals. If these clusters all have masses similar to that of IC 342, then the median age of several Gyrs is inferred for them. This would support the idea of a single episode of nuclear cluster formation. Alternatively, the fainter clusters could simply be less massive than the one in IC 342, in which case no constraint can be placed on their ages. However, the brightness distribution of these clusters may already provide an indication that the incidence of young clusters is higher than expected from the single formation episode scenario (see B ker et al, 1999b).

A direct determination of the age and mass distributions of the nuclear clusters in a large sample of spirals is required to determine whether or not the formation of nuclear clusters in spiral galaxies is a recurring phenomenon, what effect these clusters have on their environment, and how, if at all, these clusters are related to the secular evolution of the exponential bulges in which they reside. With PRVS on Gemini, we can obtain high spectral resolution data for a sample of

nuclear clusters for which there is existing HST observations (which provide high spatial resolution images in order to accurately estimate the size, e.g., B ker et al. 2004)) in order to measure their velocity dispersions and thereby address these issues. The continuing work carried out by McCrady & Graham (2006, in preparation), using NIRSPEC (R=20000) on Keck, demonstrates that accurate velocity dispersion measurements can be derived from H band spectra of stellar clusters. With the extended spectral grasp of PRVS and the higher resolving power, we expect to be able to measure highly accurate velocity dispersions for even the smallest known nuclear clusters.

References

B ker T., et al. 1999a, ApJS, 124, 95
B ker T., van der Marel R. P. & Vacca W. D. 1999b, AJ, 118, 831
B ker T., et al. 2001, AJ, 121, 1473
B ker T., et al. 2002, AJ, 123, 1389
B ker T., et al. 2004, AJ, 127, 105
Carollo C. M., Stiavelli M. & Mack J. 1998, AJ, 116, 68
Carollo M. 1999, ApJ, 523, 566
Gilbert A. & Graham J. 2000, Near-IR Spectroscopy and Population Synthesis of Super Star Clusters in NGC 1569, in Proceedings of Starburst Galaxies: Near & Far, Ringberg Castle, Germany, 10-15 Sept.
Leitherer C. et al. 1999, ApJS, 123, 3
McCrady N., Graham, J. & Gilbert A. 2003, ApJ, 596, 240
McCrady, N., Graham, J. R., & Vacca, W. D. 2005, ApJ, 621, 278
Mengel S., et al., 2002, A&A, 383, 137
Merritt D., Sellwood J. A. 1994, ApJ, 425, 551
Norman C. A., Sellwood J. A., & Hasan H. 1996, ApJ, 462, 114
van der Marel R. P. 1994, MNRAS, 270, 271

6.15 COSMOLOGY

A fundamental goal of modern cosmology is to map out the ionization history of the Universe and identify the sources that, over the first billion years of cosmic time, drove the cosmic reionization. Recent progress in this field has led to a tantalizing state of affairs. On the one hand, the Ly-alpha absorption troughs in SDSS quasars suggest a late end to reionization at z~6 (Fan et al. 2002). On the other hand, WMAP results imply z~11 (Spergel et al. 2006); although this has been reduced from an earlier estimate of z~15 (Bennett et al. 2003), the apparent conflict between the two lines of evidence remains.

Yet the investigation of reionization using quasars and the cosmic microwave background, as an enterprise, is more or less complete. The space density of quasars drops dramatically past z~4, and indeed, beyond a certain maximum redshift we expect there to be no quasars at all. At the same time, while Planck will undoubtedly improve on the Thompson optical-depth measurement of WMAP, it fundamentally cannot contribute more than this single data-point to the debate.

Progress in this area thus requires the ability to measure the optical depth in neutral hydrogen to objects at a range of redshifts z>6. Precisely this challenge – the mapping of neutral hydrogen during the cosmic age prior to reionization – is now motivating the construction of multiple billion-dollar low-frequency radio observatories (LOFAR, the Mileura Widefield Array, the Square Kilometer Array, and others), which will carry out ever more-ambitious searches for highly-redshifted 21 cm emission and absorption features in the decades to come.

Observations of bright gamma-ray burst afterglows with PRVS offer an alternate solution to this problem. The extreme brightness of GRBs makes them beacons from the very high-redshift universe, and with the launch and successful commissioning of NASA's Swift satellite, the promise of detecting GRBs from this epoch has finally been realized. GRB 050904 at z=6.3 (Haislip et al. 2006; Kawai et al. 2006; Fig 6-3) was detected by Swift and localized to few-arcsecond precision within minutes via the satellite's autonomous response procedure, which repoints the satellite and collects and analyzes simultaneous imaging data using co-aligned X-ray and optical/UV telescopes.

As with the SDSS quasars, absorption by neutral hydrogen in the high-redshift IGM extinguished all optical light from the afterglow of GRB 050904 (that is, light with wavelengths bluer than Ly-alpha in the GRB rest frame), while allowing the bright NIR afterglow to shine through. At 1 hour after the burst, with J~16.5 mag, it was bright enough for us to identify it as high-redshift on the basis of its very red J-z colour (Haislip et al. 2006); at 3.4 days after the burst it remained bright enough for low-resolution spectroscopy with Subaru's FOCAS instrument, which provided the redshift measurement (Kawai et al. 2006) and enabled the first attempt to measure the optical depth in IGM neutral hydrogen $\tau_{HI,IGM}$ to a z>6 GRB (Totani et al. 2006). The fact that these observations did not lead to a useful constraint on $\tau_{HI,IGM}$ can probably be attributed to at least three factors: (1) The relatively late response, which greatly reduced the signal-to-noise of the spectrum (compared to the optimum, 0.4 days after the burst); (2) The relatively low redshift of the event, just beyond the end of the reionization epoch as seen from the SDSS quasar sample, which reduced the strength of the IGM signature; and (3) The relatively strong absorption by neutral hydrogen in the GRB host galaxy, which (in the most likely interpretation) accounts for the great majority of Ly-alpha absorption seen in the spectrum (Figure 6-9).

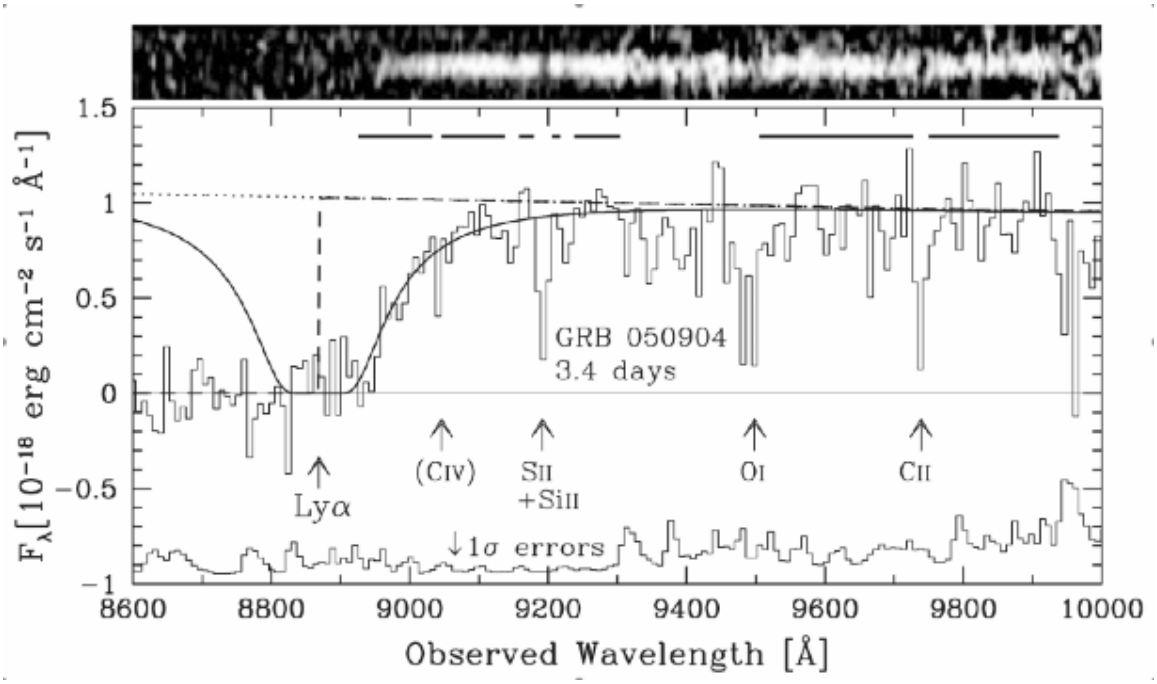

Figure 6-9 Subaru FOCAS spectrum of GRB 050904 at z=6.29 (Kawai et al. 2006), taken 3.4 days after the burst when the afterglow brightness was J=21.5 mag. At one hour after the burst the afterglow was more than 100 times brighter; at earlier times it was likely brighter still. Although a damped Ly-alpha feature is resolved, modelling suggests that it is due to neutral hydrogen in the GRB host galaxy, which overwhelms the signal from the (as yet only partly) neutral z=6.3 IGM. Metal absorption features from the GRB host galaxy are also seen. From Totani et al. (2006).

The PRVS will not be the only instrument to be applied to the study of high-redshift GRBs as these are identified. However, among all NIR spectrographs, PRVS offers a unique combination of wavelength coverage and high spectral resolution. The broad wavelength coverage is a clear advantage for GRB studies, where the exact redshift of the event is not known a priori, and coverage of a particular spectral regime – near and around the Ly-alpha transition at the GRB redshift – is critical to extracting the optimum science. Moreover, the wavelengths covered by PRVS are exactly those that are most interesting for probing the epoch of reionization - covering the gap in our knowledge from the Ly-alpha transition at z=7, just beyond the reach of published quasar studies, to z~12, the point at which (according to WMAP) the IGM is unperturbed and fully neutral.

The high spectral resolution of PRVS is also a significant asset, even though it comes at the cost of decreased sensitivity by comparison to lower-resolution instruments. We have recently published the first analysis of a Keck HIRES spectrum of a GRB afterglow (Penprase et al. 2006), which demonstrates in dramatic fashion the benefits of high resolution in the analysis of GRB afterglows. In this burst, HIRES resolves two absorption systems in the host galaxy – one high equivalent-width, low-velocity system and one low equivalent-width system with a broader velocity profile. The result is that the hypothetical analysis of a lower-resolution spectrum of this afterglow would give incorrect results for the curve of growth and thus, the element abundances in the host (Prochaska 2006). High resolution is thus desirable – perhaps even necessary – if we are interested in understanding the environments of star formation at these redshifts. And although such resolution is not required for the analysis of damped Ly-alpha absorption from the

host galaxy and IGM (which are by definition broad features, resolved in almost any spectra), it will be useful in searching for metal absorption features due to the high-redshift IGM (e.g., Oh 2002) – a potentially unique diagnostic of metal enrichment processes in the early Universe. Finally, high resolution is useful in isolating and hence minimizing the effects of bright emission lines in the NIR.

Technical Case:
GRBs are being detected by Swift at a rate of two per week. The fraction of these events that are occurring at high redshift is still uncertain, with the best estimate suggesting that 5% of Swift events (~5 per year) are at z>5 (Jakobsson et al. 2006). The Swift instruments have no consumables and the satellite orbit is stable, so that the mission is likely to operate well past 2010, allowing it to overlap with PRVS operations.

For our purposes we suggest that a S/N of 10 per resolution element will be sufficient in high-resolution mode, implying limiting magnitudes for a two-hour integration of J=18 mag and H=17.5 mag. As demonstrated by GRB 050904, these limits can certainly be achieved for GRBs from z>6; however, the afterglow flux distribution of high-redshift GRBs as a population is unknown. As a reasonable estimate, we suggest that perhaps 1 in 4 or one event per year will be observable with PRVS (to these magnitude limits) on the first night after the burst.

Each such GRB that is observed by PRVS will provide an additional constraint on the reionization history of the Universe, approximately as valuable in our understanding of this process as the current constraints derived from the SDSS quasars and WMAP. Obtaining these measurements over a range of redshifts, $7 < z < 12$, will map out the ionization history of the universe in full, addressing such critical questions as whether reionization was an extended process, whether quasars were likely to have played a significant role, and whether reionization happened not once but twice, thanks to an early and transient reionization by Pop III stars (Cen 2003).

References:

Bennett C. L., et al., 2003, ApJS, 148, 1
Cen, R., 2003, ApJ, 591, 12
Fan, X., et al., 2002, AJ, 123, 1247
Haislip, J., et al., 2006, Nature, 440, 181
Jakobsson, P., et al., 2006, A&A, 447, 897
Kawai, N., et al., 2006, Nature, 440, 184
Oh, S. P., 2002, MNRAS, 336, 1021
Penprase, B., et al., 2006, ApJ, 646, 358
Prochaska, J., 2006, ApJ in press, astro-ph/0606500
Spergel, D., et al., 2006, ApJ submitted, astro-ph/0603449
Totani, T., et al., 2006, PASJ, 58, 485

7. ISSUES RELATING TO THE PRECISION OF RADIAL VELOCITY MEASUREMENTS

Here we consider the general requirements to achieve 1-m/s RMS radial velocity. These include investigation of the effects of vibration and flexure on the SRF as well as skewness of the resulting Spectral Response Function (SRF) and its importance for data reduction. Even the ultra-stable instrument that we propose needs calibration and so we consider the available options: telluric, gas-cell, laser comb and arc line reference.

Our key results are, (1) the position of the centroid of the spot at which monochromatic light comes to a focus anywhere on the detector of PRVS has to be stable to within 0.1 pixel over the period of an observation and (2) a simultaneous arc line reference is the most appropriate calibration methodology.

7.1 REQUIRED MECHANICAL STABILITY OF IMAGES IN THE FOCAL PLANE

The light arriving at the focal plane of PRVS is spread out by virtue of a number of optical effects. Even monochromatic light does not focus on a Euclidean point but is spread over a small area, partly because the focus is an image of the slit (which has a finite width), partly because of optical aberrations and partly because of diffraction. The present design of PRVS is such that the width of this spot is expected to be roughly that of 2.5 pixels on the detector. If only these optical effects were acting, the function describing the distribution of this light, the 'spectral response function' or optical SRF, would be constant in time and so the distribution of monochromatic light in the pixels would also be constant. In practice, certain effects are expected to move the focal position about during an observation, smearing the image into an effective SRF that is broader than the optical SRF and causing problems in deriving the stellar radial velocity to the required accuracy. The first of these effects is mechanical flexure, the second is thermal flexure and the third is mechanical vibration.

Changes in the effective SRF from one observation to the next diminish the precision with which radial velocity variations of the target star may be measured, and it has previously been found necessary to keep them down to about 1% of the width of the optical SRF for good results in the visible band. Here we discuss the required mechanical stability of the images in the focal plane of PRVS if the new instrument is to be as good as this or better.

The purely optical SRF is taken to be given by a function, $f(x)$, which is fixed in time, where x is a coordinate along the dispersion direction. It is supposed that some mechanical influence causes the position of the centroid of this function not to remain constant at $x = 0$, but to drift during the observation. At some time, t , the centroid is taken to lie at $x = \xi(t)$ and the distribution of light on the detector is $f(x - \xi(t))$. If it is supposed that the fraction of the observing period during which the centroid lies between ξ and $\xi + \mathrm{d}\xi$ is $g(\xi)\mathrm{d}\xi$, then a small contribution of $f(x - \xi)g(\xi)\mathrm{d}\xi$ is made to the distribution of light over the detector in this interval. The effective SRF $h(x)$ over the whole observation is just the integral of this quantity:

$$h(x) = \int_{-\infty}^{\infty} f(x - \xi)g(\xi)\mathrm{d}\xi, \qquad (1)$$

where the integral is termed the convolution of f and g. Here we adopt the shorthand notation $g * f$ for the convolution as defined in Eq. 1. Note that it is commutative: $f * g = g * f$, as may be seen by a simple change of variable in Eq. 1 to $y = x - \xi$.

The mechanical flexure may thus be described by its own function, $g(x)$, as may thermal flexure and mechanical vibration, all of which may be convolved together to give the effective SRF. Here we investigate the properties of the convolution of functions, and in particular how the width of the convolution is related to the widths of the functions convolved. In this way, limits may be set on the functions, g , etc., in order that they not broaden the optical SRF by more than some prescribed amount.

The most general way to do this means is to apply the 'convolution theorem': given two functions of the same variable, $f(x)$ and $g(x)$, and a third function, $h(x)$, defined as the convolution of the first two, where

$$h \equiv f * g = \int_{-\infty}^{+\infty} f(u)g(x-u)du\,, \tag{2}$$

then there is a simple relationship between the Fourier transforms $\tilde{f}(k), \tilde{g}(k)$ and $\tilde{h}(k)$ of these functions, where e.g.

$$\tilde{f}(k) = \int_{-\infty}^{+\infty} f(x)\mathrm{e}^{-2\pi ikx}dx. \tag{3}$$

The theorem is proved in many textbooks (an outline sketch is given later in this section) and states that

$$\tilde{h} = \tilde{f}\ \tilde{g}. \tag{4}$$

Here, we use the theorem for a particular purpose: if the widths of the functions involved are defined in a certain way then the theorem permits the derivation of a particularly simple relationship between those widths. The appropriate definition is related to the second moment of the function and is identical to the standard deviation used in statistics. The relevant width, w_f, of f is defined as

$$w_f \equiv \sqrt{< x^2 >_f} \tag{5}$$

where $< x^2 >_f$ is the mean-square width defined by

$$< x^2 >_f = \frac{\int_{-\infty}^{+\infty} x^2 f(x)dx}{\int_{-\infty}^{+\infty} f(x)dx}.is6; \tag{6}$$

In this equation, it is assumed that the origin of x lies at the centroid of the function $f(x)$, so that

$$\int_{-\infty}^{+\infty} xf(x)dx = 0 \tag{7}$$

and similarly for g and h; this is no limitation in practice because when defining f and g, the origin of the independent variable may always be shifted to make it true.

The choice of this definition of the width, rather than for example the full width to half maximum or the equivalent width, lies in the direct connection between the moment integral and

the Fourier transform. This connection is described in textbooks on Fourier methods (and again, summarised later in this section) and leads directly to the result needed here:

$$w_h^2 = w_f^2 + w_g^2. \tag{8}$$

When two functions, f and g, are convolved together, the width of the resulting function, h, is not given by the sum of the widths of f and g but by the root-sum-of-squares of their widths. This quadrature sum is not unfamiliar: when two independent random variables are added the probability distribution of the sum is given by the convolution of the probability distributions of the individual variables, and so the standard deviation of the sum is the quadrature sum of the standard deviations of the components. This is the underlying reason why we calculate the root-sum-of-squares when combining all the factors that contribute to the error in a measurement.

7.1.1 Flexure

In calculating the broadening effect of mechanical distortion of the spectrograph on the SRF in the focal plane, we take f to be the optical SRF, determined purely by the slit width, diffraction, aberrations, etc. of the optical system, and g to be the mechanical SRF resulting from drift of the centroid of the focal spot due to gravitational and thermal flexure. It is convenient to rewrite Eq. 8 in the form

$$w_h = w_f \left[1 + \left(\frac{w_g}{w_f} \right)^2 \right]^{\frac{1}{2}} \tag{9}$$

and to suppose that the width of the mechanical SRF is so much smaller than that of the optical SRF, $w_g << w_f$, that the square root may be approximated by the first two terms of the Taylor series expansion giving

$$w_h = w_f \left[1 + \frac{1}{2} \left(\frac{w_g}{w_f} \right)^2 + \ldots \right]. \tag{10}$$

This result is very important for the design of PRVS because there is no linear term on the right-hand side, and the lowest term in the expansion is the squared term. The increase in the width of h is only of second order in the ratio w_g / w_f and is therefore much smaller than it would have been if there was a linear term. Thus, if $w_g = 0.1 w_f$ the increase in the width of h is not of order 10%, but only of order 1%. Better still, the coefficient of the squared term is not particularly large, but is only 0.5, and so the actual increase is only of order 0.5% in the above example.

This result is not entirely intuitive, and so to demonstrate its correctness a concrete example is taken here which can be solved exactly. The optical SRF is taken to be a Gaussian of unit FWHM

$$f(x) = \mathrm{e}^{-(4 \ln 2) x^2} \tag{11}$$

whilst the mechanical SRF is a 'top-hat' function of FWHM W_g

$$g(x) = \begin{cases} 1 & \text{if } |x| \le W_g/2 \\ 0 & \text{otherwise.} \end{cases} \quad (12)$$

This mechanical SRF is appropriate to the case in which the line centre drifts at a steady rate across the face of the detector during an observation of fixed duration. The convolution of f and g is readily calculated analytically and is

$$h(x) = \frac{1}{4}\sqrt{\frac{\pi}{\ln 2}}\left[\operatorname{erf}\{\sqrt{\ln 2}(2x+W_g)\} - \operatorname{erf}\{\sqrt{\ln 2}(2x-W_g)\}\right] \quad (13)$$

where erf() is the 'error function' defined as

$$\operatorname{erf}(z) = \frac{2}{\sqrt{\pi}}\int_{-\infty}^{z} e^{-\zeta^2}\,d\zeta. \quad (14)$$

Given any value for W_g, it is straightforward to apply a numerical root-finding algorithm to find W_h, the FWHM of h, and a plot of $(W_h - 1)$ against W_g is given as the points in **Figure 7-1** $(W_h - 1)$ is chosen rather than W_h itself because it is the increase in width caused by the convolution, and it may be seen that the dependence on W_g is not linear. The solid curve is a quadratic fit with no linear term

$$W_h - 1 = cW_g^2 \quad (15)$$

where $c = 0.232$; it passes through the points accurately, confirming that the broadening goes as W_g^2 and not as W_g.

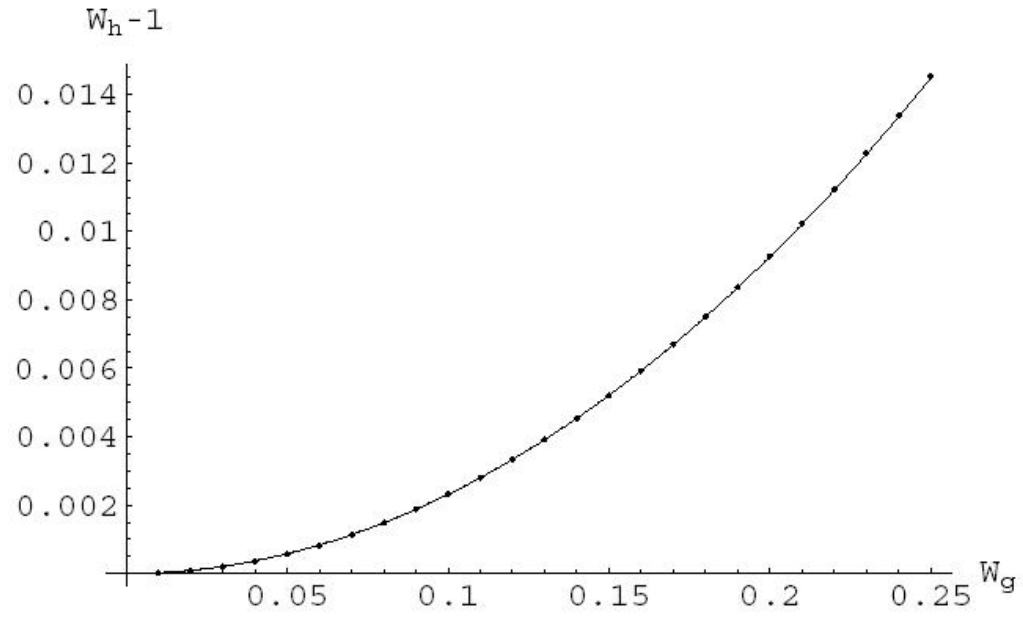

Figure 7-1: The dependence of the FWHM, W_h, of the convolved SRF on the corresponding width, W_g, of the mechanical SRF when the optical SRF has the form of a Gaussian of unit FWHM and the mechanical SRF has the form of a top hat. The points are the calculated values and the curve is a simple quadratic fit.

It is possible to use the quadratic fit to solve for the value of W_g which increases the width of h by 1%: this value is $W_g = \sqrt{0.01/c} = \sqrt{0.01/0.232} = 0.21$. The required tolerance in this case

is therefore about one-fifth of the optical SRF, or about 0.4 pixels if the width of the SRF is 2 pixels, as it may be.

Some caution is needed, however, in taking this result too strictly because the actual SRFs may not be the Gaussian and top hat adopted here, in which case the appropriate value of c would be somewhat different. This does not affect the order of magnitude of the result, however, and it is safe to conclude in general that the mechanical stability required to achieve a convolved SRF that varies by less than 1% is of order a tenth of the width of the optical SRF and not, as it might at first seem, a hundredth.

This result is based on our adoption of 1% for the required stability of the convolved SRF. This was adopted because it is the precision achieved in previous instruments with which planets have successfully been discovered, but it is possible that we shall have to do better since we are searching for planets of terrestrial mass. If 0.1% precision is needed then the width of the mechanical SRF must be no more than one thirtieth of the width of the optical SRF, or about 0.1 pixel, and so it is suggested here that this is the sort of mechanical stability PRVS should aim for over the duration of an exposure (of the order of a few minutes).

Thermal drifts affect the precision in much the same way as mechanical flexure, and so they too should be kept down to about 0.1 pixel. The case of vibration is different, however, and is now treated separately.

7.1.2 Vibration

It is to be expected that the vibrations that might affect PRVS will come principally from closed-cycle coolers, mainly the cooler on the PRVS cryostat. This type of vibration is mechanical but differs from the types discussed in the previous section in two important ways: first it may be taken not to cause a systematic drift of the centroid of the optical SRF over time, and second it is intermittent, being present for some fraction of the cooler cycle and absent for the rest. The corresponding mechanical SRF may be approximated in consequence as

$$g(x) = \lambda C(x) + (1-\lambda)\delta(x) \tag{16}$$

where $C(x)$ is the SRF that would result if the operation of the cooler were not intermittent but instead put out the maximum vibrations continuously, $\delta(x)$ is the delta function and λ is the fraction of the cooler cycle in which the strong vibrations are emitted, $0 \le \lambda \le 1$. $C(x)$ is taken to be standardised in the same way as $\delta(x)$, with unit area and with the centroid at $x = 0$, and to have RMS. width w_C.

Multiplying by x^2 and integrating gives

$$w_g^2 = \lambda w_C^2, \tag{17}$$

since the delta function has no width, and so

$$w_g = \sqrt{\lambda}\, w_C. \tag{18}$$

This may again be contrasted with the result to be expected if the widths were erroneously taken to add directly rather than as the root-sum-of-squares, which would be $w_g = \lambda w_C$; the correct

result is greater than would be expected on this latter formula because $\sqrt{\lambda} \geq \lambda$ for λ in the range given above, which contrasts with the case for gravitational flexure in which the result is smaller.

It is nevertheless possible to derive a simple upper limit on w_g for this case because $\sqrt{\lambda} \leq 1$, so

$$w_g \leq w_C \tag{19}$$

and the width of the SRF of a cooler acting intermittently is never greater than the width of the same cooler acting continuously. This, coupled with the estimates above of how much broadening of the optical SRF is tolerable, leads to the conclusion that w_C should be kept to no more than 0.1 pixel.

This latter limit is probably stricter than it need be, not only because the value of λ is expected to be smaller than unity but also because the SRF g is likely to be fairly reproducible from one observation to the next. This contrasts with the SRF corresponding to mechanical flexure or thermal drift, which might easily be very narrow for one observation but broad for the next, depending on the way in which the centroid of the optical SRF wanders, and so the variation in the width of g could be as large as the entire width of g. The case of vibration is different because there is by definition no systematic drift of the centroid of the SRF attributed to the vibrations from the cooler. The function g is determined as an average over something of the order of 100 cycles of the cooler per observation and so is likely to be relatively invariant from one observation to the next, and it is only the differences in g that are important for the experiment. If it appears difficult to keep the width of the vibrational g down to about 0.1 pixel it would be worthwhile carrying this investigation further to find out how far the specification could be safely relaxed, but until such time it is simpler to leave it at this value.

7.1.3 Conclusions

In order to keep the combined SRF stable enough for Doppler measurements at the precision required for PRVS, it is suggested that the widths of the SRFs corresponding to mechanical flexure, thermal flexure and vibration be kept at no more than about 0.1 pixel each.

Mathematical results required

A function h is defined as the convolution of f and g, and its Fourier transform $\tilde{h}$ is defined as

$$\tilde{h}(k) = \int_{-\infty}^{+\infty} \left[\int_{-\infty}^{+\infty} f(u)g(x-u)du \right] \mathrm{e}^{-2\pi ikx} dx. \tag{20}$$

Changing the order of integration gives

$$\tilde{h}(k) = \int_{-\infty}^{+\infty} f(u) \left[\int_{-\infty}^{+\infty} g(x-u)\mathrm{e}^{-2\pi ikx} dx \right] du \tag{21}$$

and the quantity in square brackets on the right hand side may be simplified by changing the independent variable from x to $v = x - u$ giving

$$[...] = \int_{-\infty}^{+\infty} g(v)\mathrm{e}^{-2\pi ik(u+v)} dv$$

$$= \mathrm{e}^{-2\pi iku} \int_{-\infty}^{+\infty} g(v)\mathrm{e}^{-2\pi ik(u+v)} dv$$
$$= \tilde{g}(k)\mathrm{e}^{-2\pi iku}. \quad (22)$$

Putting this back into Eq. 21 gives

$$\tilde{h}(k) = \int_{-\infty}^{+\infty} f(u)\mathrm{e}^{-2\pi iku} \ \tilde{g}(k) du$$
$$= \int_{-\infty}^{+\infty} f(u)\mathrm{e}^{-2\pi iku} du \ \ \tilde{g}(k)$$
$$= \tilde{f}(k)\, \tilde{g}(k) \quad (23)$$

which proves the convolution theorem.

There is a simple relationship between the definition of the n^{th} moment of a function and the behaviour of its Fourier transform near the origin. To see this, put $k = 0$ in Eq. 2 to get

$$\tilde{f}(0) = \int_{-\infty}^{+\infty} f(x) dx. \quad (24)$$

The right-hand side is the zeroth moment of f and this equation shows it to be identical to the value of the Fourier transform $\tilde{f}$ at the origin. The higher moments can be evaluated in the same way by successive differentiation of Eq. 2 by k, so the first differential

$$\frac{\mathrm{d}\tilde{f}(k)}{\mathrm{d}k} = -2\pi i \int_{-\infty}^{+\infty} x f(x)\mathrm{e}^{-2\pi ikx} dx \quad (25)$$

with $k = 0$ yields the first moment

$$\int_{-\infty}^{+\infty} x f(x) dx = -\frac{1}{2\pi i} \frac{\mathrm{d}\tilde{f}(0)}{\mathrm{d}k}. \quad (26)$$

The process may be repeated to yield any moment. We need the second, so differentiating Eq. 25 once more gives

$$\frac{\mathrm{d}^2 \tilde{f}(k)}{\mathrm{d}k^2} = (-2\pi i)^2 \int_{-\infty}^{+\infty} x^2 f(x)\mathrm{e}^{-2\pi ikx} dx \quad (27)$$

and so the second moment is given by

$$\int_{-\infty}^{+\infty} x^2 f(x) dx = -\frac{1}{(2\pi)^2} \frac{\mathrm{d}^2 \tilde{f}(0)}{\mathrm{d}k^2}. \quad (28)$$

Enough is now in place for the width of the convolution h to be calculated:

$$w_h^2 = \frac{\int_{-\infty}^{+\infty} x^2 h(x) dx}{\int_{-\infty}^{+\infty} h(x) dx} = -\frac{\left(\frac{\mathrm{d}}{\mathrm{d}k}\right)^2 \tilde{h}(0)}{(2\pi)^2 \tilde{h}(0)} = -\frac{\left(\frac{\mathrm{d}}{\mathrm{d}k}\right)^2 \left[\tilde{f}(k)\tilde{g}(k)\right]_{k=0}}{(2\pi)^2 \tilde{f}(0)\tilde{g}(0)} = -\frac{\left[\tilde{f}''\tilde{g} + 2\tilde{f}'\tilde{g}' + \tilde{f}\tilde{g}''\right]_{k=0}}{(2\pi)^2 \tilde{f}(0)\tilde{g}(0)}.$$

But

$$\tilde{f}'(0) = \tilde{g}'(0) = 0 \quad (29)$$

because the first moments of f and g are zero, given the choice of origin of x, so

$$w_h^2 = -\frac{\left[\tilde{f}''\tilde{g}+\tilde{f}\tilde{g}''\right]_{k=0}}{(2\pi)^2\,\tilde{f}(0)\tilde{g}(0)}$$
$$= -\frac{\tilde{f}''(0)}{(2\pi)^2\,\tilde{f}(0)} - \frac{\tilde{g}''(0)}{(2\pi)^2\,\tilde{g}(0)}$$

and finally

$$w_h^2 = w_f^2 + w_g^2. \tag{30}$$

7.2 VELOCITY MEASUREMENTS OF SPECTRAL LINES

Measuring the position of spectral lines on the detector of PRVS cannot be carried out with infinite precision as a result of various types of measurement error, and so the question arises just how accurately can it be measured. This question is addressed here by calculating the accuracy with which the radial velocity of a single, isolated line may be measured, which may trivially be extended to the combined sensitivity to the stellar radial velocity from the measurement of a spectrum containing any number of lines.

7.2.1 Sensitivity

The sensitivity with which the velocity of a given line may be measured depends on the instrument and on the intensity and width of the line. Here, we calculate the sensitivity in the ideal case, in which the spectrometer is completely rigid and free from all spurious and undesirable effects. Sensitivity is then governed by a fundamental, unavoidable feature of the observing process, namely photon noise.

7.2.2 The simplest case

The case is first discussed of an isolated line with the simplest possible profile and then extended to the more general case. This line has a profile in the shape of a top hat, with a centre that is completely opaque and edges that are infinitely steep Figure 7-2a).

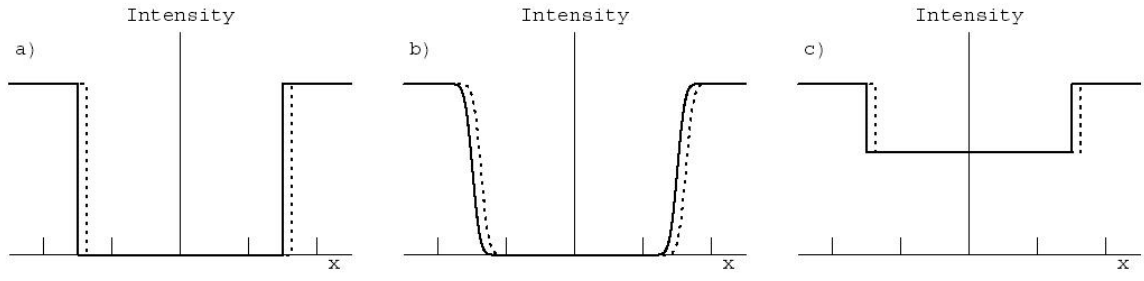

Figure 7-2 The spectrum of an absorption line as a function of velocity. In each panel the intensity of the light is plotted against x, a coordinate on the face of the detector along the dispersion direction. The vertical ticks on the horizontal axis indicate pixel boundaries. The solid line in each case is the absorption supposing the velocity of the absorber to be zero, while for the dotted line the velocity takes the small value v. In a) the profile is opaque at the centre and has infinitely steep sides. In b) it has sides with a more general profile while in c) the line centre is not opaque.

It is supposed that the width of each pixel in the detector is ΔV km s^{-1} and that if there were no absorption features the continuum would fill the well in every pixel with N_0 counts, taken as constant from pixel to pixel. As the velocity v of the line varies so that the edge of the line sweeps across one pixel, the velocity changes by ΔV and the expected number of counts N changes from 0 to N_0, so the velocity is given by

$$v = \Delta V \frac{N}{N_0} + const \tag{1}$$

where the constant is determined by the position of the origin of the velocity scale. The factors on the right-hand side of this equation are known except for N, and it is by measuring N that v is determined. As a result it is δN, the measurement uncertainty in N, that determines δv, the uncertainty in v, through the relationship derived by differentiating Eq. 1:

$$\delta v = \Delta V \frac{\delta N}{N_0}. \tag{2}$$

N is the expectation or average value of the number of counts: in any particular exposure the value is subjected to a statistical uncertainty caused by the random rate of arrival of photons and the standard deviation δN is given by the square root of the average number of counts N

$$\delta N = \sqrt{N} \tag{3}$$

which carries through into an uncertainty in the derived velocity of

$$\delta v = \Delta V \frac{\sqrt{N}}{N_0}. \tag{4}$$

The value of N depends on where the edge of the line falls within the pixel and is on average $N_0/2$ for the present case in which the line centre is opaque, so finally

$$\delta v = \frac{\Delta V}{\sqrt{2N_0}} \tag{5}$$

is the RMS. accuracy with which the velocity of one edge of the line can be determined in a single exposure. The other side of the line falls within a different pixel and an independent estimate of the velocity may be determined from the counts in that pixel, the only difference being that N will decrease with V rather than increasing. This estimate has the same RMS. precision as the other and taking the average of the two estimates as usual as being better than either gives an RMS. precision for the velocity determination of

$$\delta v = \frac{\Delta V}{2\sqrt{N_0}} \tag{6}$$

which is a factor of $\sqrt{2}$ better than either estimate alone. With the current design values for PRVS of $\Delta V = 2$ km s^{-1} and $N_0 = 10^5$ counts per pixel this gives an RMS. precision per measurement of about 3.5 m s^{-1} per line of this type. The smallness of this value compared with the velocity width of each pixel is the pleasant surprise that makes it possible to measure very small velocities with a spectrometer whose resolving power and pixel spacing seem at first sight to be far too coarse for the purpose.

7.2.3 The effect of the line profile

The vertical edges to the line profile adopted in the previous section are not realistic, and any real gas will have lines with a profile that changes more gradually (Figure 7-2b). If the profile of the line across the detector is $\phi(x)$ when the absorber is at zero velocity it will be $\phi(x-v)$ when the velocity is v. Supposing the line to be narrow enough and the velocity small enough that the profile goes from opaque at one edge of a pixel (where $x=a$) to transparent at the other ($x=b$), so that $\phi(a-v)=0$ and $\phi(b-v)=1$. The count in the pixel will be

$$N(v) = N_0 \int_a^b \phi(x-v)\mathrm{d}x. \tag{7}$$

The dependence of this count on v may be obtained by differentiating with respect to v within the integral

$$\begin{aligned}\frac{\mathrm{d}N(v)}{\mathrm{d}v} &= -N_0 \int_a^b \phi'(x-v)\mathrm{d}x \\ &= -N_0\left[\phi(x-v)\right]_a^b \\ &= -N_0\end{aligned} \tag{8}$$

which is independent of ϕ. The differentiation of ϕ followed by integration over the finite range leaves the result depending only on the opacity in the core of the line and outside the line profile, which does not depend on the details of the profile.

Another way of seeing the same result is to imagine a line whose profile on one side is infinitely steep and on the other is arbitrary. This line will absorb a fixed number of counts whatever the value of v, so on changing v the increase in the number of photons reaching the pixels on one side of the line must be exactly matched by the decrease in the number reaching the pixels on the other.

The shape of the profile does not matter, and the results derived in the previous section for one particularly simple line profile are general results that apply to all profiles.

7.2.4 The effect of line intensity

There are other factors that do influence the sensitivity, however, and the most important of these is the central depth of the line. In Figure 7-2c is seen a line with vertical sides but finite depth f, where f gives the fractional reduction in intensity below the continuum: $0 \le f \le 1$. As the edge of the line sweeps across a pixel the counts change from $(1-f)N_0$ to N_0 (rather than from 0 to N_0 as before when the centre was opaque) so Eq. 2 becomes

$$\delta v = \Delta V \frac{\delta N}{f N_0}. \tag{9}$$

The uncertainty δv in v is now greater than before because of the presence of the fraction f in the denominator. The value of δN depends as before on the average number of counts in a pixel partially occluded by the line. It will become apparent below that the case in which the line

is weak ($f << 1$) is of particular importance, in which case $\delta N \approx \sqrt{N_0}$ and the RMS. accuracy of the velocity determination from averaging both edges of the line is

$$\delta v = \frac{\Delta V}{f\sqrt{2N_0}}. \tag{10}$$

For the tentative parameters for PRVS this is

$$\delta v = \frac{4.5}{f} \text{ m/s}. \tag{11}$$

7.2.5 The effect of line width

So far it has been assumed that on each side of the line the opacity goes from its peak to a negligible value within a single pixel, and here this assumption is relaxed and it is supposed that this change is spread over N_p pixels. These pixels may be considered as constituting one big pixel, and the sensitivity may be calculated from Eq. 10 by replacing N_0 by $N_p N_0$ and ΔV by $N_p \Delta V$ giving

$$\delta v = \frac{\Delta V}{f}\sqrt{\frac{N_p}{2N_0}}. \tag{12}$$

7.2.6 Implications for PRVS on the precision of the stellar velocity determination

Once the stellar spectrum is known, whether from observations or from models, the accuracy with which the velocity of any line may be measured is given by the formula above, and it remains only to combine the velocity determinations of the individual lines to provide an average, weighted of course in the usual way as the inverse square of the error estimate. This process is applied to a particular model atmosphere calculation elsewhere in this study.

7.2.7 Emission lines

Emission lines may be treated in a similar way. The simplest case, of a narrow emission line with vertical sides that peaks at N_0 counts per pixel is identical to the case for the corresponding absorption line, because the blue side of the emission line is identical to the red side of the absorption line, and vice-versa. The effect of broadening is also identical, for the same reason.

The case of a weak emission line is different from that of a weak absorption line, however, because the number of counts per pixel is smaller in the absence of any continuum, and this reduces the photon noise. If a narrow emission line with vertical sides has a peak of fN_0 counts, then the number of counts in the pixel containing the red side of the line lies between 0 and fN_0 depending on where the edge falls within the pixel, with an average of $fN_0/2$. The RMS. noise on the counts is thus $\delta N = \sqrt{fN_0/2}$ and so the accuracy with which the velocity may be determined from one edge of the line profile is

$$\delta v = \Delta V \sqrt{\frac{2}{f N_0}} \tag{13}$$

and from both edges

$$\delta v = \Delta V \sqrt{\frac{1}{f N_0}}. \tag{14}$$

The velocity accuracy goes as $f^{-\frac{1}{2}}$ rather than as f^{-1} and so the velocity of a weak emission line can be measured more accurately than that of a weak absorption line with the same value of f. The formula for an entire emission line (both sides), including the effects of finite line-width, is

$$\delta v = \Delta V \sqrt{\frac{N_{\mathrm{p}}}{f N_0}}. \tag{15}$$

It must be emphasized that this result applies only to an isolated emission line and not to one superposed on a continuum; in the latter cases the noise becomes dominated by the photon noise from the continuum and the accuracy is greatly reduced. This is one of the factors underlying our choice of a fibre system in which the emission lines from the arc are not combined with the starlight. The weak lines in the arc spectrum provide much better velocity references in this case, precisely because there is no photon noise from the stellar continuum.

7.3 THE VELOCITY ACCURACY OF THE ARC REFERENCE SYSTEM

The stellar radial velocities are not measured absolutely but relative to the local reference system provided by the arc lamps, which allows compensation for such effects as image drift across the face of the detector during the observation. This system must provide a reference standard of velocity which is at least as good as the 1 m/s that is intended for the stellar measurement, and here we show that the particular system designed for PRVS is more than good enough. The precision with which the position of the centroid of any reference arc line can be determined when observing depends ultimately on the number of photons detected in that line, and so showing the system to be adequate amounts to demonstrating that it can provide enough photons.

The light in any arc line does not arrive at a point on the detector but over a range determined by the Spectral Response Function (SRF). If we take this function in this section to be normalized to unit area along the dispersion direction, like a probability density function, it can in fact be interpreted as a probability density function: one that gives where on the detector the next photon from the arc line is going to be absorbed. That position is an estimate of the position of the centroid of the arc line, plus or minus σ, the standard deviation of the probability function (i.e. the rms width of the SRF in this case). With a large number of photons N, the accuracy of the estimate of the centroid position improves as the square root of N, and so we just need to know the value of N that delivers the centroid position to plus or minus 1 m/s. Our SRF has a width (FWHM) of 5 km/s, and adopting a functional form for the SRF determines σ and hence N. For a Gaussian N=4.5 million photons are required, and for a hyperbolic secant (sech) 7.2 million.

To find out how many photons an arc line can deliver, we first consider the standard case in which the peak of the line is exposed to full-well, for which we adopt a round number of 100,000 photons. The SRF is 2.5 pixels wide FWHM, and so the total number of photons under the SRF, allowing for its extent both along and perpendicular to the dispersion direction, is 750,000.

The flux in one arc line may be augmented in two ways: first by the flux in the other arc lines and second by making multiple exposures of the arc system with destructive readouts while observing the stellar spectrum normally ("superexposures"). There are hundreds of lines in the spectra of our four arc gases, and here we adopt the conservative assumption that the total flux in all these lines amounts to at least 10 times the flux in the brightest. This gives a minimum of 7.5 million photons from all the arc lines added together, which is a little more than the minimum derived above for 1 m/s accuracy. The arc line system used normally (without superexposures) is just good enough to achieve the required precision.

When superexposures are considered, allowing for e.g. a 10-fold increase in the exposure of the arc system, the total number of photons collected becomes 75 million, enough to give 0.3 m/s accuracy. This level is sufficient to provide a reference system for stellar velocities that are themselves good to 1 m/s with negligible degradation of that precision.

7.4 THE EFFECT OF DETECTOR PIXELLATION ON THE SENSITIVITY OF RADIAL-VELOCITY SPECTROMETERS

An arbitrary image $I(x,y)$ is a distribution of light intensity over the surface of a detector as a function of the coordinates x and y on that surface. The image contains all the information available to the detector from the source of the light as delivered by the optical system. The detector absorbs the light and presents to the subsequent electronics and computer a digitized approximation to the image. However good the detector, it will be imperfect in certain regards and the information in the image will suffer a certain amount of degradation. There are many different ways in which this degradation may take place, but here we are concerned only with the effects of pixellation. The surfaces of modern semiconductor detectors are invariably divided into pixels, and the output of the detector is an array of numbers, each one ideally proportional to the number of photons captured in the corresponding pixel during the observation, plus or minus some detector noise.

Pixellation brings with it two consequences: smoothing and aliasing. The smoothing enters because the digital number from each pixel is proportional to the value $< I(x,y) >$ averaged over the area of the pixel rather than to the value of $I(x,y)$ at one Euclidean point. The aliasing is a consequence of the even spacing of the pixels, so that the values $< I(x_i, y_j) >$ are the result of sampling over a discrete set of points on a regularly-spaced grid (x_i, y_j) (where $i, j = 1, 2..N$ for an $N \times N$ array of pixels) rather than over the continuous variables (x,y); this famously results in fine structure in the image (corresponding to spatial wavelengths shorter than twice the separation of grid points) masquerading as large-scale structure (at longer spatial wavelengths).

Here we investigate the effect this degradation in image quality has on the radial-velocity sensitivity of PRVS. It is to be expected that a design with coarse pixels will have poorer sensitivity than one with fine, but it is not known by how much. The issue is particularly important for PRVS because it relates to the cost of the project. Reducing the size of the image of the cross-dispersed spectrum reduces the area of detector required and therefore the cost, but reduces at the same time the width of the spectral-response function (SRF) as measured in units of pixels. It is possible to keep the number of detector chips down to two, instead of the four that would otherwise be required, if the image is reduced to the point at which the width of the SRF is 2.5 pixels. Here we calculate whether this is acceptable. Spectroscopists are often unwilling to design instruments with such a narrow SRF because the loss of spectral detail is unwelcome, but we are not designing a general-purpose spectrograph and detail per se is not relevant; the objective of PRVS is to measure radial velocities, and the important issue is how the velocity sensitivity depends on the coarseness of the pixellation.

7.4.1 Pixellation

The spectrum is effectively one-dimensional and so the only pixellation that is relevant being that along the dispersion direction. The i-th pixel is taken to receive the image of the spectrum between wavelengths λ_i and λ_{i+1}. The spectrum of the light reaching the detector is given by the function $n_\lambda(\lambda)$, whose units are counts per second per unit of wavelength. The expected (i.e. average) number of counts in the i-th pixel after an observation of duration T seconds is therefore N_i where

$$N_i = T\int_{\lambda_i}^{\lambda_{i+1}} n_\lambda(\lambda)\mathrm{d}\lambda. \quad (1)$$

Now consider the case in which the same spectrum is observed but with a small Doppler shift corresponding to a very small velocity v: very small in this context means very small compared with the width of the pixel in velocity units, $v\dfrac{\mathrm{d}\lambda}{\mathrm{d}v} << (\lambda_{i+1} - \lambda_i)$ where $\mathrm{d}\lambda/\mathrm{d}v$ is the Doppler shift. For a positive radial velocity the spectrum shifts to the longward and the pixel now captures light that originated at wavelengths shorter than observed: any light received at a wavelength λ was emitted at $\lambda - v\dfrac{\mathrm{d}\lambda}{\mathrm{d}v}$. This changes the expected number of counts in the i-th pixel to

$$N_i + \delta N_i = T\int_{\lambda_i}^{\lambda_{i+1}} n_\lambda\left(\lambda - v\frac{\mathrm{d}\lambda}{\mathrm{d}v}\right)\mathrm{d}\lambda. \quad (2)$$

This equation is developed by expanding the expression for n_λ as a Taylor series

$$n_\lambda\left(\lambda - v\frac{\mathrm{d}\lambda}{\mathrm{d}v}\right) = n_\lambda(\lambda) - v\frac{\mathrm{d}\lambda}{\mathrm{d}v}\frac{\mathrm{d}n_\lambda(\lambda)}{\mathrm{d}\lambda} \quad (3)$$

from which all the terms in v^2 and higher have been dropped. Substituting this in Eq. (2) and subtracting Eq. (1) gives the change in the expected number of counts brought on by the Doppler shift as

$$\begin{aligned} \delta N_i &= -v\frac{\mathrm{d}\lambda}{\mathrm{d}v} T\int_{\lambda_i}^{\lambda_{i+1}} \frac{\mathrm{d}n_\lambda}{\mathrm{d}\lambda}\mathrm{d}\lambda \\ &= -v\frac{\mathrm{d}\lambda}{\mathrm{d}v} T\left[n_\lambda\right]_{\lambda_i}^{\lambda_{i+1}} \quad (4) \\ &= v\frac{\mathrm{d}\lambda}{\mathrm{d}v} T\left[n_\lambda(\lambda_i) - n_\lambda(\lambda_{i+1})\right]. \end{aligned}$$

This change δN_i in the expected number of counts is the entire contribution of the i-th pixel to the knowledge of the radial velocity v. Inverting the last equation therefore yields an estimate of that velocity which may be combined with similar estimates from all the other pixels to give a grand estimate where w_i is the weight accorded to the i-th measurement. The most suitable weight is the inverse of the variance of each measurement

$$w_i = \frac{1}{\sigma_i^2} \quad (5)$$

where σ_i is the standard deviation of the velocity estimate . σ_i is determined by the noise on the measured counts δN_i, for which we adopt the photon-limited noise model

$$\sigma(\delta N_i) = \sqrt{N_i}. \quad (6)$$

From Eq. (7) the standard deviation of the velocity estimate is then

$$\sigma_i = \frac{\sqrt{N_i}}{\dfrac{\mathrm{d}\lambda}{\mathrm{d}v} T\left[n_\lambda(\lambda_i) - n_\lambda(\lambda_{i+1})\right]} \quad (7)$$

and the standard deviation σ on the grand velocity estimate is given by use of Eq. (7) as

$$\frac{1}{\sigma^2} = \sum_i \frac{1}{\sigma_i^2}$$

$$= T\sum_i \frac{\mathrm{d}\lambda}{\mathrm{d}v}\frac{\left[n_\lambda(\lambda_i)-n_\lambda(\lambda_{i+1})\right]^2}{\int_{\lambda_i}^{\lambda_{i+1}} n_\lambda(\lambda)\mathrm{d}\lambda} \qquad (8)$$

$$= T\frac{\mathrm{d}\lambda}{\mathrm{d}v}\sum_i \frac{\left[n_\lambda(\lambda_i)-n_\lambda(\lambda_{i+1})\right]^2}{\int_{\lambda_i}^{\lambda_{i+1}} n_\lambda(\lambda)\mathrm{d}\lambda}$$

where in the last line we have assumed that the Doppler shift $\frac{\mathrm{d}\lambda}{\mathrm{d}v}$ varies by so little across the spectrum that it can be taken outside the sum.

This last expression contains terms such as T that are not in themselves of interest. They may be removed by renormalizing the expression for σ by dividing it by σ_0, the corresponding expression for the case in which the size of the pixels is taken to be vanishingly small. This is done by taking $\Delta\lambda \to 0$ where $\Delta\lambda = \lambda_{i+1} - \lambda_i$. The terms in the sum in Eq. (7) become

$$\begin{aligned} \left[n_\lambda(\lambda_i)-n_\lambda(\lambda_{i+1})\right]^2 &\to \left[n'_\lambda(\lambda)\Delta\lambda\right]^2 \\ \int_{\lambda_i}^{\lambda_{i+1}} n_\lambda(\lambda)\mathrm{d}\lambda &\to n_\lambda(\lambda)\Delta\lambda \end{aligned} \qquad (9)$$

and so the sum itself becomes

$$\sum_i \frac{\left[n_\lambda(\lambda_i)-n_\lambda(\lambda_{i+1})\right]^2}{\int_{\lambda_i}^{\lambda_{i+1}} n_\lambda(\lambda)\mathrm{d}\lambda} \to \int \frac{\left(n'_\lambda(\lambda)\right)^2}{n_\lambda(\lambda)}\mathrm{d}\lambda \qquad (10)$$

and finally σ_V, defined as σ/σ_0, is given by

$$\sigma_\mathrm{V} = \sqrt{\frac{\int \frac{\left(n'_\lambda(\lambda)\right)^2}{n_\lambda(\lambda)}\mathrm{d}\lambda}{\sum_i \frac{\left(n_\lambda(\lambda_i)-n_\lambda(\lambda_{i+1})\right)^2}{\int_{\lambda_i}^{\lambda_{i+1}} n_\lambda(\lambda)\mathrm{d}\lambda}}}. \qquad (11)$$

Eq. (11) is the desired result. The normalization is such that the exposure time T no longer enters, and neither does the normalization of n_λ. It is to be expected that the value of σ, calculated as it is on the basis of a finite pixel width, will always be greater than that of σ_0 for the infinitessimal pixels, because the latter are expected to lose no information, and so $\sigma_\mathrm{V} \geq 1$, the equality applying only to the limit of small pixel size.

7.4.2 The velocity sensitivity

Various specific cases are now investigated, with different profiles adopted for the spectral-response function and different ratios of the width of the SRF to the pixel size. This is done by choosing the SRF and the pixellation and evaluating Eq. (11) numerically. For a first example

the SRF is taken to be a Gaussian, which for simplicity and without loss of generality is taken to have unit height and unit width (FWHM), and to be centred on a wavelength of λ_0:

$$n_\lambda(\lambda) = \exp\left[-k(\lambda-\lambda_0)^2\right] \qquad (12)$$

where $k = 4\ln 2$. Choosing the pixellation amounts to selecting a value of the pixel width $\Delta\lambda$ and also deciding where λ_0, the centre of the SRF, falls with respect to the detector grid. The results of choosing λ_0 to lie on the boundary between two adjacent pixels are given as the solid curve in Figure 7-3; the calculation was in fact repeated for other choices of siting within a pixel but the value of σ_V is indistinguishable from the plotted curve over the range shown.

The dashed curve in Figure 7-3 is for a double Gaussian, similar to the single Gaussian but with a second component with 0.01 times the amplitude and 10 times the width, to simulate broad, low-level wings. The dotted curve is for the hyperbolic secant, a bell-shaped curve with rather broader wings than the Gaussian

$$sech(x) = \frac{2}{e^x + e^{-x}}. \qquad (13)$$

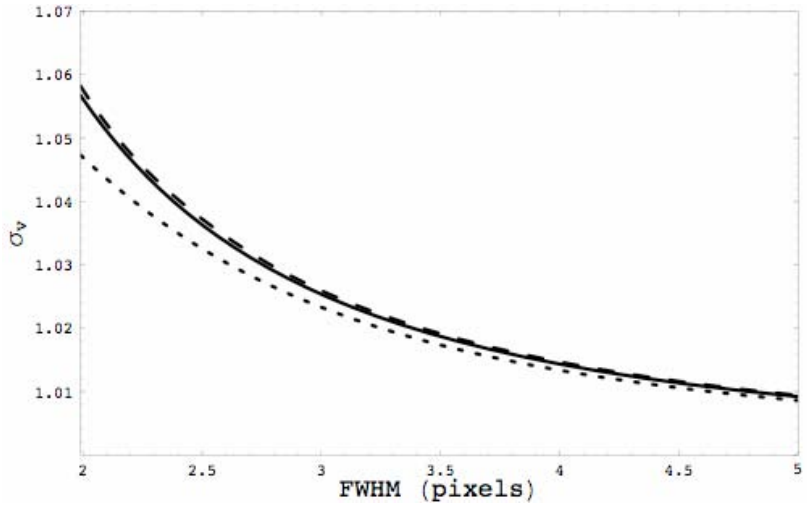

Figure 7-3 The dependence of σ_V on the width of the SRF in pixels. The curve are for different functional forms of the SRF. Solid curve: a simple Gaussian; dashed curve: a double Gaussian (a simple Gaussian with additional broad wings); dotted curve: a hyperbolic secant.

7.4.3 Discussion

There is not much difference between the three curves in Figure 7-3, and it is therefore the general features of the results that are of interest for PRVS. First, σ_V increases steadily from right to left across the figure, as the pixels are made coarser. There is no abrupt increase at any point on the curves, and instead the velocity precision degrades gracefully in all three cases.

Second, the precision does not degrade by much. The absolute increase in the rms error of measurement over the case for vanishingly small pixels is only of the order of a few percent over the entire range plotted for all three curves.

Third, the relative precision in going to 2.5 pixels FWHM from other possible choices for PRVS, such as 3.0 pixels, degrades by even less. The values of σ_V for 2.5 pixels are only about 1%

greater than those for 3, requiring observations of only 2% longer duration to achieve the same accuracy. The extra cost of two more detectors required for the wider SRF is therefore hard to justify.

7.4.4 Conclusions

The loss of radial-velocity precision in reducing the FWHM of the SRF from 3 pixels to 2.5 is slight, and insufficient to form the basis of a case for purchasing 4 detectors for PRVS instead of 2.

7.5 THE EFFECT ON THE VELOCITY MEASUREMENTS OF SKEWNESS OF THE SPECTRAL-RESPONSE FUNCTION

The skewness of the spectrometer spectral-response function (SRF) has to be considered in the design phase of PRVS because if it is not properly controlled it can introduce spurious shifts in the derived velocities of spectral lines. The effect is a rather subtle one: partly because it is small; partly because it depends, not on the skewness of the SRF directly, but on any difference between what the skewness of the SRF actually is and what the observer thinks it is; and partly because the spurious shift in the derived velocity of each stellar line depends on the width of that line. This latter feature means that there could be a spurious and unknown velocity offset between the derived stellar velocity and that of the reference arc lines because the stellar lines will not in general have the same average width as the arc lines. Such an offset is unwelcome, and completely intolerable if it varies with time.

The effect of the skewness is discussed here in two parts. In the first, it is shown how the spurious velocity errors arise in reducing the data from the spectrometer whenever there is a difference between the skewness of the actual SRF of the instrument and that of the SRF adopted in the calculations. In the second it is pointed out that the main cause of such a difference in skewness is likely to be small drifts in the position of the image of the spectrum on the detector over the period of the observation, which change the effective SRF by smearing; limits are set on how much drift of this kind can be tolerated.

7.5.1 The SRF and data reduction

Erroneous velocity shifts arise when there is a difference between the actual spectral-response function (SRF) of the instrument and the SRF adopted when modelling the observation in the process of reducing the data. The former is here called $SRF1(x)$, where x is a variable measuring distance along the dispersion direction, and the latter $SRF2(x)$. $SRF1$ is termed the effective spectral-response function because it includes all contributions to the broadening of the response to a monochromatic signal, such as the width of the slit, the aberrations of the optical system, diffraction and any smearing caused by image motion across the face of the detector during the observation.

The skewness is measured by the third moment of the SRF. The first two moments are defined as

$$m_0 = \int_{-\infty}^{\infty} SRF(x)\mathrm{d}x$$

$$m_1 = \int_{-\infty}^{\infty} xSRF(x)\mathrm{d}x/m_0 \qquad (1)$$

and the higher moments m_n for $n = 2,3,.$ as

$$m_n = \int_{-\infty}^{\infty} (x - m_1)^n \, SRF(x)/m_0 \mathrm{d}x. \qquad (2)$$

It is also useful to define a dimensionless version of the third moment as μ_3 where

$$\mu_3 = \frac{m_3}{\sqrt[3]{m_2^2}}. \qquad (3)$$

The definitions differ in that if a SRF is written in a form in which it is easily scaled to a new width w, i.e. as

$$SRF(x) = \frac{1}{w} f(\frac{x}{w}) \qquad (4)$$

then it is easy to show that m_2 varies as w^2 and m_3 varies as w^3, whereas μ_3 is constant, independent of w.

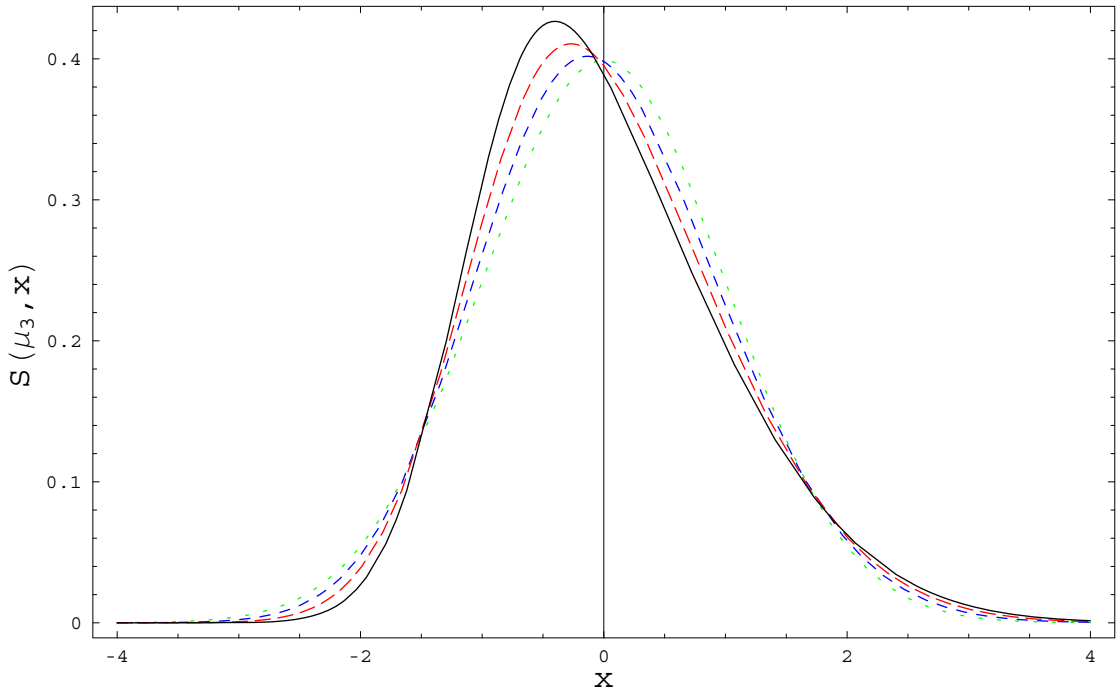

Figure 7-4 Skewed Gaussians. The curves are for $\mu_3 = 0, 0.2, 0.4$ and 0.6 (dotted, medium dashed, long dashed and solid lines respectively).

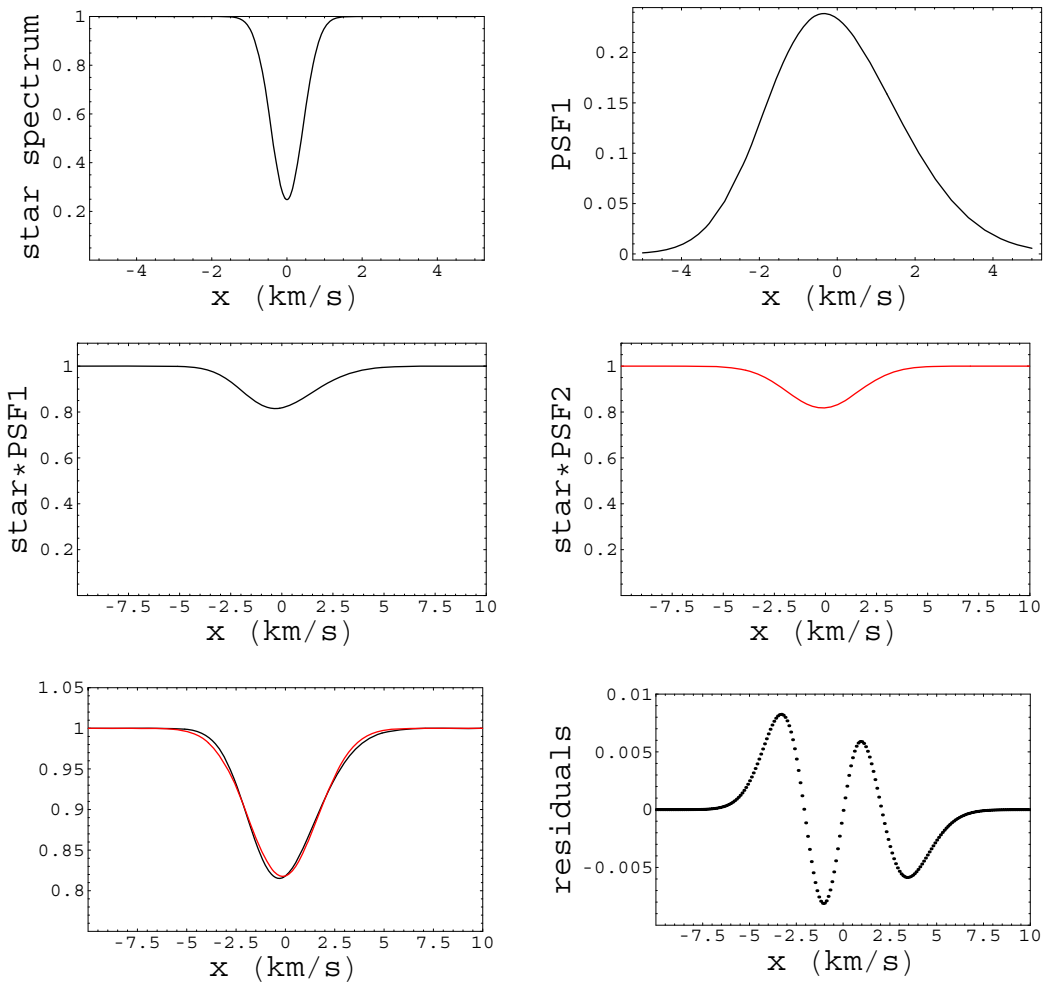

Figure 7-5 The model (note that the axis label PFS1 should read SRF1, and similarly PSF2 SRF2). By panel: 1) Top left: a symmetrical Gaussian absorption line representing a feature in the stellar spectrum. 2) Top right: $SRF1$, a skew Gaussian with FWHM=4 km/s and $\mu_3 = 0.3$. 3) Centre left: the convolution of the first two curves, representing the observed spectrum. 4) Centre right: the convolution of the stellar line with $SRF2$, a symmetrical Gaussian with FWHM=4 km/s and $\mu_3 = 0$, representing the model. 5) Bottom left: the curves in panels 3 and 4 after least-squares fitting the latter to the former. 6) Bottom right: the residuals from panel 5.

The instrumental SRF is expected to be a bell-shaped curve, and in order to model it here it is taken to be a Gaussian modified in a simple way in order to induce any desired amount of skewness. The formula adopted for the skew Gaussian is

$$S(\mu_3, x) = exp[-(x - \kappa\, log(cosh(x)))^2/2] \qquad (5)$$

in which the parameter $\kappa = \kappa(\mu_3)$ governs the skewness. The procedure adopted was to numerically integrate to find the moments of this function for a range of values of κ, which could then be inverse interpolated and rescaled to give a function with unit area, zero mean and any desired values of m_2 and m_3. Skewed Gaussians generated in this way with the same value of m_2 but different values of m_3 are shown in Figure 7-4.

A model was adopted in which a single stellar feature is represented by a deep symmetrical Gaussian absorption line centred on zero velocity (Figure 7-5, panel 1) of FWHM=1 km/s (this

unrealistically small value is necessary to bring out the small differences between the various curves in Figure 7-5, and more realistic values are taken when deriving numerical results below). $SRF1$ is taken to be a skew Gaussian with FWHM=4 km/s and $\mu_3 = 0.3$ (panel 2) and the convolution with the stellar spectrum that represents the observed profile is given in panel 3. The model curve for fitting is identical except that $SRF2$ is an ordinary Gaussian (i.e. has FWHM=4 km/s but $\mu_3 = 0$) giving the convolution in panel 4 that represents the modelled profile. This latter curve was then fitted by a least-squares procedure to that in panel 3, the main variable being the velocity offset between the observed and modelled curves. The best fit is shown in panel 5 and the residuals in panel 6. The key feature is that the model curve had to be shifted by a finite amount (-133 m/s) to provide the best fit: the stellar velocity would have been inferred erroneously from this shift to be -133 m/s and not zero, the true value. The erroneous shift arises because the best fit between curves of different skewness does not occur with the centroids of the two curves superposed but with a small, systematic displacement between them.
The procedure was repeated with a more realistic width for the stellar line (5 km/s FWHM) and with μ_3, the third moment of $SRF1$ variable: the third moment of $SRF2$ was kept at zero. The resulting erroneous shift is plotted in Figure 7-6, where it is seen to have a strong, linear dependence on μ_3.

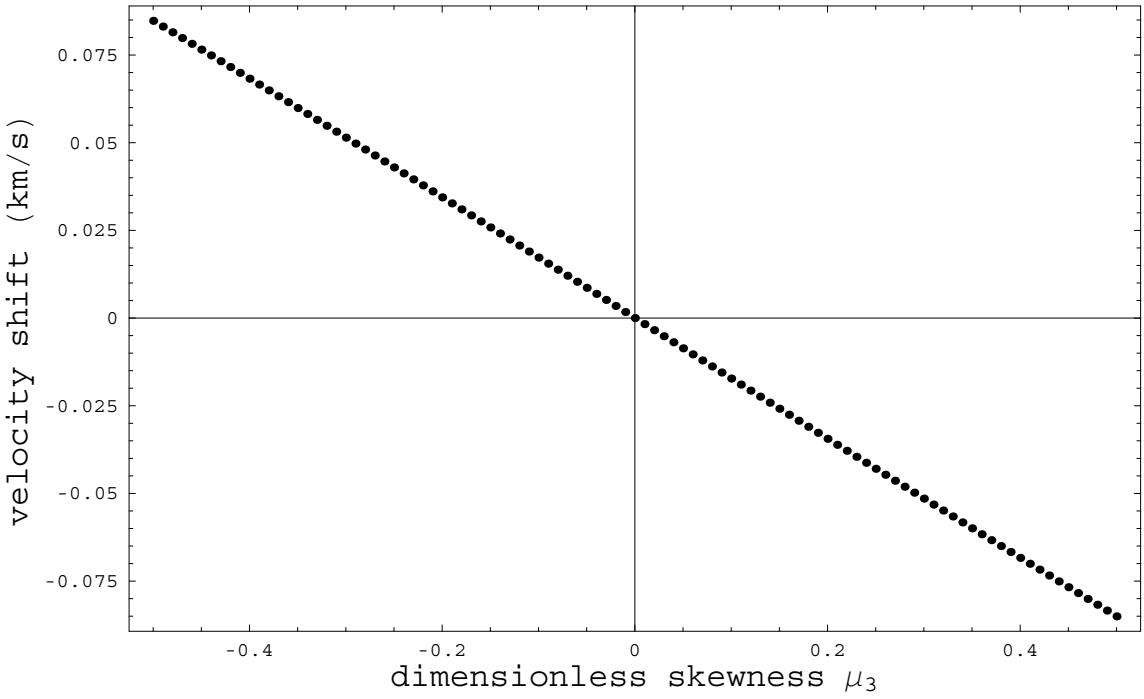

Figure 7-6 The spurious velocity shift when $SRF1$ has skewness μ_3 but $SRF2$ is not skew; for a stellar line of width 5 km/s.

The procedure in the previous paragraph was repeated once more, but this time $SRF2$ was also allowed to have a finite skewness. The skewnesses of $SRF1$ and $SRF2$ were taken as independent samples from a random number generator, and the erroneous shift plotted against the difference

$$\delta\mu_3 = \mu_3(SRF1) - \mu_3(SRF2) \quad (6)$$

in Figure 7-6. There is again a strong linear dependence, with the points defining in fact the same line as in Figure 7-5.

The line in Figure 7-6 passes through the origin. This shows that it is not actually the skewness of the SRF that causes the erroneous shift, because if the two SRFs both have the same, finite skewness the shift is zero. It is instead the observer's ignorance of $SRF1$ that causes the shift, because ideally $SRF2$ should be taken identical to $SRF1$, and it is in any difference in skewness between these functions that the unwelcome shift arises.

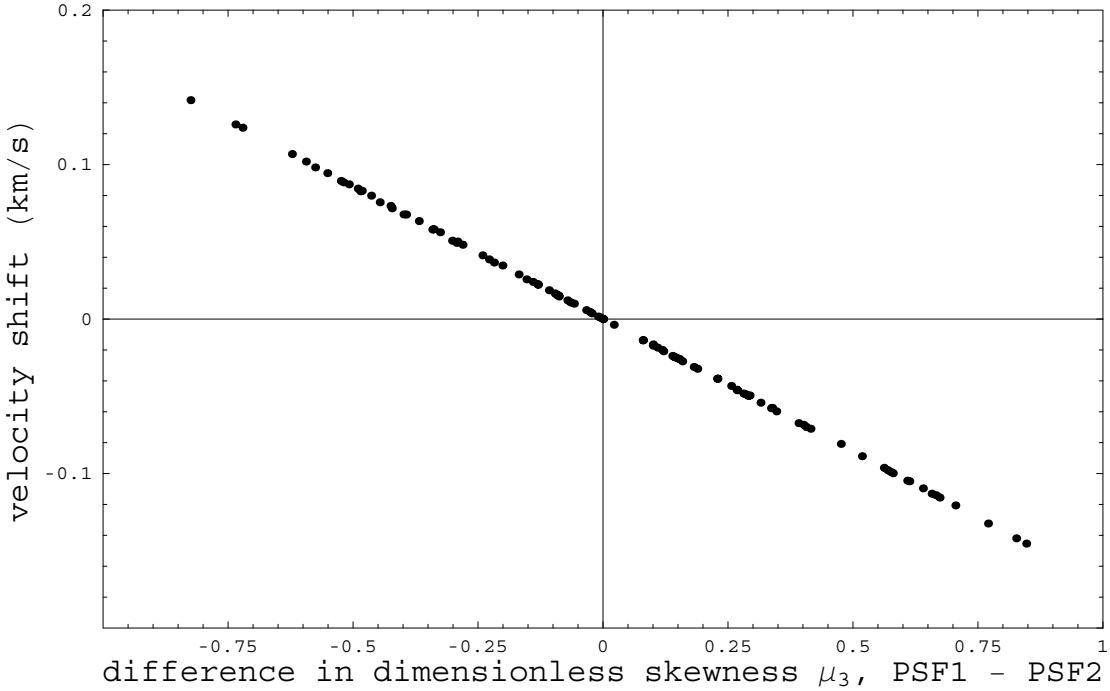

Figure 7-7 The spurious velocity shift as a function of $\delta\mu_3$ for the general case when $SRF1$ and $SRF2$ have different, finite skewness; for a stellar line of width 5 km/s.

7.5.2 The effect of the width of the stellar lines

Even so, this error might not matter too much if it were to affect the stellar spectrum and the reference spectrum identically; they would both be shifted by the same amount and there would be no difference between the origins of their velocity scales. But the problem is that they may not be shifted by the same amount because the extent of the shift depends on the width of the stellar line. In Figure 7-8 the absolute value of the shift is shown as a function of the width of the stellar line when the SRFs both have width 4 km/s (FWHM) and differ in third moment by $\delta\mu_3 = 0.3$. The shift is seen to be greatest for the narrow lines and to decrease monotonically as the line width increases. The average width of the stellar lines will in general differ from the average width of the arc lines, and so this effect will introduce a spurious and highly undesirable zero offset between the velocity scales for the star and the arc reference system. It is this, somewhat subtle, effect that could ruin radial velocity measurements at the desired accuracy if care is not taken to control it. If, for example, the reference lines have an average width of 4 km/s and the stellar lines 6 km/s, the offset would be of order 30 m/s.

The range of offsets in Figure 7-8 is of order 100 m/s, and we require to reduce the offset for PRVS to 1 m/s or smaller. The calculations for Figure 7-8 were performed for the particular choice of parameter $\delta\mu_3 = 0.3$, and since the shifts are proportional to $\delta\mu_3$ (Figure 7-7) the offset may be reduced by reducing the uncertainty in μ_3. For 1 m/s, $\delta\mu_3 \leq 0.003$, while for 0.3

m/s, $\delta\mu_3 \leq 0.001$ is required. We next investigate how to keep μ_3 under control to this accuracy.

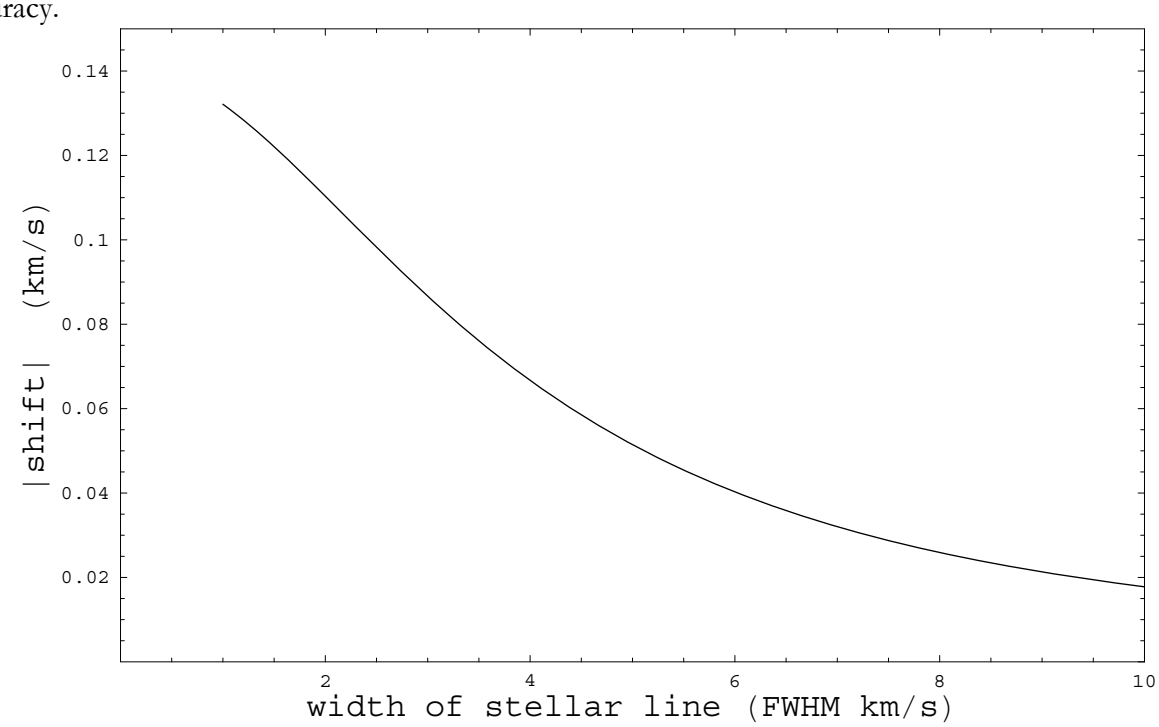

Figure 7-8 The amplitude of the spurious velocity shift as a function of the width of the stellar line.

7.5.3 Implications for the mechanical stability

The effective SRF may be written as the convolution of two functions f and g. f is the optical SRF, defined as the instantaneous SRF of the optical system. It is determined by the aberrations of the optical system, particularly by various orders of coma, and unless the optics are deliberately realigned from time to time it is most unlikely to vary significantly with time, and we assume here that it does not. It will also be very well determined from calibration measurements.

The variability and uncertainty in the effective SRF are attributed entirely to the function g, which describes the wandering of the image over the detector caused by mechanical and thermal flexure. This function is defined as follows. It is supposed some mechanical influence causes the position of the centroid of the function f not to remain constant at $x = 0$ but to drift during the observation. At some time t the centroid is taken to lie at $x = \xi(t)$ where ξ is some function of t, and the distribution of light on the detector is $f(x - \xi(t))$. If it is supposed that the fraction of the observing period during which the centroid lies between ξ and $\xi + d\xi$ is $g(\xi)d\xi$ (defining g) then a small contribution of $f(x-\xi)g(\xi)d\xi$ is made to the distribution of light over the detector in this interval. The effective SRF $SRF1(x)$ over the whole observation is just the integral of this quantity

$$SRF1(x) = \int_{-\infty}^{\infty} f(x-\xi)g(\xi)d\xi \qquad (7)$$

where the integral is termed the convolution of f and g. Here we adopt the shorthand notation $g * f$ for the convolution as defined in Eq. (7) note that it is commutative: $f * g = g * f$, as may be seen by a simple change of variable in Eq. (7) to $y = x - \xi$.

This function g does vary from one observation to the next and its third moment with it, and this is the origin of the variability of the third moment of the effective SRF $SRF1 = f * g$. In order to see how to control its variability, advantage is taken of the earlier results derived from Eq.(4): if the width w of $g(x)$ is kept small enough, the absolute value of its third moment can be no greater than w^3. Any changes in its third moment m_3 may therefore be kept arbitrarily small by keeping w small enough. w is of order the total extent of the drift of the image over the face of the detector during the observation, and so the constraint is effectively on the allowable mechanical and thermal stability of the image.

We first look at the form that $g(x)$ might have. In Figure 7-9, the left panel shows the `top-hat' form for the case in which the image drifts steadily across the detector, which is likely to be a reasonable approximation to the behaviour of the image during most observations. In the right panel we show a very asymmetrical version that might be caused by a strong acceleration of the drift motion, with the image lingering longer at one end of its range than the other; this may be regarded as a fairly extreme case. The skewness of the latter is $\mu_3 = -0.57$, so we have to consider the possibility that $|\delta\mu_3|$ could be as large as unity in a very bad case; more usually we would expect it to be of order 0.1.

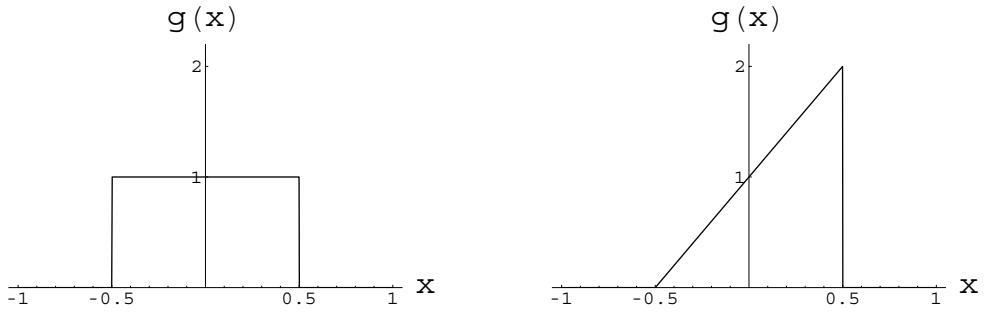

Figure 7-9 Possible forms for the convolving function $g(x)$. Left: for the case in which the image drifts at a constant velocity over the detector. Right: for a case in which the image spends more time near the right-hand end of its range.

We now consider the m_n^*, the various moments of the convolution $f * g$. The second moment of a convolution m_2^* is equal to the sum of the second moments of the two functions that were convolved:

$$m_2^* = m_2 + m_2' \quad (8)$$

where m_2 is the second moment of f and m_2' that of g. m_2 is of order W^2, where W is the width of f. The instrument will certainly be stable enough that any image drift during an observation will be much smaller than the width of the optical SRF, so $w << W$ (where w is the width of g) and $m_2^* \approx W^2$.

The third moment of a convolution m_3^* is equal to the sum of the third moments of the two functions that were convolved:

$$m_3^* = m_3 + m_3'. \quad (9)$$

Without loss of generality we take f to be symmetrical, so $m_3 = 0$ and $m_3^* = m_3'$. The third moment of g may be as large as $|m_3'| \approx w^3$ and so we obtain the final relationship, an expression for the uncertainty in the dimensionless third moment of the effective SRF (i.e. $SRF1$) of

$$|\delta\mu_3^*| \leq \left(\frac{w}{W}\right)^3 . \quad (10)$$

An upper limit to the uncertainty in μ_3^* is therefore given by the cube of the ratio of the widths of g and f. It was established above that to achieve an offset between the stellar and reference velocity scales of no more than 0.3 m/s it is necessary to keep the uncertainty in μ_3^* to less than 0.001, which is achieved by ensuring $w \leq 0.1W$. Since $W = 2.5$ pixels in our design for PRVS, this implies $w \leq 0.25$ pixels. Given the uncertainties in the calculation, which is based for example on the adoption of a Gaussian model for the SRF whereas the real SRF is not yet known, and given also that a small reduction in w brings a large reduction in the offset between the two velocity scales because of the high power in Eq. (10), we have adopted the more conservative $w \leq 0.1$ pixels as the stability requirement on the centroid of the image during an observation. With this limit, $|\delta\mu_3^*| \leq 0.000064$, and the offset in the velocity scales is reduced to roughly 1 -- 2 orders of magnitude too small to influence the accuracy of PRVS. Provided the mechanical stability is this high, we can determine the optical SRF once and for all, and use that as $SRF2$ in the process of data reduction, ignoring the smearing caused by image motion: the difference between the optical SRF and the effective SRF will be too small to influence the accuracy of the derived radial velocities.

7.5.4 General

This limit on w requires high stability for the spectrometer, and is behind the various decisions to build PRVS solidly, in an evacuated vessel, to stabilize the temperature both actively and to have a large mass of cold metal in the instrument in order to make any temperature changes as sluggish as possible. In this we are following the design philosophy of HARPS. In fact, the data reduction pipeline for HARPS uses a fixed, standard SRF for the model fitting, implying that the instrument is indeed as stable as calculated here as required for PRVS in order to make uncertainty in the SRF orders of magnitude too small to influence the accuracy of the zero of velocity for the star. This bodes well for our design for PRVS, since it is deliberately intended to be similar to that of HARPS and to follow the techniques that have provided the high stability of that instrument.

If the instrument is kept very stable, it is not in principle necessary to determine the SRF with great accuracy. If there is a difference between $SRF1$ and $SRF2$, there will be an offset between the stellar and reference velocity scales for any given star. This offset may vary from star to star as the average stellar linewidth varies, but the offset in any one star will not vary with time and so the orbital changes caused by an orbiting planet will still be detectable. In practice, however, it is safer to minimize the offset, and this requires that the SRF be measured accurately. To do this, the arc light system is ideal, providing as it does many lines across the spectrum. By sending this light down the stellar fibres offline (i.e. during the day when not observing) many determinations of the SRF may be made right across the spectrum, and by repeating the process many times, with many different settings of the strength of the light in order to bring different lines of different strength into play, the SRF may be determined with almost arbitrary accuracy. This process is identical to that proposed for calibrating the wavelength scale of the spectrometer, and

so this wavelength scale and the shape of the SRF may be determined at the same time. It is likely that the process will be accurate enough that the anticipated small variations in SRF across the detector brought on by the variation in the aberrations will be detected and measured.
The SRF may also be monitored from the observations. This may be done by varying $SRF2$ when reducing the stellar spectrum to find whether it is possible to reduce the rms difference between the measured and modelled spectra; it may also be done by making similar use of the arc lines in the reference spectrum. In this way any unexpected instrumental problems may reveal themselves, preventing erroneous astronomical inferences being drawn.

7.5.5 Conclusions

1) There is no design requirement on the skewness of the SRF. The SRF should be designed to keep the diameter of the image of monochrome light as small as possible (i.e. to minimize the second moment of the SRF thereby to maximize the spectral resolving power) without concern for the third moment.
2) The third moment must, however, be kept very stable; this may be achieved by building a very solid and stable instrument in order to keep the optical SRF stable, and by ensuring that any drift of the image of the spectrum over the face of the detector be kept to less than 0.1 pixel during the course of any observation (i.e. on timescales from about 1 minute to 1 hour).
3) The optical SRF should be determined as accurately as possible as part of the process of calibrating the instrument. This may be done as a by-product of the calibration of the wavelength scale of the spectrometer using arc light.

7.6 MEASURING THE SKEWNESS OF THE SPECTRAL-RESPONSE FUNCTION

It has been shown that in order to keep constant the relative velocity scales of the starlight and the reference arc light, it is necessary to know the skewness of the spectrometer spectral-response function (SRF) to within 1 part in 1000, as measured by the dimensionless third moment μ_3. The general strategy is to measure the skewness thoroughly once in a while in an offline (daytime) measurement and to keep the spectrometer so stable that the skewness does not change significantly between such measurements. Here is investigated what is necessary to measure the SRF to the required accuracy using the arclines provided by the calibration system.

7.6.1 Measuring the SRF in the face of photon noise

The SRF is parameterized by the third moment and can therefore be written $f(\mu_3, x)$, where x is measured along the dispersion direction. The question to be answered is how easy is it to discern the difference between this SRF and one with a slightly different third moment $f(\mu_3 + \Delta\mu_3, x)$? Any measurement technique will suffer from noise and, when observing the strong signals which we will provide in the calibration process, our detectors are limited by photon noise. The question may thus be recast as how many photons are required for us to be sure that $\Delta\mu_3$ is no greater than 0.001?

The dependence of f on μ_3 is nonlinear and hard to tackle in general, but the Taylor series expansion may be used in order to linearize the problem in our case because $\Delta\mu_3$ is very small. The series is

$$f(\mu_3 + \Delta\mu_3, x) = f(\mu_3, x) + \Delta\mu_3 \frac{\partial f(\mu_3, x)}{\partial \mu_3} + O(\Delta\mu_3^2) \quad (1)$$

and all the terms in the small quantity $\Delta\mu_3$ higher than the first are neglected here, so the expression is linear in that parameter. In order to calculate the photon statistics the distribution of light collected on the detector from a particular arcline during the exposure between x and $x + \mathrm{d}x$ is written $Nf(x)\mathrm{d}x$ where N is the total number of photons collected across the entire profile of the arcline. The notation for the SRF f has been simplified by dropping explicit mention of the dependence on μ_3 and f is taken to be normalized to unit area

$$\int_{-\infty}^{\infty} f(x)\mathrm{d}x = 1. \quad (2)$$

The linearized problem is thus one of fitting the function

$$f(x) + \Delta\mu_3\, g(x) \qquad (30$$

to the measured data, where the notation has been simplified by setting g(x) for $\partial f/\partial\mu_3$. $\Delta\mu_3$ is estimated by first fitting f to the profile of the measured data, subtracting out the corresponding best fit to yield a set of residuals, and finally fitting g to the residuals to give the best estimate of $\Delta\mu_3$. This latter process is a regression of g on the residuals, and the noise σ on $\Delta\mu_3$ may be calculated by standard methods. When the pixels are taken to be arbitrarily small:

$$\sigma^2(\mu_3) = \frac{1}{N\int_{-\infty}^{\infty} g^2(x)/f(x)\mathrm{d}x} \quad (4)$$

which solves the problem of how much information such an observation contains about the skewness μ_3. This equation may be rearranged to give the minimum number of photons required in order to measure the skewness with an accuracy better than some specified value $\sigma(\mu_3)$ as

$$N_{min} = \frac{1}{\sigma^2(\mu_3)\int_{-\infty}^{\infty} g^2(x)/f(x)\mathrm{d}x.} \qquad (5)$$

It has already been decided that the required accuracy is $\sigma(\mu_3) = 0.001$ and so all that remains is to choose a functional form for the SRF f and to evaluate the integral. The SRF is taken to be a Gaussian, with the following formalism for making it as skew as desired

$$f(\mu_3, x) = A\,exp[-(x - \kappa\,log(cosh(x)))^2/2] \quad (6)$$

where κ is a parameter that determines the skewness and A is a normalizing constant to give unit area. The integral then has the value 0.173 and so $N_{min} = 5,800,000$. The photon noise becomes small enough to enable μ_3 to be determined to the required precision if more than about 6 million photons are accumulated in the arc line.

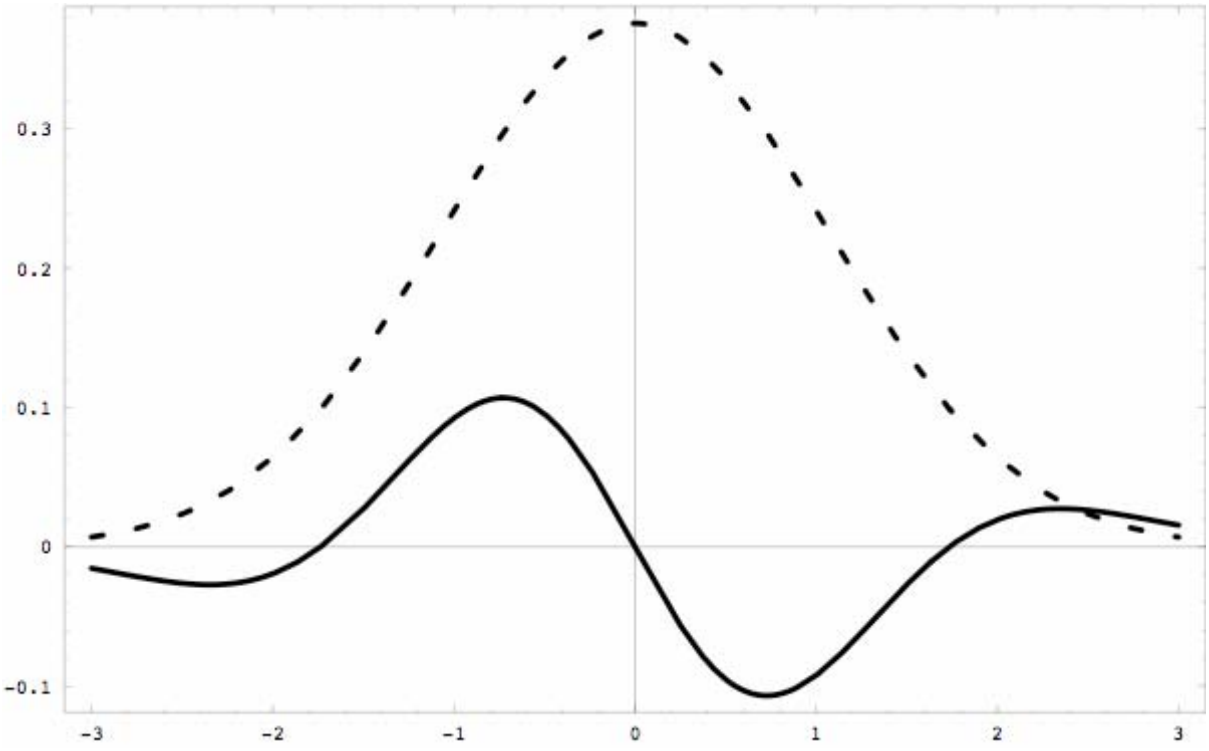

Figure 7-10 A Gaussian SRF of width 2.5 pixels FWHM (dashed curve) and its partial derivative (solid curve).

7.6.2 The effect of pixellation

The above calculation refers to the ideal case in which the pixels are arbitrarily small, and it is to be expected that rather more photons will be required in the real case. In order to gain a first impression how much the pixellation could matter, Figure 7-10Figure 7-10 has been plotted. It shows first the Gaussian SRF f, in a different normalization in which the full width to half maximum is 2.5 horizontal units, so that the horizontal units correspond to pixels on the PRVS detector. Also shown, to the same scale, is the partial derivative with respect to the third moment

$\partial f/\partial\mu_3$. When the pixels are very small the sampled function averaged over bins is very close to the function itself, but as they become coarser the sampled values pixel begin to give only an approximation to the continuous curve. When the pixels are very large, parts of the positive lobes of a function like that of the partial derivative begin to lie in the same pixels as parts of the negative lobes, giving considerable cancellation, so that the measured values do not follow the continuous curve at all fully and the information on the shape of the curve becomes lost. The matter of interest is where the case with 2.5 pixels across the FWHM lies in this progression. As can be seen, the function $\partial f/\partial\mu_3$ is indeed oscillatory, with a characteristic "wavelength" defined as the separation of the zero-crossings at $x\approx -1.75$ and $x\approx +1.75$ of about 3.5 pixels. This scale is sufficiently large that individual pixels sample the function fairly well, without too much cancellation between positive and negative lobes, so it seems that not too much information is lost in the binning, and that it should be possible to measure μ_3 satisfactorily with the image scale chosen for PRVS.

These subjective matters may be made quantitative as follows. With coarse pixels it will be necessary to collect more photons than for arbitrarily small ones by a factor N_{fac} given by the ratio of the integral in Eq.(7) to its discrete approximation obtained by summing over pixels. If the pixel width is Δx, so that the i-th pixel extends from x_i to $x_{i+1} = x_i + \Delta x$, then the binned functions may be written

$$\begin{aligned} f_i &= \int_{x_i}^{x_{i+1}} f(x)\mathrm{d}x \\ g_i &= \int_{x_i}^{x_{i+1}} g(x)\mathrm{d}x \end{aligned} \qquad (7)$$

and so

$$N_{fac} = \frac{\int_{-\infty}^{\infty} g^2(x)/f(x)\mathrm{d}x}{\sum_i \left(\frac{g_i^2}{f_i}\right)}. \qquad (8)$$

For the Gaussian SRF of width 2.5 pixels FWHM considered here, it is found that $N_{fac} = 1.24$. Measuring μ_3 will require nearly 25% more photons given our pixellated detector than in the ideal case in which the pixels are vanishingly small. Overall, about 7.5 million photons are required to measure μ_3 to better than one part in a thousand.

7.6.3 Discussion

The implications for the offline calibration process are now considered. First, how difficult is it to provide 7.5 million photons? A well-exposed arcline will have its central pixel just less than saturated, which we will take to imply 100,000 counts. The Gaussian profile of width 2.5 pixels covers several pixels along the dispersion direction, for a total of 2.66 times this number of counts; the same spreading is true perpendicular to the dispersion, so each fibre delivers about 750,000 photons in total when the central pixel has 100,000. This is almost exactly one-tenth of what is required, so ten successive exposures suffice to determine the skewness of this particular arc line with the required accuracy.

In fact, the calibration light is fed into all 7 sky fibres, so one exposure provides about 5 million photons, nearly enough: two exposures will suffice when the results of all 7 fibres are combined.

There are also many arclines, maybe 200 in all. The total flux in these lines has not been calculated, but we estimate that the total photon flux in all useful lines adds up to 10 times that in the brightest single line. A single exposure in which the brightest line approaches saturation therefore contains about 50 million photons in all the lines for all the fibres, plenty to determine the average skewness of the profile.

In a single daytime campaign of calibration consisting of say 100 exposures or more, it would not be difficult to accumulate many billions of photons, determining the skewness of the SRF and any gradients in the skewness across the detector, with more than enough accuracy for our purpose.

When observing, the sky fibres carry starlight but the reference fibre carries arclight. The total number of photons in the various arclines in an exposure in which the strongest approaches saturation is about 7.5 million, just enough to give an average value of μ_3 to the required accuracy. If, as is likely, superexposures are used in which the arc line system effectively provides perhaps ten times this much light in every stellar observation, it will be possible to determine the skewness quite accurately from each observation. The accuracy will not rival that obtained in an offline campaign, and it is not likely that these concurrent measurements will be used to determine the SRF to be used in data reduction, but they should be very useful in order to monitor the SRF to help decide when any changes have grown to the point that a new offline determination is needed; they may also be used to indicate if ever any unexpected change in the optics has occurred, signifying that some technical problem requires attention.

7.6.4 Conclusions

It is not difficult to measure the skewness of the SRF to the required accuracy of 1 part in 1000 in the dimensionless third moment μ_3 by making use of the standard arc calibration system required to keep track of image motion in PRVS. Daytime calibrations will give this parameter and its variation over the focal plane with more than enough accuracy, and it will even be possible to monitor the skewness with useful accuracy whilst observing by making use of the reference arc spectrum.

7.7 CALIBRATION REFERENCE

Moving into a new wavelength region it is important to consider the various possible calibration reference sources that we might use. Below we give some detail of the various calibration options that we have considered namely telluric, laser combs, gas-cell and simultaneous arc referencing. We conclude that simultaneous arc referencing is the most appropriate.

7.7.1 Telluric

The obvious calibration source for work in the infrared is the atmosphere. As we have seen in Section 5 it contains plentiful strong features that might be referenced against. Telluric features are ideal since they have same optical path as the starlight. The problem with the use of the atmosphere is that it is turbulent and has a wide range of velocity components. All of these are considerably larger than m/s signals that we seek. We discuss existing telluric work in Section 5.6.

7.7.2 Laser combs

One new technology has been considered for the calibration system. It is the laser comb generator, a repetitively-pulsed laser whose output light has a spectrum consisting of a number of narrow lines, uniformly spaced in frequency. The spectral range covered by the lines depends on the width of the pulses: when they are short, comparable in duration with one cycle of oscillation at the central wavelength of the laser, the comb may extend over as much as an octave. A laser comb could be ideal for PRVS if a suitable device could be found: it would provide a very large number of sharp lines across our entire observing spectrum, whose frequencies are accurately known and stable and whose intensities vary only moderately across the band. Such light would be perfect for the fundamental calibration of the wavelength scale of the spectrometer, for the determination of the point-spread function at every position on the detector, and for providing the reference spectrum when observing.

A steady train of equally-spaced pulses has a spectrum made up of sharp lines, the n-th having frequency f_n where

$$f_n = nF_c + F_z. \quad (1)$$

In this equation, n is an integer and F_c and F_z are constants whose value is determined by the design of the laser system. The comb frequency interval F_c is the more important of the two: it gives the separation of adjacent lines in the spectrum, while the zero-offset F_z is simply an additive constant. The values of both of these constants are locked to a highly-stable clock, and are known and stable to the accuracy of the clock.

Just one commercial laser comb system is available (product number FC1500 from Menlo Systems of Germany) that comes close to meeting all the requirements for PRVS. These requirements and the performance of the Menlo Systems product are listed in Table 1.

Laser comb performance: required for PRVS and delivered by Menlo Systems product FC1500

Property	Required	Delivered
Wavelength range	0.95 - 1.7 μm	1.05 - 2.1 μm
Output power (minimum)	1 μW	200 W
Frequency stability	1 in 10^9	1 in 10^{11}
Comb spacing F_c	25 - 50 GHz	0.1 GHz

The wavelength range almost fully overlaps our astronomical bands, with a slight mismatch at the short wavelengths. Since the comb does not end abruptly at the edge of the quoted band there will in fact be lines below 1.05 μm that would provide ample calibration into the Y astronomical band.
The total power received in our observing bands from a typical M dwarf star at a distance of 10 parsecs is of order 1 nW, and the reference system would be required to put out something comparable. Allowing for losses and for the occasional requirement to observe a brighter star, 1 μW will suffice, and the comb generator provides eight orders of magnitude more than this.

The frequency stability requirement is to know and keep constant the comb frequencies to better than 0.3 m/s Doppler equivalent, which is 1 in 10^9. The standard clock in the Menlo Systems

device is a quartz oscillator stabilized by reference to the GPS navigational satellite system and is good to 1 in 10^{11}.

The required comb spacing is determined by a compromise between having adjacent lines in the comb well-resolved by the spectrometer in PRVS whilst wanting as many lines as possible in order to improve the quality of the local calibration all over the face of the detector; a spacing of about 5 - 10 FWHM of the spectrometer point-spread function would be appropriate. At $\lambda = 1\mu$m, 1 km/s corresponds to a Doppler shift of 1 GHz, so the FWHM of our SRF of 5 km/s corresponds to 5 GHz. With the lines separated by 5 - 10 FWHM, the comb spacing should be of order 25 - 50 GHz. The Menlo Systems device has a comb spacing of only 0.1 GHz, and in this parameter, and only this parameter, the product falls well short of what is required for PRVS. The spectrometer would not even be able to resolve lines as close together as this.

Increasing the comb separation by a factor of 300 or so to meet the specification for PRVS is not trivial. The comb separation is equal to the reciprocal of the pulse separation, and increasing the pulse rate of the laser by a factor of 300 is likely to prove very difficult. In a telephone call, the management of Menlo Systems said that they have recently started a research programme to investigate whether it is possible to design a product with a wide comb separation that would be suitable for astronomy. They stated that they do not expect to be able to achieve this by developing their present technique and that a completely different approach would be necessary, if it is possible at all.

It is possible in principle to devise a Fabry-Perot filter system which would greatly attenuate most of the lines in the comb from the FC1500, only transmitting one in 300 of them. In practice the high rejection required for the unwanted lines and the difficulty of ensuring that each transmission peak falls exactly on a line in the comb (given the finite offset F_z in Equation 11 make the design and construction of a Fabry-Perot system a major undertaking in itself, and we have decided not to proceed with this for PRVS.

Our strategy is therefore to adopt the arc-line system for calibration, and to keep in touch with developments at Menlo Systems and elsewhere in case a suitable generator comes available. One possibility is that generators will become available with wider comb separations, but not wide enough for direct use on PRVS. The difficulty of designing and building a Fabry-Perot filter system decreases steadily as the comb separation increases; a filter system is still a substantial project if $F_c = 1.0$ GHz but much easier if $F_c = 10$ GHz. Depending on what progress is made with laser systems it may be that a comb generator plus Fabry-Perot becomes an attractive option within a few years.

7.7.3 Externally dispersed interferometry

2006 has seen success the first success (Ge et al. 2006) of the externally dispersed interferometry technique recently pioneered by Erskine & Ge (2000). This is a most promising technique because it requires a relatively low resolution spectrograph and recovers precise spectral information from interference fringes. Such instruments have been based on lower resolution spectrographs (allowing cost saving relative to traditional radial velocity instruments) and rely on the gradients of interference fringes to maximise the recovery of sub-pixel spectral information. Such an approach may well be most efficient way to multiplex radial velocity surveys to search

large numbers of objects (ASSE). However, for precision radial velocities the necessity to mask narrow telluric features would seem to be a limiting factor for this technique. The prevalence of narrow telluric emission and absorption features in the infrared means that reliable velocity information would only be available for a relatively small number of resolution elements. Accordingly the first generation of instruments TEDI (Edelstein et al. 2006) is aiming for a 100 m/s precision. Given the rather modest precisions (3m/s short-term, no published long-term stabilities) of the existing optical work which have taken a long time to achieve, along with the significantly enhanced telluric problems we consider this as a relatively high risk solution. Once more proven in the optical regime it will be appropriate to consider an interferometry retrofit to PRVS. Larry Ramsey (a member of this PRVS team) is involved with the Ge et al. (2006) and would this possibility and any options at PDR.

7.7.4 Gas-cell

The determination of precision radial velocities in the optical regime has been achieved by a number of different groups using gas absorption cells, but there are two objections to their use in PRVS:

1. We could identify no suitable gas or mixture of gases. The problem is that the spectra, while they may be fairly rich in lines, do not have the lines well spread through the spectral range required for PRVS. Molecules with electronic transitions in the infrared are relatively rare, and the transitions are instead rovibrational. Each molecular species has a small number of vibrational origins in our spectral range (typically 1 or 2), with maybe 10 – 30 rotational satellite lines near each. Each vibrational transition is thus good to calibrate perhaps one order of the spectrometer only, and we have not been able to circumvent this difficulty: no gas or mixture of gases we have studied gives a sufficient distribution of lines across the echelle orders.
2. The gas and gas cell absorbs light, decreasing the throughput undesirably. The reference lines mask stellar features in just the same way as telluric lines, and the grey absorption of the gas plus the effect of the windows of the gas cell absorb further.

7.7.5 Simultaneous arc

This, the adopted solution, is discussed in detail in the calibration document (PRVS-TRE-00004-0001), so we do not repeat it here. In summary, the use of a ThAr lamp will give a suitable line density over all orders, a suitable intensity range (with the use of fast detector readout), and the wavelength stability required for PRVS.

7.8 CHOICE OF WAVELENGTH CALIBRATION METHOD

In deciding the general form that the wavelength calibration system for PRVS should take there are two major issues and they are closely related. The first is whether to use a gas absorption cell or an arc emission cell as the wavelength reference, and the second is whether to feed the spectrograph through a slit or a fibre. The issues are linked because choosing a slit automatically favours an absorption cell, the reason being that, in monochromatic light at any wavelength, the distribution of light across the face of the detector is an image of the slit. The width of the slit of the present design is such that its image has a width of about 2 pixels on the detector, and so shifting the centroid of the light focussed on the slit shifts the centroid of the SRF on the detector by up to this amount. The width of the slit is therefore enough that a centroid shift in

the dispersion direction could change the zero of the velocity scale by several km/s, and while the position of the centroid on the slit would be stabilized (by a feedback system consisting of a camera to monitor the position of the centroid and a servo driving the tip-tilt part of the telescope adaptive optics system) it would not be easy to guarantee stability to the 1 m/s or so necessary for PRVS. An absorption cell would therefore be necessary because the reference spectrum would be imprinted on the starlight before it reaches the slit and would be focussed onto precisely the same spot. It would suffer exactly the same shift as the stellar spectrum as the centroid moves so that there could be no offset in the difference between them. This exact cancellation cannot be matched by any alternative scheme that makes use of an arc as the wavelength reference because, while it is not hard to focus a locally-generated emission-line spectrum onto the same slit as the starlight, there is no corresponding way to keep the centroid of the arc-light locked precisely to that of the starlight, and differential errors would be hard to avoid.

If a fibre is chosen as the spectrograph feed rather than a slit, however, there is no reason outright to prefer an emission-line or absorption-line reference, and a decision between them is more complicated because it has to take into account a number of factors. A system based on a fibre feed copes with motion of the centroid of the light focussed on the input end of the fibre in a completely different way from a slit: it exploits the scrambling of the modes in an over-moded fibre. This scrambling results in the position of the centroid of the light emerging from the downstream end of the fibre being almost independent of the position of the centroid of the light focussed on the upstream end. The dependence is not likely to be reduced exactly to zero, but we expect a reduction in sensitivity of about 3 orders of magnitude from the two-fibre scrambler system chosen for this project. The dependence on the position of the centroid of the focus on the input end of the fibre is reduced to a few m/s, which will easily be reduced to well below 1 m/s by the camera plus tip-tilt feedback system described in the previous paragraph. It follows that a calibration system based on arc light is not ruled out if a fibre is chosen.

After a long review of the two different methods we came to the conclusion that a fibre feed with an arc emission velocity reference system is best for PRVS. The principal considerations were the following:

a) Loss of light in the absorption cell. Absorption cells used in existing exoplanet spectrometers lose about 50% of the incident starlight. There need be no corresponding loss when an emission-line reference is used.
b) Inability to identify a suitable absorbing gas. The use of an emission-line system has a number of advantages, because the intensity can readily be adjusted to provide any desired peak intensity in the spectrum after convolution. It is therefore possible to provide much stronger lines, with the consequence that many fewer are needed. Electrical-discharge arcs in argon, krypton and xenon are known to provide sufficient lines in total, and they are better distributed amongst the orders of the échelle.
c) Stability of the SRF. Changes in the instrumental SRF over time are highly undesirable, but in a system with a slit the SRF varies depending on where the starlight is focussed between the jaws of the slit by virtue of the varying blockage of the light by the jaws; the SRF also varies with the seeing conditions. In a fibre-scrambler system the properties of the emerging cone of rays are almost independent of these factors at the input to the fibre, which eliminates many of the causes of variation of the SRF.

For these reasons we have chosen to offer a design for the exoplanet facility on PRVS in which fibres feed the spectrograph, and in which the velocity reference is provided by the arc emission from inert gases. There are a number of standard arc reference standards available for the NIR: ThAr, Kr, Xe, Ar and Ne lamps. Their standard use in infrared spectrographs means that there are existing lines lists for all these lamps. While the existing lists are likely to be adequate for our purposes, the quality control of the existing information, in particular, use of the re-calibration of ThAr by Florian Kerber at ESO will be a key part for our pathfinder experiment. It is possible that further high precision measurements maybe necessary at NIST or at the new infrared facility at Lund Observatory (Sveneric Johansson, private communication). The proposed calibration arrangements for PRVS are described in detail in the Calibration Assembly document (PRVS-TRE-00004-0001).

References

Ge J. et al. 2006, SPIE, 6269, 62691D1
Edelstein et al. 2006, SPIE, 6269, 62691E-1

8. CONCLUSIONS

We highlight some key findings of our study:

- M dwarf spectra have plenty of spectral information for precision radial velocities.
- Telluric contamination allows for approximately 90% of Y, 50% of J and 60 % of H to be used. This is a spectral range greater than currently used by precision optical studies.
- The NIR bands provide a significant improvement in velocity precision over the optical for late spectral types (≥ M6V) and whenever the star has substantial rotational velocity (v sin i > 5 - 10 km/s). The majority of M4 to L dwarfs are fast rotators, meaning that PRVS operating in the NIR will be more capable of detecting the RV signature from a low-mass planet around these low-mass stars.
- PRVS on Gemini will be capable of detecting Earth-mass planets around late M stars, and is expected to find these in a reasonable (5 year) survey.
- Intrinsic limits due to non-uniform photospheres are expected to be less at later M spectral types and into the NIR where the contrast is reduced.
- Our pathfinder experiment has demonstrated precision radial velocities in the NIR at levels of <10m/s.
- We do not find an appropriate gas for an absorption cell and propose simultaneous arc line calibration.

The key requirements for the PRVS instrument design are summarised in the following table:

Parameter	**Magnitude**	**1σ RV error**	**Comment**
Skewness measurement	±0.001	0.3 m/s	Requires ΔT=±0.05K
SRF drift	±0.1 pixel	0.3 m/s	Requires ΔT=±5K
SRF vibration	±0.1 pixel	<< 0.3 m/s	Cooler requires vibration isolation
Arc line measurement	≈ 10^5 e	6 m/s per line	300 lines for 0.3 m/s

In summary, these findings, the rest of our study and the existing body of literature enable us to judge that there is a strong scientific case for a PRVS-like instrument and consider that it will have a wide ranging impact on astrophysics. The impact of discovering terrestrial-mass exoplanets in the habitable-zones of the nearest stars will ensure that the scientific and public interest in exoplanets will continue its incredible growth. Even without the exoplanet science we consider that its proposed resolution, throughput and wavelength coverage make PRVS a landmark instrument.